Electron Tunneling in Proteins and Water

Thesis by

Adrian Ponce

In Partial Fulfillment of the Requirements

For the Degree of

Doctor of Philosophy

California Institute of Technology

Pasadena, California

2000

(Submitted November 10, 1999)

Acknowledgments

My graduate experience at Caltech has been rewarding on many levels and I would like to thank those who have supported me with advice and friendship along the way.

First, I would like to thank my advisors of past and present. I thank Harry Gray for generating a stimulating and exciting working environment. Harry is a model of kindness and is an inspiration for me in science. I thank Jay Winkler who has taken a tremendous amount of time to teach me the details of laser spectroscopy, ET theory, and much more. Perhaps most importantly, he has patiently taught me independent thinking and problem solving. I also thank my undergraduate advisor, Dan Nocera, whose never-ending enthusiasm for science made working in the lab an addictive activity. He brought me from a Michigan-State freshman who placed into a taped chemistry course that taught that C stands for carbon, to a Caltech-ready senior. Finally, I thank Greg Hillhouse for allowing me to work in his lab where I learned the art of high-vacuum synthesis. Collectively, my advisors have presented me with the beautiful gift of knowledge, which I hope to pass on to the next generation with the same enthusiasm as it was given to me.

I would also like to thank my collaborators who have helped make the work presented here possible. Max Bachrach introduced me to the world of picosecond transient-absorption spectroscopy. Pat Farmer mentored me on electrochemistry. Angelo Di Bilio invited me to work on the HiPIP project and kept it moving along swiftly. Ralf Alsfasser is the principal investigator of the work presented in Chapter 5, and was fun to work with during all-night laser lab sessions.

There are many people in the department crucial for progress in research. I thank Dian Buchness, who is the friendliest secretary I know. I thank Steve Gould, who not only efficiently places orders, but also gets the Christmas party hopping with his band, and Chris Smith who has seen Jimi Hendrix perform live at the Monterey Pop Festival. I thank Mike and Guy in the machine shop, Rick in the glass shop, Tom in the electronics shop, Fenton in the analytical lab, Peter Green in the mass spectrometry lab, Larry Heinling and Mike Day in the X-ray crystallography lab. Thank you for your support!

I thank Gray group members of past and present, especially Kara for her kindness and friendship, Ivan and Akif whom I often consulted and shared many fun moments with, Randy who stood in line for Star Wars tickets with me, Corinna who put up with me while sharing an office, and Lila who underwent the same torment. I would also like to thank Jeff Regan for watching late night documentaries in my office with me, and Jeff Rack for interesting scientific discussions.

Of course I want to thank Helen and Jim, who were my house- and classmates. I miss watching the very therapeutic MASH sessions with Helen. And Jim, who I met while I was hijacking a shopping cart to bring groceries home to the Cats. At first he wanted to report me but then he realized that I was bringing the groceries into his apartment. Thank you for being a great friend and roommate.

From the Nocera group, I would like to thank Doug, Jim, and J.P., whom I lived and worked with. I also thank Zoe and Jeff, who initiated me into the experimental world.

My acknowledgments would be incomplete if I did not mention Dr. Erwin Huber, who was the first academic type that believed in me when I was a kid, despite my lack of interest. And Michael Günther, who was my childhood friend. I will see you on the bench.

A special thanks to Xenia! I have already learned so much from you and I look forward to every new day that we can spend together.

I would like to thank Pete and Tracy who invited me to America and provided a beginning to this journey. I also thank Katie and Kelly who I have watched grow over the years. Finally, I thank my Mom and Dad who have given me their love and support over the years. Most importantly, they allowed me to have a carefree childhood. Thank You All!

Abstract

The subject of this thesis is electronic coupling in donor-bridge-acceptor systems. In Chapter 2, ET properties of cyanide-bridged dinuclear ruthenium complexes were investigated. The strong interaction between the mixed-valent ruthenium centers leads to intense metal-to-metal charge transfer bands (MMCT). Hush analysis of the MMCT absorption bands yields the electronic-coupling strength between the metal centers (H_{AB}) and the total reorganization energy (λ). Comparison of ET kinetics to calculated rates shows that classical ET models fail to account for the observed kinetics and nuclear tunneling must be considered.

In Chapter 3, ET rates were measured in four ruthenium-modified high-potential iron-sulfur proteins (HiPIP), which were modified at position His50, His81, His42 and His18, respectively. ET kinetics for the His50 and His81 mutants are a factor of 300 different, while the donor-acceptor separation is nearly identical. PATHWAY calculations corroborate these measurements and highlight the importance of structural detail of the intervening protein matrix.

In Chapter 4, the distance dependence of ET through water bridges was measured. Photoinduced ET measurements in aqueous glasses at 77 K show that water is a poor medium for ET. Luminescence decay and quantum yield data were analyzed in the context of a quenching model that accounts for the exponential distance dependence of ET, the distance distribution of donors and acceptors embedded in the glass and the excluded volumes generated by the finite sizes of the donors and acceptors.

In Chapter 5, the pH-dependent excited state dynamics of ruthenium-modified amino acids were measured. The $[Ru(bpy)_3]^{2+}$ chromophore was linked to amino acids *via* an amide linkage. Protonation of the amide oxygen effectively quenches the excited state. In addition, time-resolved and steady-state luminescence data reveal that nonradiative rates are very sensitive to the protonation state and the structure of the amino acid moiety.

Я посвящаю эту работу Ксеньке, Боошкину, и Беньчику.

Table of Contents

List of Figures

Chapter 1

Chapter 2

Chapter 3

Chapter 4

Chapter 5

List of Tables

Chapter 1

Introduction to Electron Transfer in Chemistry and Biology

The global impact of electron transfer (ET) becomes clear when the detailed reaction mechanisms of photosynthesis and aerobic metabolism are considered (Equation 1.1) [1].

Equation 1.1.

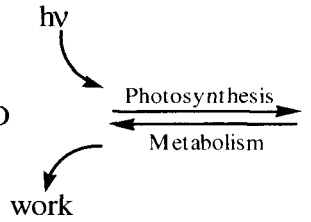

$$6\ CO_2 + 6\ H_2O \rightleftharpoons C_6H_{12}O_6 + 6\ O_2$$

Light absorption in the photosynthetic systems of plants and algae drives the generation of glucose and oxygen from atmospheric CO_2 and water. The energy stored in glucose is liberated in the respiratory system to perform mechanical or chemical work as required by the organism.

ET in the bacterial photosynthetic reaction centers is well characterized thanks to high-resolution crystal structures [2,3] (the first structure of a membrane spanning protein), spectroscopy and fast kinetics measurements [4,5]. Electromagnetic radiation captured by surrounding pigments is transferred to the reaction center (RC) in a few picoseconds, which results in excitation of the special pair (P). P* is a strong reducing agent and transfers an electron over 18 Å to bacteriopheophytin in 3 picoseconds. The following ET events to reduce menaquinone and subsequently ubiquinone occur in 100 ps and 100 ns, respectively. Each forward ET step is exothermic. Nevertheless, the final charge separated state lies more than 0.3 eV higher than the ground state, energy that is available for synthesis of high-energy molecules such as ATP. Charge separation in the reaction center occurs efficiently over long distances (>50 Å) on a nanosecond timescale, while the energy wasting charge recombination reactions are orders of

magnitude slower. There are still many interesting, unanswered questions, such as the curious fact that only one arm of the nearly symmetric reaction center is ET active [6,7]. And so, the reaction center has and will continue to provide a fertile laboratory to examine ET theory.

ET plays a central role in many other biological systems, most of which consist of metalloproteins. Many metalloproteins have been synthetically modified to attach a ruthenium complex that can act as an artificial redox partner [8,9]. These types of systems have been prepared extensively to study long-range intramolecular ET mediated by the protein matrix, and the parameters that govern the ET process. Investigations of distance dependence revealed that the efficiency of long-range ET depends on the secondary structure that bridges the space between the redox partners. In general, β-sheets mediate ET more efficiently than α-helices, and hydrogen bonds are important in both [8,9]. β-strands are structurally straight, with almost direct covalent connections between the donor and acceptor, while α-helices present a more circuitous route. The wealth of experimental data has allowed formulation of theoretical models that try to determine the most efficient pathway connecting the redox sites. Pathway models that assign differential coupling strength to covalent, hydrogen-bonded and through-space segments, and search for the most efficient coupling pathway between the redox sites have been successful at describing many of the experimental data [10-14].

Many elegant, synthetic efforts have generated model systems that provide a more controlled environment in which to perform systematic studies on ET parameters [15-17]. Controlling the structure of the donor, acceptor and bridge have allowed

systematic studies of free energy, orientation, and distance dependence. These findings confirmed many of the theoretical predictions and provided insights for more sophisticated formalisms.

After four decades of an iterative relationship between theory and experiment, we have a better understanding of ET processes. Nonetheless, many challenges need to be met before we can reproduce nature's efficiency in photochemical energy storage. Beyond that, molecular electronics [18-20] coupled with nanotechnology [21,22] endeavors to create molecular sized supercomputers; But first and foremost, a clear understanding of the properties that govern ET is required.

Electron transfer (ET) is the only chemical reaction that can occur at distances several times the spatial extension of the donor and acceptor centers, sometimes exceeding 20 Å with rates that are greater than $10^3 s^{-1}$. In ET reactions, no bonds are formed or broken and only bond length and angle adjustments in the ET partners and the reaction medium are needed to accommodate product formation. The simplicity of ET reactions has allowed the development of elegant and powerful theoretical treatment that describes ET in terms of a small number of experimentally accessible parameters [23].

Classical Marcus Theory

In 1956, Marcus published the seminal paper on what came to be known as classical electron transfer (ET) theory [24]. Classical ET theory is based on the Franck-Condon principle and the law of energy conservation. The Franck-Condon principle states that since the masses of nuclei are much greater than that of an electron,

the positions, or momenta of the nuclei change much slower than those of an electron. Consequently, the nuclei do not have time to change either their positions or momenta during the ET event. Therefore, ET can only occur (classically) at the transition state (Figure 1.1), where nuclei do not need to move and energy is conserved upon product formation. Thermal fluctuations in the nuclear and solvent coordinates of the reactant (D–A) lead to the transition state geometry [23]. Following ET, the nuclear and solvent coordinates relax to stabilize the new charge distribution of the ET product (D^+–A^-).

The rate constant for ET (k_{ET}), according to classical theory, is given by:

Equation 1.2.
$$k_{ET} = A\exp\left(\frac{-(\Delta G^o + \lambda)^2}{4\lambda kT}\right)$$

where A is the preexponential frequency factor that depends on the nature of the ET event. For bimolecular reactions the prefactor is equal to $\kappa A\sigma^2$, where κ is the transmission coefficient, and $A\sigma^2$ has dimensions of collision frequency. In an intramolecular reaction the prefactor is equal to $\kappa\nu_n$, where ν_n is the nuclear vibrational frequency, usually taken to be ~1 × 10^{13} s^{-1}. The crossover probability to form products depends on the transmission coefficient, κ. In general, classical theory is utilized to describe adiabatic (i.e., strongly coupled) ET reactions where $\kappa = 1$ [25]. The standard free energy for the reaction is represented by ΔG^o and the reorganization energy by λ. The total reorganization energy (λ) is composed of inner sphere (λ_i) and solvent (λ_s) contributions:

Equation 1.3.
$$\lambda = \lambda_i + \lambda_s$$

Equation 1.4. $$\lambda_i = \frac{1}{2}\sum_l f_l\left(\Delta q_{e,l}\right)$$

Equation 1.5. $$\lambda_s = (\Delta e)^2\left[\frac{1}{2a_1} + \frac{1}{2a_2} - \frac{1}{R}\right]\left[\frac{1}{\varepsilon_\infty} - \frac{1}{\varepsilon_o}\right]$$

The inner-sphere reorganization energy can be estimated from intramolecular vibrational force constants (f_l) and the change in equilibrium positions between the reactants and products ($\Delta q_{e,l}$) (Equation 1.4). These parameters can be gleaned from vibrational spectroscopy and X-ray structures. An estimate of λ_s can be obtained by using a model in which reactants and products are rendered as spheres and the solvent as a dielectric continuum (Equation 1.5). Here a_1, a_2, R, ε_∞, and ε_o are the radii of the donor and acceptor, the distance between their centers, and the optical and static dielectric constants, respectively [26,27].

Classical ET theory predicted that the cross-reaction rate (k_{12}) of two reactants (labeled 1 and 2) can be calculated from two self-exchange rate constants (k_{11} and k_{22}) and the equilibrium constant (K_{12}).

Equation 1.6. $$k_{12} = \left(k_{11}k_{22}K_{12}f_{12}\right)^{1/2}$$

where f_{12} is a known function of k_{11}, k_{22}, and K_{12}, and is usually close to unity [23]. This relation was later validated by experimental data obtained by Sutin in 1962 [28].

The most famous prediction is the existence of the inverted region (Figure 1.2). As the driving force ($-\Delta G^o$) for the reaction is increased, the logarithm of the ET rate increases (normal region), reaches a maximum (activationless), and decreases again (inverted region) in parabolic fashion. It was not until 1984 when experimental

Figure 1.1 Plot of the free energy of the reactants and products as a function of nuclear configuration (reaction coordinate) for ferric-ferrous self-exchange. Thermal electron transfer occurs at the transition state configuration. The change in nuclear configuration of reactants (where the circles represent inner-sphere coordinates, and the arrows represent solvent dipoles) to form products is illustrated by the difference in the radii of the oxidized and reduced forms of the redox couple and the change in the average orientations of the solvent dipoles [30].

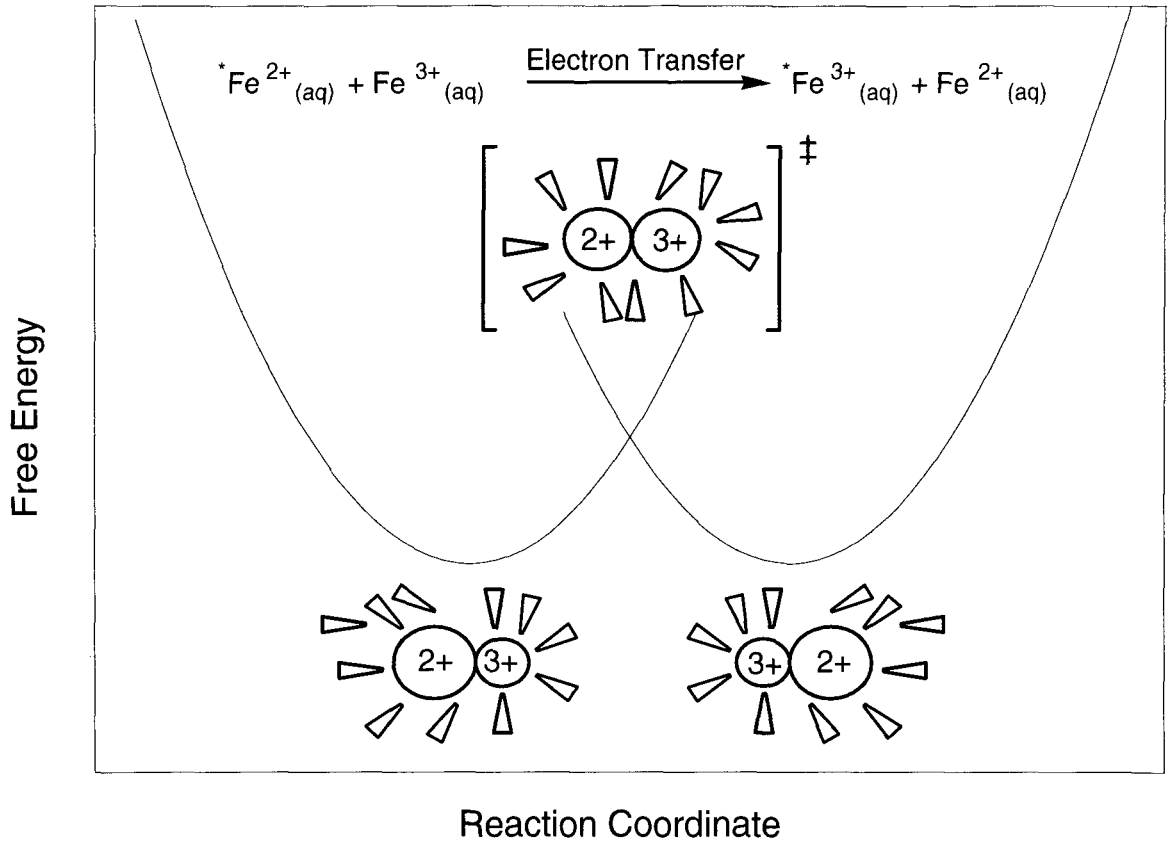
*Fe 2+ (aq) + Fe 3+ (aq)
Electron Transfer
*Fe 3+ (aq) + Fe 2+ (aq)
‡
2+
3+
2+
3+
3+
2+
Free Energy
Reaction Coordinate

Figure 1.2 Logarithm of ET rate *vs.* free energy plot. ET reactions occur in the normal region, activationless or in the inverted region when $-\Delta G^{o} < \lambda$, $-\Delta G^{o} = \lambda$, $-\Delta G^{o} > \lambda$, respectively.

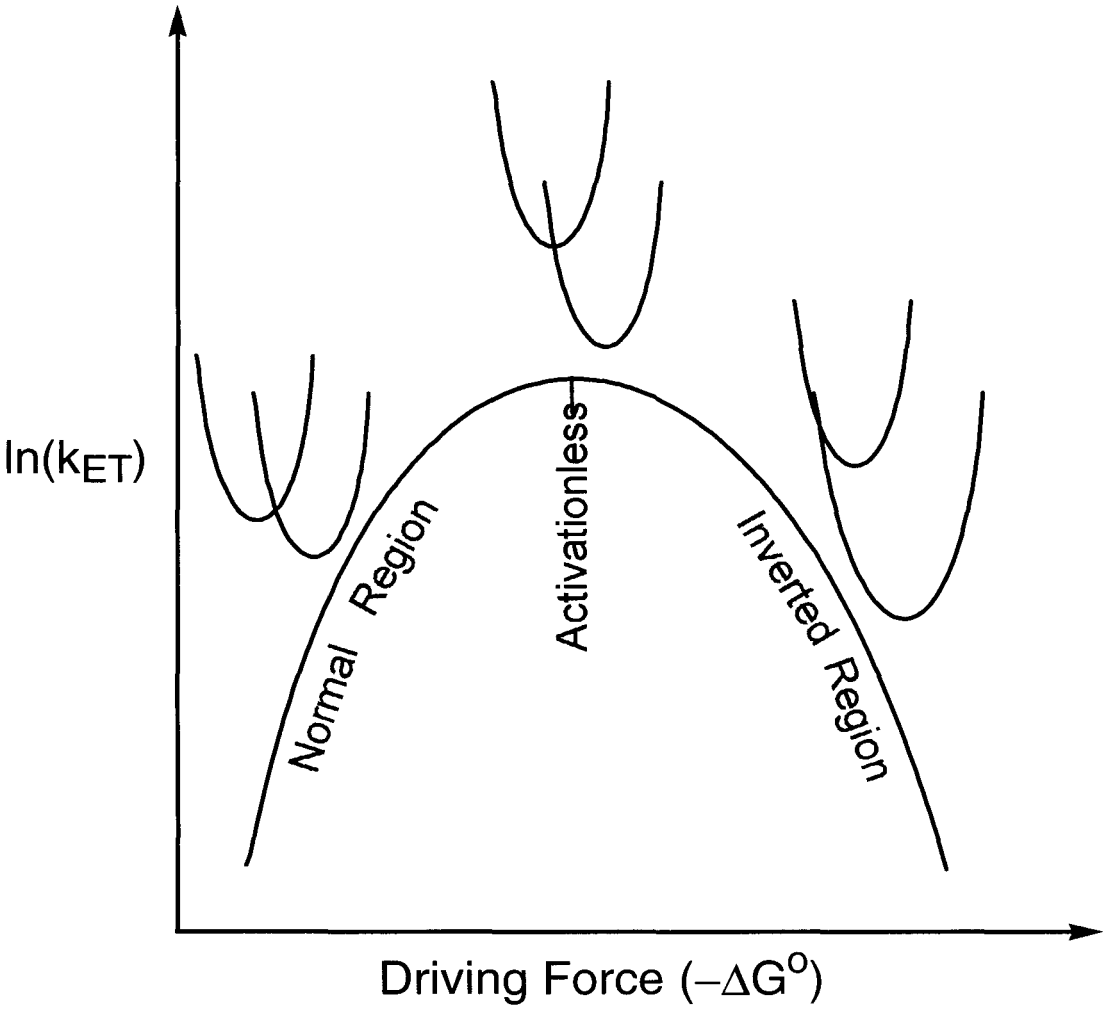
ln(k_ET)
Normal Region
Activationless
Inverted Region
Driving Force (–ΔG°)

evidence for the inverted region was found by Closs and Miller [29]. The inverted effect has been used to explain the efficient charge separation in the photosynthetic reaction center. Small reorganization energies allow charge separation to occur nearly activationless at low driving forces, minimizing the energy loss. The charge recombination is highly inverted, and thus slow, allowing subsequent charge separation steps to be competitive with energy wasting charge recombination.

Similarly, the photophysical properties of $[Ru(bpy)_3]^{2+}$ exemplify a model system of the photosynthetic reaction center. MLCT excitation of this complex leads to a charge-transfer state that has a lifetime of 600 ns. Charge recombination is highly inverted ($-\Delta G^{\circ}$ and λ of 2.0 eV and 0.26 eV, respectively) and thus faces a large activation barrier. The long lifetime is noteworthy, considering that the distance of charge separation is only 3.4 Å, the electronic coupling (H_{AB}) is strong (400 cm^{-1}) and about 3×10^6 vibrations will have occurred during the lifetime [30].

Quantum Mechanical Models for Electron Transfer

Electron Tunneling

Electron tunneling occurs when a potential barrier exists for electron motion in the space between the donor-acceptor pair. The rate of electron tunneling depends on the magnitude of the electronic-coupling strength, H_{AB}, between donor and acceptor. The electronic-coupling strength is the effective electronic Hamiltonian matrix element that couples the reactant and product states for the ET reaction. For weakly coupled (nonadiabatic) ET reactions, the transition state must be formed many times before an electron is transferred, and is described by semiclassical models [31,32]. The most

Figure 1.3 Plot of free energy *vs.* reaction coordinate for an ET reaction. The splitting at the intersection of the curves is defined as $2H_{AB}$, where H_{AB} is the electronic coupling matrix element. The reorganization energy (λ) is the free energy difference of the reactants at the equilibrium nuclear coordinates and at the equilibrium nuclear coordinates of the products. The activation barrier and the free energy of the reaction are designated $\Delta G^{\ddagger}$ and ΔG^{o}, respectively.

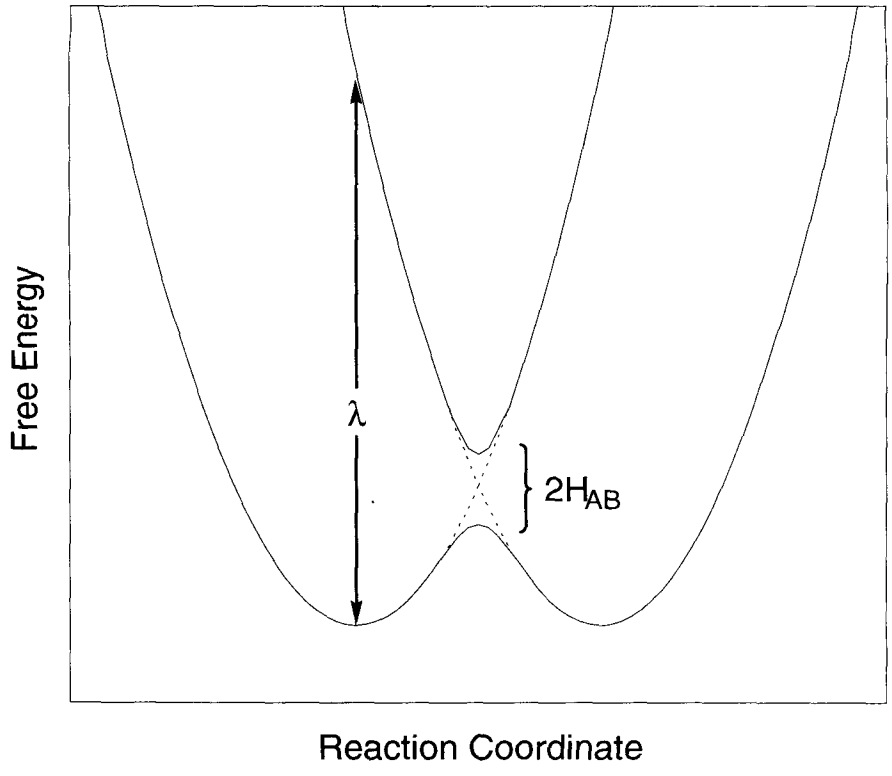
Free Energy
λ
2H_AB
Reaction Coordinate

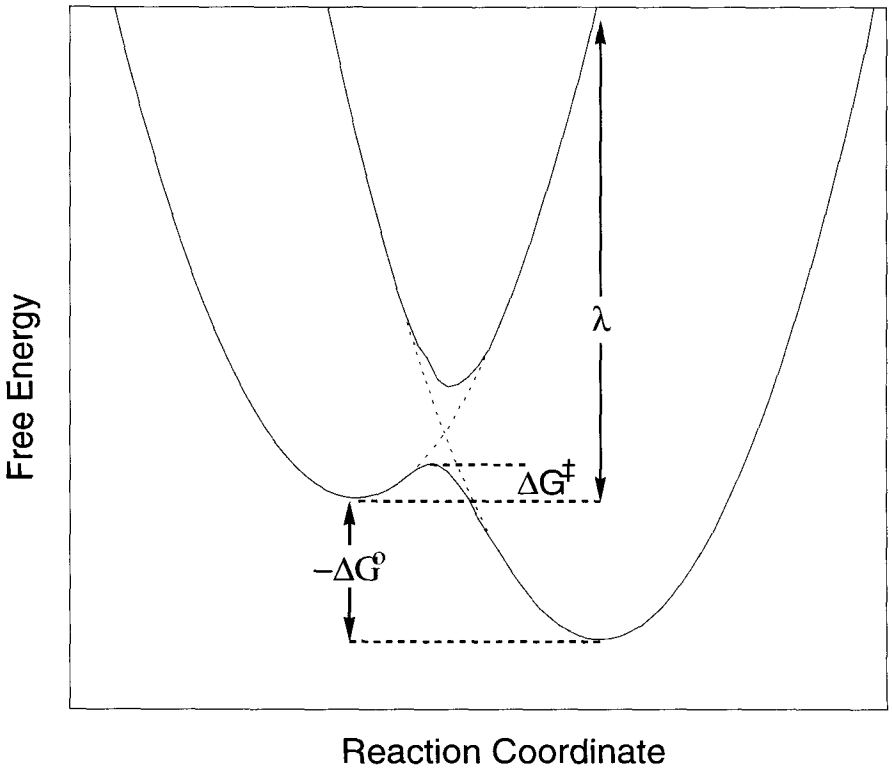
Free Energy
λ
ΔG‡
−ΔG°
Reaction Coordinate

frequently used semiclassical model used to describe long-range ET treats all nuclear coordinates classically (Equation 1.7).

Equation 1.7.
$$k_{ET} = \left(\frac{4\pi^3}{h^2 \lambda kT}\right)^{1/2} (H_{AB})^2 \exp\left(\frac{-(\Delta G^o + \lambda)^2}{4\lambda kT}\right)$$

If H_{AB} becomes large, the rate of product formation becomes limited by the rate at which the transition state is formed (see page 27).

The magnitude of H_{AB} declines exponentially with distance (R) from H_{AB} at contact (H^o_{AB}) and is scaled by the distance-decay constant (β) (Equation 1.8) [33-38].

Equation 1.8.
$$H_{AB} = H^o_{AB} \exp\left(-\frac{\beta R}{2}\right)$$

The exponential distance-decay constant (β) is believed to be sensitive to the composition of the intervening medium [39]. The electronic coupling between redox sites in vacuum decays rapidly with distance, leading to large values of β (3-5 $Å^{-1}$) [10,40]. Moderated distance decays, however, are provided when an intervening medium bridges the redox sites. Distance dependence studies have been performed for a variety of redox partners and bridging units including alkanes [41,42], alkenes [43-46], alkynes [47-49], phenyl [50,51], protein matrices [52,53], DNA [54,55], and frozen solvents [56,57]. Distance decay factors (β) are centered at 1.0 ± 0.3 $Å^{-1}$, with the exception of alkenes, alkynes and DNA (Barton), which range between 0.2 $Å^{-1}$ and 0.5 $Å^{-1}$.

Superexchange models are frequently employed to explain the distance dependence of ET reactions in which coupling *via* hole and/or electron states of an intervening medium (bridge) provides enhanced coupling [58-60], with respect to

vacuum. The bridge group levels, consisting of the lowest unoccupied (LUMO, electron transfer) or highest occupied molecular orbital (HOMO, hole transfer), can be significantly higher energy than the donor and acceptor levels. Nonetheless, the bridge group orbitals constitute lower tunneling barriers than direct ET where the barrier would correspond to full ionization. Therefore, the electronic coupling *via* the nearest-neighbor bridge groups is more favorable than direct coupling of donor-acceptor wavefunctions. The McConnell superexchange model, illustrated in Equation 1.9,

Equation 1.9. $$H_{AB} = \frac{h_{D-br}}{\Delta\varepsilon}\left(\frac{h_{br-br}}{\Delta\varepsilon}\right)^{n-1} h_{br-A}$$

is an attractive formalism that is used in contemporary work on pathways or bond counting, and highlights the important factors that govern superexchange [33]. The model describes the electronic coupling between a donor and an acceptor separated by a bridge comprised of identical repeat units, D-$(br)_n$-A. The matrix elements $h_{D\text{-}br}$, $h_{br\text{-}br}$, and $h_{br\text{-}A}$ describe the electronic coupling of donor to bridge, adjacent bridges, and bridge to acceptor, respectively. The tunneling energy gap, $\Delta\varepsilon$, is defined as the vertical energy difference between the tunneling energy (energy at the transition state) and the energy of the bridge levels, which are the one-electron oxidized (for hole transfer) and one-electron reduced (for electron transfer) bridge states. Organic bridges are usually easier to oxidize than to reduce; thus, superexchange *via* hole transfer will dominate.

From this model and the exponential distance dependence of H_{AB} we obtain an expression (Equation 1.10) for β in terms of two parameters,

Figure 1.4 Plot of free energy *vs.* reaction coordinate for bridge mediated ET. Bridge reduced and bridge oxidized states can give rise to enhanced overall coupling (H_{AB}) between the donor and acceptor. The tunneling energy gap ($\Delta\varepsilon$) is defined as the energy difference between the energy at the transition state and the energy of the mediating bridge states. The oxidized and reduced bridge states mediate ET *via* hole- and electron-transfer mechanisms, respectively. Simple superexchange models predict that the distance dependence of ET is a function of bridge to bridge electronic coupling (h_{bb}) and the tunneling energy gap ($\Delta\varepsilon$).

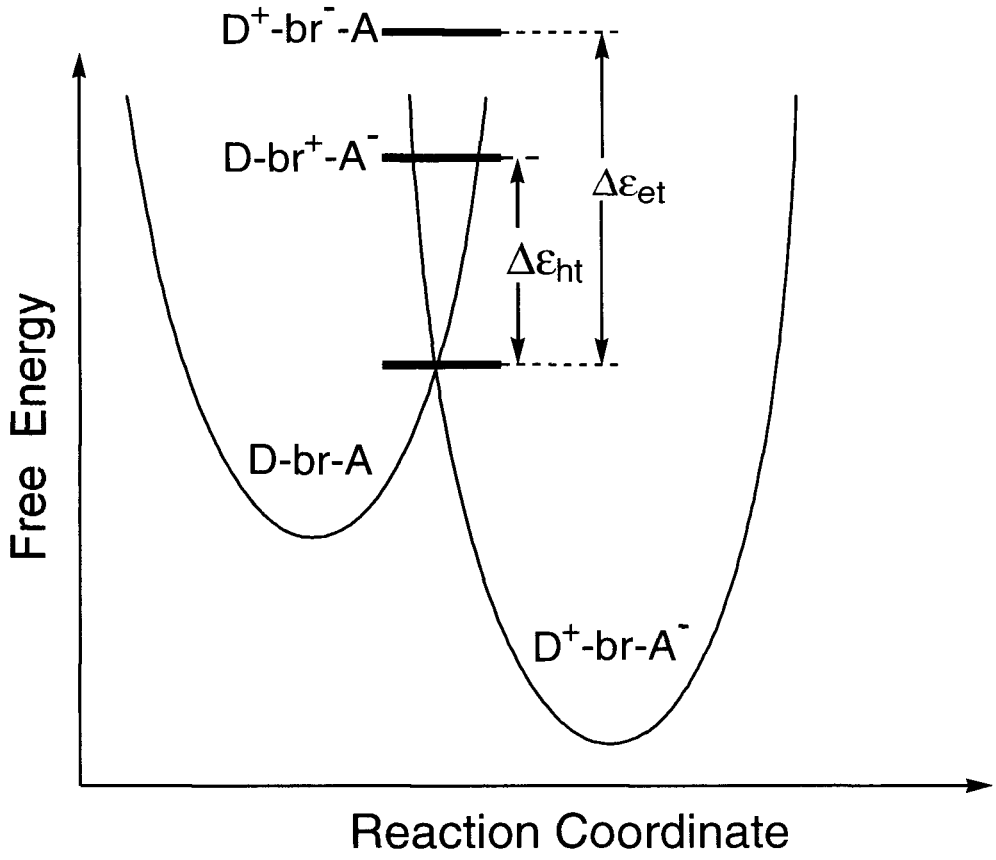

$$H_{AB} = \frac{h_{Db}}{\Delta\varepsilon}\left(\frac{h_{bb}}{\Delta\varepsilon}\right)^{N-1} h_{bA} = H_{AB}^{o} \exp\left(\frac{-\beta R_e}{2}\right)$$

$$\beta = -2a^{-1} \ln\left(\frac{h_{bb}}{\Delta\varepsilon}\right)$$

Figure 1.5 Schematic depiction of nearest neighbor superexchange coupling *via* two bridge units, each of which has an occupied (HOMO) and an unoccupied orbital (LUMO). The uppermost diagram serves as a legend for the processes depicted in (a) and (b). Diagram (a) depicts electron transfer mediated superexchange, and diagram (b) depicts hole transfer mediated superexchange.

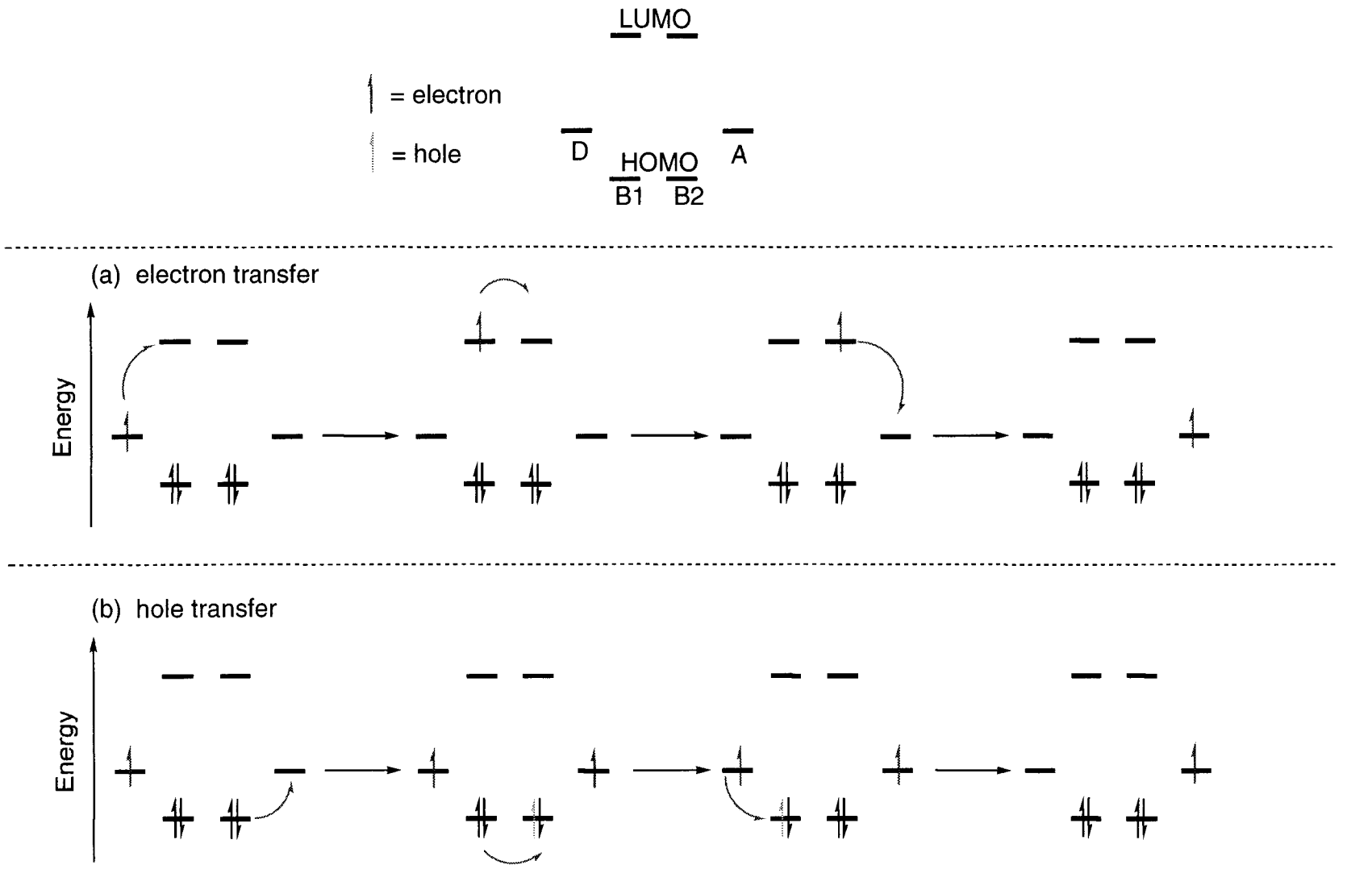
LUMO
= electron
= hole
D
HOMO
B1
B2
A
(a) electron transfer
Energy
(b) hole transfer
Energy

Equation 1.10. $$\beta = -2a^{-1} \ln\left(\frac{h_{br-br}}{\Delta\varepsilon}\right)$$

where a is the length of a bridge unit. Alternative approaches in determining β involve the distance dependence of the optical intervalence bands of mixed-valence compounds (see page 28).

The limitations in the McConnell model are that either hole- or electron-transfer states, but not both, mediate ET and that the bridge consists of identical repeat units. *Ab Initio* calculations have shown that superexchange models are not quantitatively correct [34,35,37,61]. However, more sophisticated superexchange models that account for many-particle and hybrid pathway perspectives provide improved results [39].

Nuclear Tunneling

ET products can be formed by nuclear tunneling, which presents an alternate route to electron tunneling. Rather than forming ET products by electron tunneling at the transition state, the products are formed by tunneling through the activation barrier [62-64]. At room temperature, nuclear tunneling in the normal region is negligible, but can lead to significant rate enhancements in the inverted region, especially if there are high frequency modes associated with the donor and/or acceptor groups. This rate-enhancing behavior in the inverted region has been observed for both intra- and bimolecular electron-transfer reactions [29,65,66]. Moreover, nuclear tunneling can occur at low temperature where the thermal energy is too low to populate the transition-state geometry significantly. In fact, at sufficiently low temperatures, all of the reaction occurs by nuclear tunneling. The magnitude of the nuclear tunneling contribution to the rate of ET can be determined by calculating the quantum mechanical Franck-Condon factors [67-73]. In general,

Figure 1.6 Plot of the free energy of the reactants and products against the reaction coordinate overlaid with the vibrational wavefunctions of a single mode. Nuclear tunneling is facilitated by overlap between reactant and product vibrational wavefunctions (Franck-Condon factor). In the normal region (a), the overlap between reactant and product vibrational wavefunctions is small, and thus nuclear tunneling is often negligible. In the inverted region (b), the overlap of the vibrational wavefunctions can become significant, especially when high-frequency modes are present (bottom). Here significant increases in rate due to nuclear tunneling can occur (Figure 1.7).

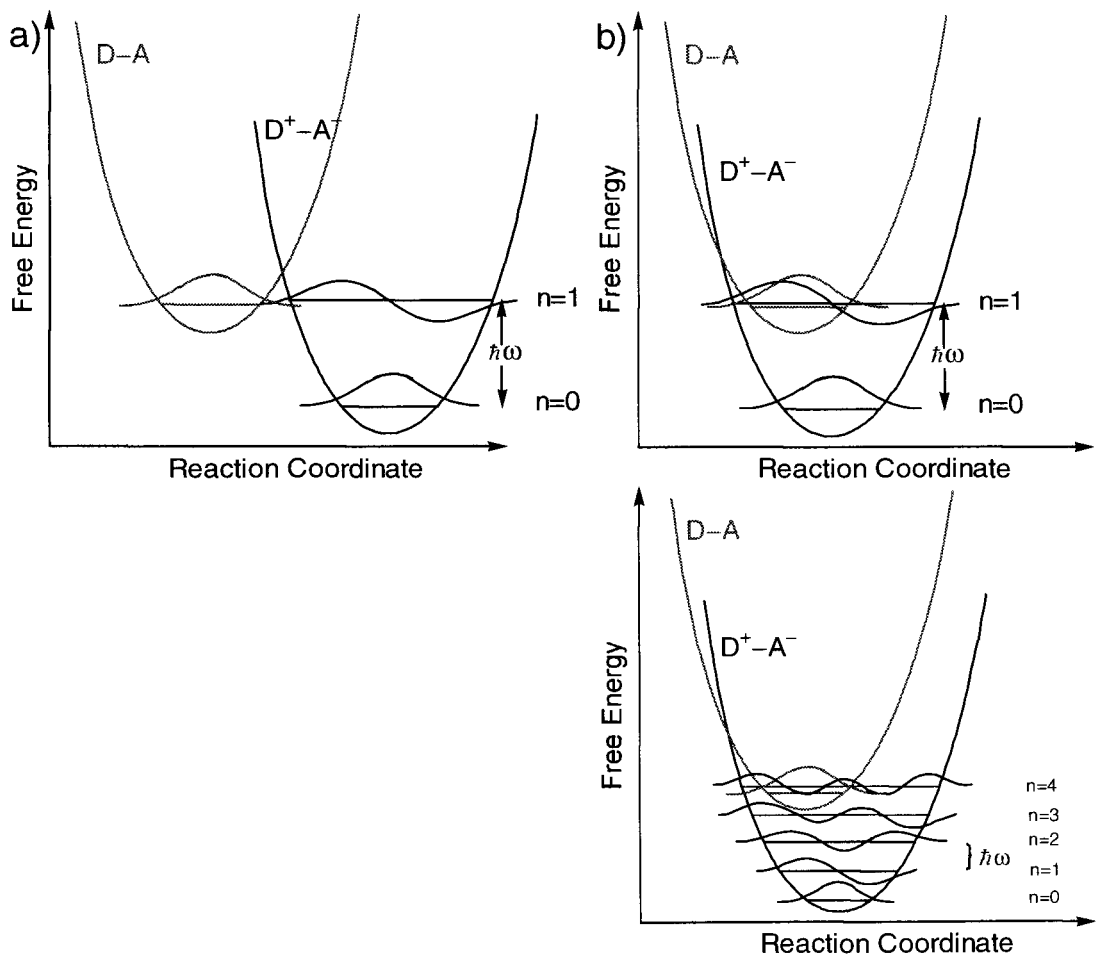
a)
D–A
D+–A–
Free Energy
n=1
ħω
n=0
Reaction Coordinate
b)
D–A
D+–A–
Free Energy
n=1
ħω
n=0
Reaction Coordinate
D–A
D+–A–
Free Energy
n=4
n=3
n=2
ħω
n=1
n=0
Reaction Coordinate

Figure 1.7 Plot of $\log(k_{ET})$ *vs.* $-\Delta G^{\circ}$ illustrating the effect of increasing nuclear tunneling. The plot was generated from Equations 1.11 and 1.12 with different values of dimensionless distortion parameter, S. The increase in rate due to nuclear tunneling is more pronounced in the inverted region.

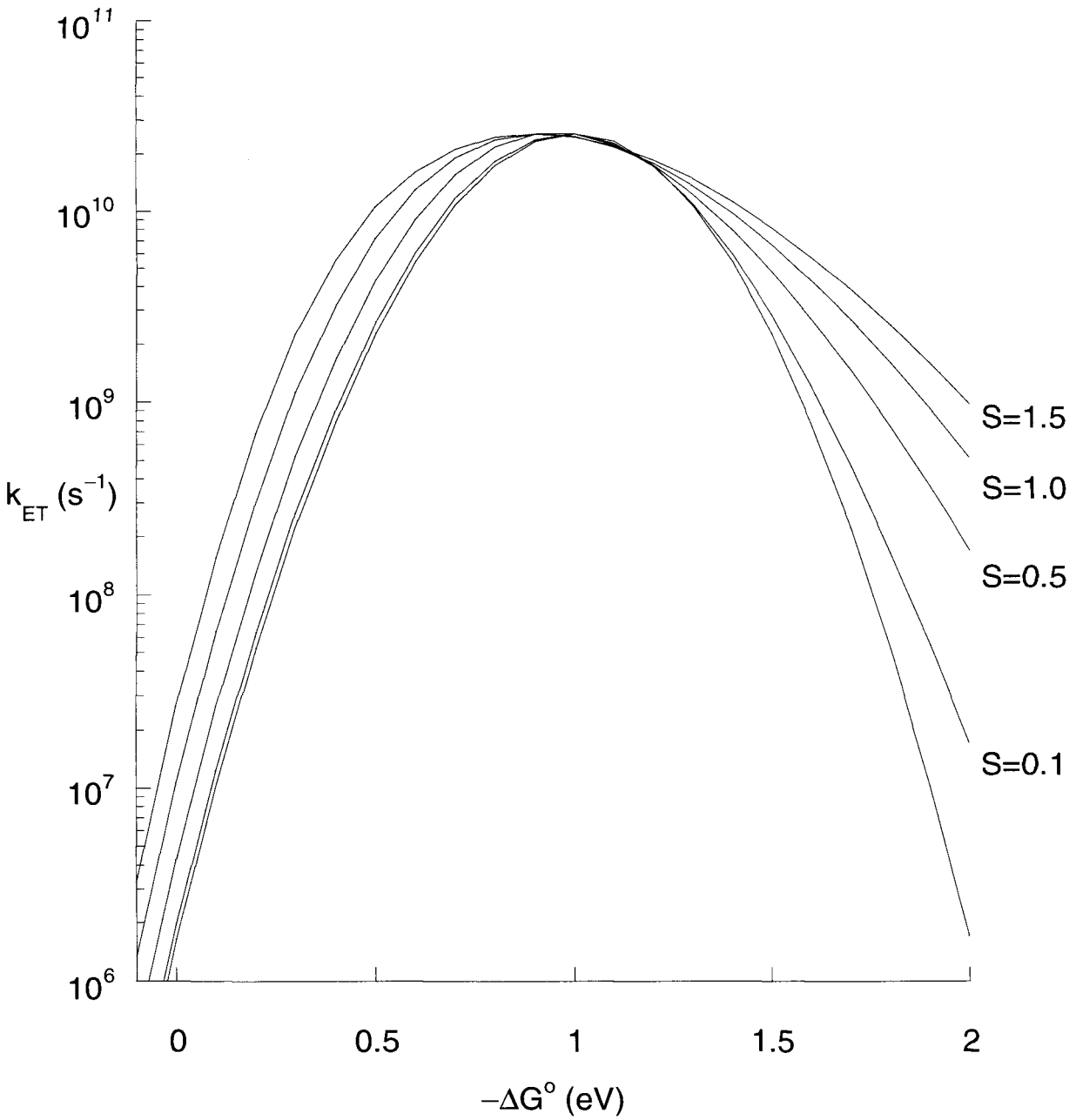
10^{11}
10^{10}
10^{9}
10^{8}
10^{7}
10^{6}
k_{ET} (s^{-1})
S=1.5
S=1.0
S=0.5
S=0.1
0
0.5
1
1.5
2
$-\Delta G^{o}$ (eV)

quantum mechanical models for nuclear motion either treat all coordinates (solvent and inner sphere) quantum-mechanically or treat the inner-sphere quantum-mechanically, while treating the solvent classically [23]. Equation 1.11 represents the latter case in which one vibrational mode is represented.

Equation 1.11.
$$k_{ET} = \frac{2\pi}{\hbar(4\pi\lambda_s kT)^{1/2}} H_{AB}^2 \sum_{n=0}^{\infty} |\langle 0|n\rangle|^2 \exp\left(\frac{-(\Delta G^o - n\hbar\omega + \lambda_s)^2}{4\lambda_s kT}\right)$$

where the nuclear Franck-Condon factors for a given vibrational mode between the n=0 ground vibrational state of D–A ($kt << \hbar\omega$) and the n^{th} vibrational state of D^+–A^- are show in Equation 1.12 [68-70].

Equation 1.12.
$$|\langle 0|n\rangle|^2 = \left(\frac{S^n}{n!}\right)\exp(-S)$$

where $S = \lambda_i/\hbar\omega$ is the dimensionless distortion parameter for the vibrational mode of frequency $\hbar\omega$.

Finally, the ET rate constant for weakly coupled systems, where all nuclear coordinates are treated quantum mechanically, is given by Equation 1.13.

Equation 1.13.
$$k_{ET} = \frac{2\pi}{\hbar} H_{AB}^2 (FC)$$

where FC is the Franck-Condon factor which is the Boltzmann weighted sum of products of the reactants and products vibrational and solvent wavefunctions [74,75]. In the high temperature limit ($kT >> \hbar\varpi$) Equation 13 reduces to the activated rate equation (Equation 1.7).

Adiabatic–Nonadiabatic Transition Models

The transition between the adiabatic ($\kappa \bullet 1$) and nonadiabatic ($\kappa << 1$) coupling regimes for electron transfer was described by Jortner [76-78].

Equation 1.13.

$$k_{ET} = \frac{k_{NA}}{1+\kappa_A} = \frac{\left(\frac{4\pi^3}{h^2 \lambda kT}\right)^{1/2} H_{AB}^2 \exp\left(\frac{-(\Delta G^o + \lambda)^2}{4\lambda kT}\right)}{1+\frac{8\pi^2 H_{AB}^2 \tau_L}{h\lambda}}$$

The most notable feature is the denominator, which contains an adiabaticity factor, κ_A. When H_{AB} is small, the denominator is unity and the expression reduces to the nonadiabatic equation (Equation 1.7). When H_{AB} is large, such that the adiabaticity factor is much greater than one, the H_{AB} terms cancel and the prefactor becomes inversely proportional to the longitudinal dielectric solvent relaxation time (τ_L). These considerations set an upper limit on the ET rate. However, several violations of the theoretical predictions of solvent controlled ET have been reported and cannot be reconciled with current theoretical treatments [79-85].

Intervalence Band Analysis

In 1967 Hush developed a theory that predicts ET parameters from analysis of metal-to-metal-charge-transfer (MMCT) bands, which are exhibited by moderately to strongly-coupled mixed-valence complexes [86]. From the MMCT band, both H_{AB} and λ can be determined. The reorganization energy can be determined by:

Equation 1.14.

$$\lambda = E_{op} - \Delta G^o$$

where E_{op} is the energy at the maximum of the MMCT absorption band. ΔG^{o} can be obtained by measuring the redox potentials of the donor and acceptor moieties.

The electronic coupling parameter can be obtained from:

Equation 1.15. $$H_{AB} = 2.05\times10^{-2}\left[\frac{\varepsilon_{\max}\Delta\bar{\nu}_{1/2}}{\bar{\nu}_{\max}}\right]\frac{\bar{\nu}_{\max}}{r}$$

where ε_{max} (M^{-1} cm^{-1}) is the molar extinction coefficient at the MMCT absorption band maximum, $\Delta\bar{\nu}_{1/2}$ (cm^{-1}) is the full-width at half-height of the MMCT band, $\bar{\nu}_{\max}$ (cm^{-1}) is energy at the band maximum, and r (Å) internuclear distance between the redox sites. Until the advent of ultrafast kinetics measurements, strongly-coupled ET could only be studied using this theoretical treatment on molecules amenable to MMCT.

Initiating ET

There are three main ET processes relevant to the topics contained in this thesis. These include [39]:

1. Thermally activated ground-state ET proceeding through the transition state; the designation ground-state indicates that the transition state involves the two lowest-lying states of the system. This process can be initiated by mixing donor and acceptor molecules in a reaction vessel.

2. Optical ET (often designated as intervalence- or metal-to-metal charge transfer for binuclear mixed-valence transition metal complexes), occurring vertically from the equilibrium configuration of the initial state. Absorption of light in the energy range of the MMCT band initiates the optical ET (see page 28).

3. Photoinduced ET, where photoexcitation generates an excited state that presents a good donor and acceptor for ET. Photoinduced charge separation is a thermally activated process and, in general, is followed by thermal charge recombination back to the ground state.

References

[1] L Stryer, *Biochemistry*, 3rd edn., Freeman, San Francisco (1995).

[2] H Michel, O Epp, J Deisenhofer, *EMBO J.*, **5**, 2445 (1986).

[3] J Deisenhofer, O Epp, I. Sinning, H Michel, *J. Mol. Biol.*, **246**, 429-457 (1995).

[4] *Chem. Phys.*, **197**, 223-472 (1995) ME Michel-Beyerle, GJ Small, Eds., Special Issue on Photosynthesis and the Bacterial Reaction Center.

[5] M Bixon, J Fejer, G Feher, JH Freed, D Gamliel *et al., Isr. J. Chem.*, **32**, 369-518 (1992).

[6] MA Steffen, KQ Lao SG Boxer, *Science*, **264**, 810-816 (1994).

[7] BA Heller, D Holten, C Kirmaier, *Science*, **269**, 940-945 (1995).

[8] HB Gray, JR Winkler, *Annu. Rev. Biochem.*, **65**, 537-561 (1996).

[9] HB Gray, JR Winkler, *J. Biol. Inorg. Chem.*, **2**,.399-404 (1997).

[10] DN Beratan, JN Onuchic, JJ Hopfield, *J. Chem. Phys.*, **86**, 4488-4498 (1987).

[11] JN Onuchic, DN Beratan, *J. Chem. Phys.*, **92**, 722-733 (1990).

[12] JN Onuchic, DN Beratan, JR Winkler, HB Gray, *Annu. Rev. Biophys. Biomol. Struct*, **21**, 349-377 (1992).

[13] DN Beratan, JN Betts, JN Onuchic, *J. Phys. Chem.*, **96**, 2852-2855 (1992).

[14] DN Beratan, JN Betts, JN Onuchic, *Science*, **252**, 1285-1288 (1991).

[15] MR Wasielewski,*Chem. Rev.*, **92**, 435-461 (1992).

[16] KD Jordan, MN Paddon-Row, *Chem. Rev.*, **92**, 395-410 (1992).

[17] M Bixon, J Jortner, *Adv. Chem. Phys.*, **106**, 35-202. (1999).

[18] D Astruc, *Acc. Chem. Res.*, **30**, 383-391 (1997).

[19] MC Petty, *Meas. Sci. Tech.*, **7**, 725-735 (1996).

[20] CA Mirkin, MA Ratner, *Annu. Rev. Phys. Chem.*, **43**, 719-754 (1992).

[21] JR Heath, PJ Kuekes, GS Snider *et al.*, *Science*, **280**, 1716-1721 (1998).

[22] WM Tolles, *ACS Sym. Ser.*, **622**, 1-18 (1996).

[23] RA Marcus, N Sutin, *Biochim. Biophys. Acta*, **811**, 265-322 (1985).

[24] RA Marcus, *J. Chem. Phys.*, **24**, 966-978 (1956).

[25] RA Marcus, *Annu. Rev. Phys. Chem.*, **15**, 155-196 (1964).

[26] RA Marcus, *Faraday Disc.*, **74**, 7-15 (1982).

[27] RA Marcus, *J. Chem. Phys.*, **43**, 679-701 (1965).

[28] N Sutin, *Prog. Inorg. Chem.*, **30**, 441 (1983).

[29] JR Miller, LT Calcaterra, GL Closs, *J. Am. Chem. Soc.*, **106**, 3047 (1984).

[30] N Sutin, BS Brunschwig, C Creutz, JR Winkler, *Pure Appl. Chem.*, **60**, 1817-1829 (1988).

[31] JJ Hopfield, *Oxidases and Related Redox Systems*, JJ Hopfield, Ed., Pergamon Press: Oxford, 3-19 (1982).

[32] JJ Hopfield, *Electrical Phenomena at the Biological Membrane Level*, JJ Hopfield, Ed., Elsevier: New York, 471-492 (1977).

[33] HM McConnell, *J. Chem. Phys.*, **35**, 508-515 (1961).

[34] C Liang, MD Newton, *J. Phys. Chem.*, **96**, 2855-2866 (1992).

[35] C Liang, MD Newton, *J. Phys. Chem.*, **97**, 3199-3211 (1993).

[36] A Broo, S Larsson, *Chem. Phys.*, **148**, 103-115 (1990).

[37] LA Curtiss, CA Naleway, JR Miller, *Chem. Phys.*, **176**, 387-405 (1993).

[38] KD Jordan, MN Padden-Row, *Chem. Rev.*, **92**, 395-410 (1992).

[39] MD Newton, *Adv. Chem. Phys.*, **106**, 303-375 (1999).

[40] JJ Hopfield, *Proc. Natl. Acad. Sci.*, **71**, 3640-3644 (1974).

[41] H Oevering, MN Paddon-Row, M Heppener, AM Oliver, E Cotsaris, JW Verhoeven, NS Hush, *J. Am. Chem. Soc.*, **109**, 3258-3269 (1987).

[42] MD Johnson, JR Miller, NS Green, GL Closs, *J. Phys. Chem.*, **93**, 1173-1176 (1989).

[43] TS Arrhenius, M Blancharddesce, M Dvolaitzky, JM Lehn, J Malthete, *Proc. Natl. Acad. Sci.*, **83**, 5355-5359 (1986).

[44] MR Wasielewski, in *Photochemical Energy Conversion*, (Ed. JR Norris), 135-147 (1989).

[45] F Effenberger, HC Wolf, *New J. Chem.*, **15**, 117-123 (1991).

[46] LM Tolbert, *Acct. Chem. Res.*, **25**, 561-568 (1992).

[47] JM Tour, *Chem. Rev.*, **96**, 537-553 (1996).

[48] V Grosshenny, A Harriman, R Ziessel, *Angew. Chem. Int. Edn. Engl.*, **34**, 2705-2708 (1996).

[49] SB Sachs, SP Dudek, RP Hsung, LR Sita, JF Smalley, MD Newton, SW Feldberg, CED Chidsey, *J. Am. Chem. Soc.*, **119**, 10563-10564 (1997).

[50] A Helms, D Heiler, G McLendon, *J. Am. Chem. Soc.*, **114**, 6227-6238 (1992).

[51] AC Ribou, JP Launay, K Takahashi, T Nihira, S Tarutani, CW Spangler, *Inorg. Chem.*, **33**, 1325-1329 (1994).

[52] JR Winkler, HB Gray,*Chem. Rev.*, 369-379 (1992).

[53] CC Moser, JM Keske, K Warncke, RS Farid, PL Dutton, *Nature*, **355**, 796-802 (1992).

[54] FD Lewis, TF Wu, YF Zhang, RL Letsinger, SR Greenfield, MR Wasielewski, *Science,* 673-676 (1997).

[55] RE Holmlin, PJ Dandliker, JK Barton, J.K *Angew. Chem. Int. Edn. Engl.*, **36**, 2715-2730 (1998).

[56] JR Miller, JA Peeples, MJ Schmitt, GL Closs, *J. Am. Chem. Soc.*, **104**, 6488 (1982).

[57] T Guarr, ME McGuire, G McLendon, *J. Am. Chem. Soc.*, **107**, 5104 (1985).

[58] JM Lawson, DC Craig, MN Paddon-Row, J Kroon, JW Verhoeven, *Chem. Phys. Lett.*, **164**, 120-125 (1989).

[59] GL Closs, LT Calcaterra, NJ Green, KW Penfield, JR Miller, *J. Phys. Chem.*, **90**, 3673-3683 (1986).

[60] JF Smalley, SW Feldberg, CED Chidsey, MR Linford, MD Newton, Y-P Liu, *J. Phys. Chem.*, **99**, 13141-13149 (1995).

[61] MJ Shephard, MN Paddon-Row, KD Jordan, *Chem. Phys.*, **176**, 289-304 (1993).

[62] P Siders, RA Marcus, *J. Am. Chem. Soc.*, **103**, 748-752 (1981).

[63] P Siders, RA Marcus, *J. Am. Chem. Soc.*, **103**, 741-747 (1981).

[64] RA Marcus, *J. Phys. Chem.*, **86**, 622-630 (1982).

[65] GL Closs, JR Miller, *Science,* **240**, 440-447 (1988).

[66] RS Farid, IJ Chang, JR Winkler, HB Gray,*J. Phys. Chem.*, **98**, 5176-5179 (1994).

[67] VG Levich, RR Dogonadze, *Collect. Czech. Chem. Commun.*, **26**, 193 (1961).

[68] MA Vorotyntsev, RR Dogonadze, AM Kuznetsov, *Phys. Status Solidi B*, **54**, 125 (1972).

[69] MA Vorotyntsev, RR Dogonadze, AM Kuznetsov, *Phys. Status Solidi B*, **54**, 425 (1972).

[70] RR Dogonadze, AM Kuznetsov, MA Vorotyntsev, MG Zakaraya, *J. Electroanal. Chem.*, **75**, 315 (1977).

[71] J Ulstrup, *Charge Transfer Processes in Condensed Media*, Springer-Verlag, Berlin (1979).

[72] D DeVault, *Quantum Mechanical Tunneling in Biological Systems*, Cambridge University Press, Cambridge, UK (1984).

[73] AM Kuznetsov, *Charge Transfer in Physics, Chemistry, and Biology*, Gordon and Breach, Reading, UK (1995).

[74] N Sutin, *Prog. Inorg. Chem.*, **30**, 441-498.

[75] VG Levich, RR Dogonadze, *Dokl. Acad. Nauk SSSR*, **124**, 123-126.

[76] M Bixon, J Jortner, *Chem. Phys.*, **176**, 467-481 (1993).

[77] J Jortner, M Bixon, *J. Chem. Phys.*, **88**, 167-170 (1988).

[78] I Rips, J Jortner, *J. Chem. Phys.*, **87**, 2090-2104 (1987).

[79] T Haberle, J Hirsch, F Polinger, H Heitele, ME Michel-Beyerle, C Andres, A Dohling, C Krieger, A Ruckermann, HA Staab, *J. Phys. Chem.*, **100**, 18269 (1996).

[80] E Akesson, AE Johnson, NE Levinger, GC Walker, TP DuBruil, PF Barbara, *J. Chem. Phys.*, **96**, 7859 (1992).

[81] K Tominaga, DAV Kliner, AE Johnson, NE Levinger, PF Barbara, *J. Chem. Phys.*, **98**, 1228 (1993).

[82] GC Walker, PF Barbara, SK Doorn, JT Hupp,*J. Phys. Chem.*, **95**, 5712 (1991).

[83] T Kobayashi, Y Takagi, H Kandori, K Kemnitz, K Yoshihara, *Chem. Phys. Lett.*, **180**, 416 (1991).

[84] H Pal, Y Nagasawa, K Tominagam, K Yoshihara, *J. Phys. Chem.*, **100**, 11964 (1996).

[85] M Seel, S Engleitner, W Zinth, *Chem. Phys. Let.*, **275**, 363 (1997).

[86] NS Hush, *Electrochim. Acta*, **13**, 1005-1023 (1968).

Chapter 2

Electron Transfer in Strongly-Coupled Dinuclear Ruthenium Complexes

Abstract

The absorption, luminescence, and transient-absorption spectra of $[(bpy)(tpy)Ru^{II}(CN)]^{+}$ (bpy = 2,2'-bipyridine; tpy = 2,2':6,2''-terpyridine) and $[(bpy)(tpy)Ru^{II}CNRu^{II,III}(NH_3)_5]^{3+,4+}$ have been measured. Metal-to-ligand charge-transfer (MLCT) excitation of the monomer produces an excited state that decays with a rate constant of 1.3×10^8 s^{-1}. Picosecond excitation of $[(bpy)(tpy)Ru^{II}CNRu^{III}(NH_3)_5]^{4+}$ does not lead to any detectable transients, indicating that relaxation rate constants are greater than 10^{12} s^{-1}. A transient attributable to $[(bpy)(tpy^{\bullet-})Ru^{II}CNRu^{III}(NH_3)_5]^{3+}$ is observed following picosecond excitation of $[(bpy)(tpy)Ru^{II}CNRu^{II}(NH_3)_5]^{3+}$; this intermediate decays *via* intramolecular ET with a rate constant of 3.8×10^{10} s^{-1}. Quantum-mechanical descriptions of the nuclear reorganization accompanying ET are required to explain the observed kinetics. ET parameters have been extracted from an analysis based on Hush theory of the intense intervalence charge-transfer absorption band present in the mixed-valence $[(bpy)(tpy)Ru^{II}CNRu^{III}(NH_3)_5]^{4+}$ complex.

Introduction

Electron transfer (ET) in strongly-coupled bimetallic mixed-valence complexes gives rise to an intense charge-transfer absorption transition. These absorption bands have been assigned to metal-to-metal charge-transfer transitions (MMCT) and are generally found in the near-infrared region [1]. The strong coupling that gives rise to the charge-transfer bands also leads to ET kinetics on the pico- to femtosecond time scale. Due to the difficulty of measuring kinetics in that time regime, only few ET kinetics studies of strongly-coupled dinuclear transition metal complexes exist.

For 25 years, ET in strongly-coupled mixed-valence complexes has been studied indirectly using the theoretical framework developed by Mulliken and Hush [2-4]. According to their theory, ET parameters such as the reorganization energy (λ) and the electron coupling matrix element (H_{AB}) can be gleaned from the MMCT absorption band energy maximum and area, respectively. Using this theoretical model, Stein and Taube measured the first distance dependence of the electronic coupling in a series of dinuclear ruthenium complexes [5,6]. Since then, many aspects of strongly coupled ET have been probed using MMCT band analysis. The direct measurement of ET kinetics, however, has only become possible in light of advances in laser technology over the last 15 years.

In an early study, it was reported that $Ru^{II} \rightarrow pz$ (pz = pyrazine) charge-transfer excitation in $[(H_3N)_5Ru^{II}(pz)Ru^{III}(edta)]^+$ produces a small yield of $[(H_3N)_5Ru^{III}(pz)Ru^{II}(edta)]^+$ that subsequently relaxes by intramolecular ET with a rate constant of 8×10^9 s^{-1} [7]. However, direct MMCT excitation of this dinuclear complex produced no detectable transient species. More recent work has focused on the $(H_3N)_5M^{III}(CN)Ru^{II}(CN)_5^-$ (M = Fe, Ru) ions. Femtosecond transient absorption [8-10] and picosecond infrared [11] measurements indicate that charge recombination following MMCT excitation in these dimers is extremely rapid (<1 ps), proceeding on the same timescale as solvent relaxation. In addition, this study found that the initial charge-transfer places large amounts of energy directly into the RuCN stretching mode so that photoinduced ET occurs between the reactant and a vibrationally excited product. Both studies emphasize that, while band shape analysis is qualitatively useful, quantitative predictions of rates have been unsuccessful. The rates measured by ultrafast spectroscopy are orders of magnitude faster than predicted by band shape analysis. This indicates that

the ET properties of the complexes need to be described with quantum mechanical ET models.

We have opted for an alternative approach to the study of ET in strongly coupled D(br)A systems, where (br) is the bridge. ET can be initiated in D(br)A complexes by local excitation of D (or A) rather than by direct D $\rightarrow$ A charge-transfer excitation. The locally excited species, being both better electron donors and acceptors than the ground-state complexes, can initiate a sequence of ET reactions. We have taken advantage of this approach to study intramolecular ET in the binuclear metal complexes $[(bpy)(tpy)Ru^{II}(CN)Ru^{II,III}(NH_3)_5]^{3+,4+}$ (bpy = 2,2'-bipyridine; tpy = 2,2':6,2'' -terpyridine). Metal-to-ligand charge-transfer (MLCT) excitation of the Ru^{II}-imine moiety can initiate intramolecular electron-transfer reactions with the Ru-ammine partner. In principle, four distinct intramolecular ET reactions can be studied using this technique.

Experimental

Synthesis and Characterization

Reagent-grade solvents were used for synthesis without further purification. UV-grade acetonitrile was distilled over CaH_2 prior to use for all spectroscopic measurements.

$[(bpy)(tpy)Ru^{II}(CN)](PF_6)$. This compound was prepared as previously described [12], and characterized by UV-Vis spectroscopy and elemental analysis (Calc: C 45.96; H 3.12; N 12.40; Found: C 46.00; H 3.21; N 12.40). The chloride salt was prepared by dissolving the PF_6 complex in acetone and precipitating with tetrabutyl ammonium chloride ((TBA)Cl).

[(bpy)(tpy)Ru^{II}(CN)Ru^{III}(NH$_3$)$_5$](PF$_6$)$_4$. This compound was prepared using a modified, published procedure [13]. [Ru(NH$_3$)$_5$Cl]Cl (62 mg, 0.212 mmol, Strem Chemical Company) was added to H_2O (20 ml) in a round-bottom flask fitted with a solids-addition arm containing freshly prepared Zn(Hg). The solution was deoxygenated before a few drops of 0.1 M trifluoromethanesulfonic acid were added. The Zn(Hg) was added, and the mixture was stirred at room temperature for one hour to yield [Ru(NH$_3$)$_5$(OH$_2$)]$^{2+}$. The solution was transferred *via* cannula into a Schlenk frit attached to a flask containing [(tpy)(bpy)Ru^{II}(CN)]Cl (100 mg, 0.175 mmol) in H_2O (10 ml). The filtered mixture of [Ru(NH$_3$)$_5$(OH$_2$)]$^{2+}$ and [(tpy)(bpy)Ru^{II}(CN)]$^{+}$ was stirred 4-6 hours at room temperature in the dark under an argon atmosphere. After this period, the reaction mixture was exposed to air, producing the green mixed-valence [(tpy)(bpy)Ru^{II}(CN)Ru^{III}(NH$_3$)$_5$]$^{4+}$ complex. This air-stable compound was purified by ion-exchange chromatography on Sephadex SP C-25 (3×10 cm column) using aqueous LiCl as the eluant. The green fraction was collected, precipitated with NH_4PF_6, filtered, washed twice with water, and dried over P_2O_5 in a vacuum desiccator. Yield 55% (Calc: C 23.68; H 2.91; N 11.68; Found: C 23.72; H 3.00; N 11.55).

[(bpy)(tpy)Ru^{II}(CN)Ru^{II}(NH$_3$)$_5$](PF$_6$)$_3$. [(bpy)(tpy)Ru^{II}(CN)Ru^{III}(NH$_3$)$_5$](PF$_6$)$_4$ was dissolved in acetone and precipitated as the chloride salt with (TBA)Cl. An aqueous solution of this compound was reduced with excess sodium ascorbate under Ar. The resulting red-brown solution was transferred *via* cannula into a Schlenk frit attached to a flask. A red-brown product was precipitated with excess NH_4PF_6 and filtered. The solid was washed twice with degassed H_2O, dried in vacuum and stored in a glove box to

prevent air oxidation. Yield 90% (Calc: C 26.61; H 3.26; N 13.13; Found: C 26.32; H 3.03; N 13.18).

Crystal Structure

Crystals of $[(bpy)(tpy)Ru^{II}(CN)Ru^{III}(NH_3)_5](PF_6)_4$ were grown from a 1:1 solution of water/acetone by slow evaporation in air at ambient conditions. The data were acquired at room temperature with an Enrat Nonius CAD4 diffractometer using Mo K_α radiation and ω-scans.

Absorption and Luminescence Spectroscopy

UV-Vis-NIR spectra were obtained using a modified Cary14 spectrometer (Olis) under PC control.

Relative luminescence quantum yields were measured with a Hitachi 4500 fluorimeter. All samples were thoroughly degassed prior to data collection, and had absorbencies of approximately 0.1 at the 450-nm excitation wavelength. The luminescence from $[Ru(bpy)_3](PF_6)_2$ in acetonitrile, attenuated with a neutral density filter (A = 1.0), was used as the standard for quantum-yield determinations (ϕ_{em} = 0.06) [14]. Luminescence from the ruthenium dimers could not be detected even at very high solute concentrations (0.1 mM).

Electrochemistry and Spectroelectrochemistry

Electrochemical data were measured with a Bioanalytical Systems 100 electrochemical analyzer. Square-wave voltammetry experiments were performed at room temperature in degassed acetonitrile containing 0.3 M $(TBA)PF_6$. A carbon electrode was

used as the working electrode, a saturated calomel electrode (SCE) was used as the reference electrode, and ferrocene was used as an internal standard (Fe^{3+}/Fe^{2+} $E_{½}$ = 400 mV *vs.* NHE) [15]. All reported potentials are referenced to NHE.

Spectroelectrochemical measurements were performed with the BAS-100 electrochemical analyzer and a Hewlett Packard 8452A diode array UV-Vis spectrometer. Samples were dissolved in 0.3 M $(TBA)PF_6$/acetonitrile solutions and degassed with N_2. Amorphous carbon was used as the working electrode for bulk electrolyses in a modified 1 cm quartz cuvette. Sample reduction was performed at −1.6 V *vs.* NHE.

Picosecond Transient Absorption Spectroscopy

Picosecond pulses are generated by seeding a Continuum RGA60 Nd:YAG regenerative amplifier with the output of a Coherent Antares laser (1064 nm) that was chirped in 100 m of single-mode optical fiber. The pulses from the RGA60 oscillator (10 Hz) pass through a grating-pair pulse compressor, then are amplified in a single-pass Nd:YAG amplifier. The pulses (20 mJ, 1064 nm, 10 ps) from the amplifier are separated with a polarizing beamsplitter to form the pump and probe legs for the transient-absorption experiment.

Sample pump is generated either by doubling the Nd:YAG fundamental to form 532 nm pulses (~500 μJ), or by using the 355 nm third harmonic to produce 416 nm pulses (~200 μJ) by stimulated Raman scattering in H_2 (800 psi, 1 m path).

The probe-light timing relative to the pump is controlled by passing the 532 nm pulses four times over an 8 ft delay stage. Supercontinuum probe light is generated by focusing the 532 nm beam into a mixture of D_2O, H_2O, and H_2SO_4 [24]. The resulting

broadband continuum probe light is focused onto a 400 μm aperture, and then is separated into sample and reference beams. The former passes through the sample excitation volume before being focused onto the entrance slit of a 0.275 m spectrograph (Acton Research). The reference beam bypasses the sample and directly enters the spectrograph entrance slit about 2.5 mm below the sample-beam image. Sample and reference beam intensities are measured using a dual diode-array detector (Princeton Instruments DPDA-1024). The data are transferred to a PC where home-written control software calculates optical-density changes and stores the data.

In order to minimize degradation, all the samples were dissolved in degassed, dry acetonitrile, and flowed through a 1 mm path quartz cell. The instrument temporal response was determined by measuring the transient kinetics of iron(octaethyl porphyrin) (532 nm pump) and horse heart cytochrome *c* (416 nm pump). The bleach of the Soret absorption in cytochrome *c* was fit to a Gaussian function with FWHM of 17.6 ps. This function was convoluted with exponential-decay functions and fit to kinetics data using a Matlab program. Details of the picosecond transient-absorption instrument can be found in the thesis of Dr. Max Bachrach, Caltech (1996).

Results

Absorption and Luminescence Spectra

The absorption spectra of $[(bpy)(tpy)Ru^{II}(CN)]^{+}$, $[(bpy)(tpy)Ru^{II}(CN)Ru^{II}(NH_3)_5]^{3+}$, and $[(bpy)(tpy)Ru^{II}(CN)Ru^{III}(NH_3)_5]^{4+}$ are shown in Figure 2.1 and the spectroscopic parameters are summarized in Table 2.1. We have found that small amounts of impurities dramatically alter the spectra of these compounds;

Figure 2.1 UV-Vis spectra in acetonitrile, at 22 °C, of (- - - -)[(bpy)(tpy)Ru^{II}(CN)]$^{+}$, (——)[(bpy)(tpy)Ru^{II}(CN)$Ru^{II}$$(NH_3)_5$]$^{3+}$, and (— —)[(bpy)(tpy)$Ru^{II}(CN)Ru^{III}$$(NH_3)_5$]$^{4+}$.

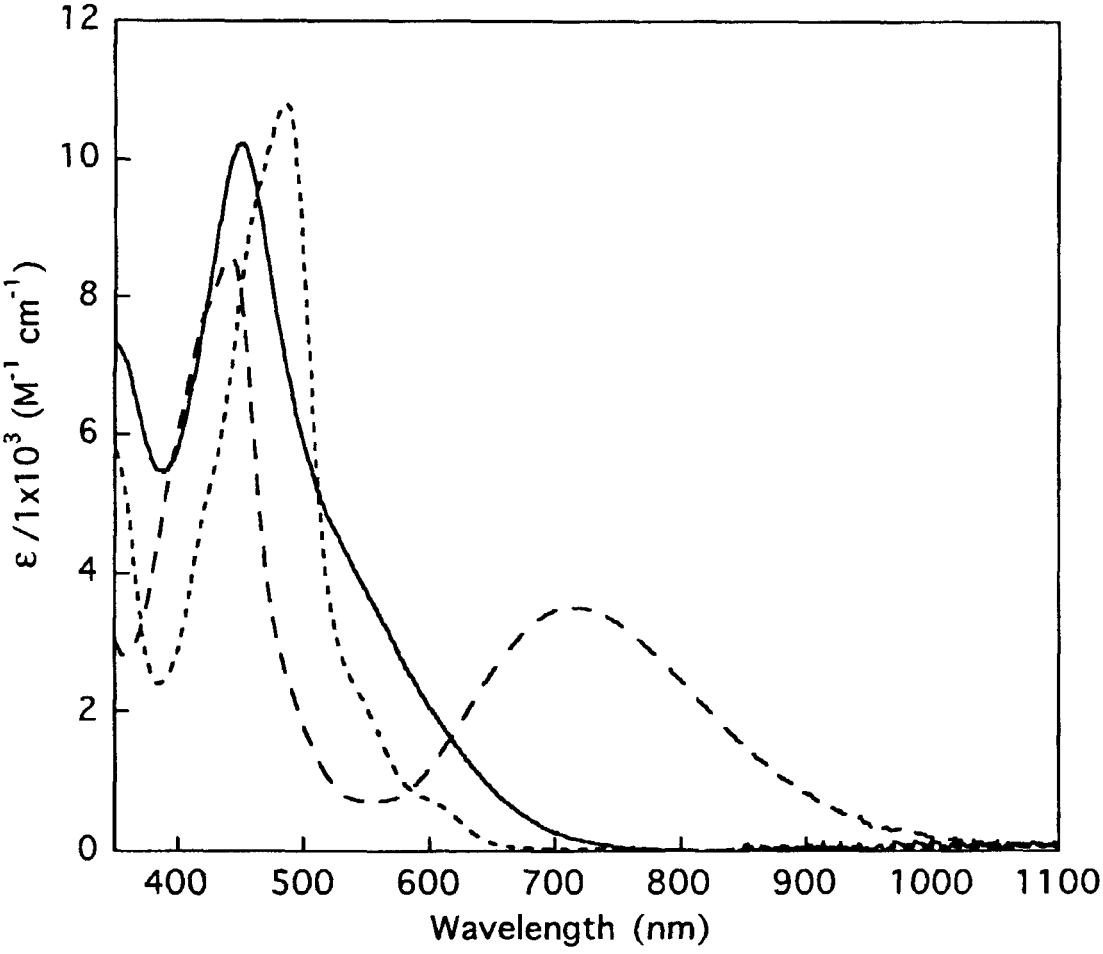
12
10
8
6
4
2
0
ε /1x10³ (M⁻¹ cm⁻¹)
400
500
600
700
800
900
1000
1100
Wavelength (nm)

Table 2.1 Spectroscopic properties of ruthenium complexes.

Complex	Absorption λ_{max} (nm)	Assignment	Emission λ_{max} (nm) ‡	Quantum Yield Φ
$[(bpy)(tpy)Ru^{II}CN]^{+}$	485	MLCT	651	1.5×10^{-4}
$[(bpy)(tpy)Ru^{II}CNRu^{III}(NH_3)_5]^{4+}$	441	MLCT	†	†
	717	MMCT		
$[(bpy)(tpy)Ru^{II}CNRu^{II}(NH_3)_5]^{3+}$	451	MLCT	†	†

‡ Using 450 nm excitation.

† No detectable emission at room temperature inacetonitrile.

consequently, great care was taken to achieve a high degree of sample purity. Ru → bpy and Ru → tpy charge-transfer transitions dominate the absorption spectrum of $[(bpy)(tpy)Ru^{II}(CN)]^{+}$ (λ_{max} = 485 nm). Upon complexation with the ruthenium-pentaammine moiety to form $[(bpy)(tpy)Ru^{II}(CN)Ru^{II}(NH_3)_5]^{3+}$, the MLCT absorption loses intensity and shifts to the blue. Oxidation of this dimer to $[(bpy)(tpy)Ru^{II}(CN)Ru^{III}(NH_3)_5]^{4+}$ further attenuates the MLCT absorption and shifts the maximum slightly further to the blue. The striking feature in the $[(bpy)(tpy)Ru^{II}(CN)Ru^{III}(NH_3)_5]^{4+}$ absorption spectrum is an intense band in the red (λ_{max} = 717 nm, $\varepsilon = 3500\ M^{-1}\ cm^{-1}$).

Excitation (450 nm) of $[(bpy)(tpy)Ru\text{-}^{II}(CN)]^{+}$ in acetonitrile at room temperature produces MLCT luminescence with a quantum yield of 1.5×10^{-4}. No luminescence could be detected from either dinuclear complex.

X-Ray Structure

The compound crystallized as brown plates in the orthorhombic space group $C222_1$. The Ru–Ru and C–N distances are 5.11 Å and 1.18 Å, respectively. The PF_6 anions are disordered; there is also water present in the structure. The structure is rendered in Figure 2.2.

Electrochemistry and Spectroelectrochemistry

The electrochemical data are summarized in Table 2.2. All electrochemical potentials for the monomer and dimers correspond to fully reversible, one-electron processes. Oxidation of the monomer at 1.68 V *vs.* NHE is assigned to the $[(bpy)(tpy)Ru^{III/II}(CN)]^{2+/+}$ couple, while its reduction at −1.38 V is assigned to tpy anion-

Figure 2.2 Structure of the $[(bpy)(tpy)Ru^{II}(CN)Ru^{III}(NH_3)_5]^{4+}$ cation. Hydrogen atoms are omitted for clarity.

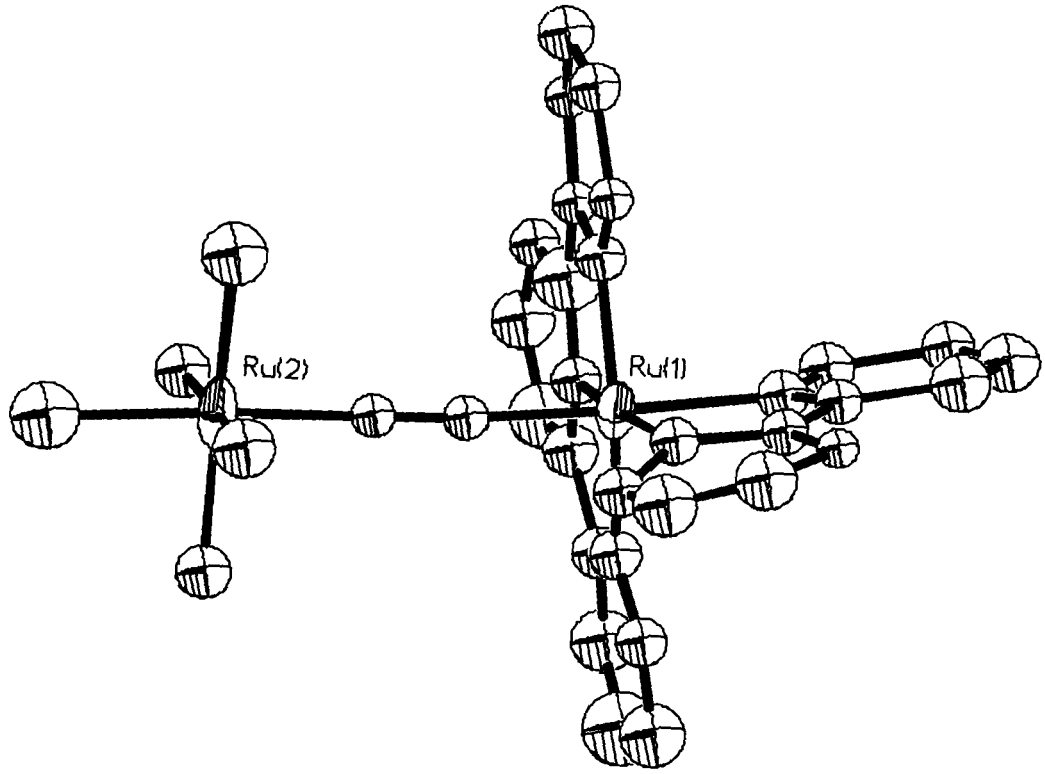
Ru(2)
Ru(1)

radical formation [12]. A second, reversible one-electron wave observed at −1.69 V can be attributed to the reduction of the neighboring bpy ligand. These ligand-based reductions occur at nearly the same potentials in the cyanide-bridged dimer (−1.40 V and −1.67 V). In contrast, the $Ru^{III/II}$-imine potential in the dimer is 380 mV lower than the corresponding potential in the monomer. The $Ru^{III/II}$-ammine potential (0.09 V) is quite close to that of $Ru(NH_3)_6^{3+/2+}$ in water (0.10 V) [16].

The spectra of the cyanide-bridged dinuclear Ru complex in its various oxidation states were determined using spectroelectrochemistry. The changes of the spectral feature upon reduction are particularly relevant to assignments of the features observed in the transient absorption experiments. Oxidation of the Ru-imine center to Ru^{III} bleaches the MLCT absorption features. The reduction of tpy produces an increase in absorbance from 340-470 nm but only a slight decrease and red shift of the MLCT absorption (Figure 2.3).

Picosecond Transient Absorption Spectroscopy

Picosecond excitation (λ_{ex} = 532 nm) of $[(bpy)(tpy)Ru^{II}(CN)]^+$ in acetonitrile at room temperature generates a transient species with a difference spectrum comprised of MLCT bleaching and increased absorbance that extends from 430 nm to higher energies (Figure 2.4). These features are consistent with those expected for a metal-to-ligand charge-transfer excited state [17]. This transient species decays to the ground state with a rate constant of 1.3×10^8 s^{-1} (τ = 7.9 ns) (Figure 2.5), which lies between the excited-state lifetimes of $Ru(bpy)_3^{2+}$ (600 ns) [28] and $Ru(tpy)_2^{2+}$ (0.25 ns) [18].

Excitation of the mixed-valence $[(bpy)(tpy)Ru^{II}(CN)Ru^{III}(NH_3)_5]^{4+}$ complex at 532 nm, 416 nm and 683 nm (MMCT band) yielded no detectable transients. Given the

Table 2.2 Electrochemical properties of ruthenium complexes. All redox couples are fully reversible, one-electron processes. Values are given *vs.* NHE.

Complex	$E_{1/2}Ru_b^{III/II}$ (V)	$E_{1/2}Ru_b^{II/I}$ (V)	$E_{1/2}Ru_a^{III/II}$ (V)
$[(bpy)(tpy)Ru_bCN]^+$	1.69	-1.39	—
$[(bpy)(tpy)Ru_bCNRu_a(NH_3)_5]^{n+}$	1.3	-1.40	0.09

Figure 2.3 Spectroelectrochemisty of $[(bpy)(tpy)Ru^{II}(CN)Ru^{II}(NH_3)_5]^{3+}$. Spectral changes associated with one electron reduction of $[(bpy)(tpy)Ru^{II}(CN)Ru^{II}(NH_3)_5]^{3+}$ in acetonitrile solution.

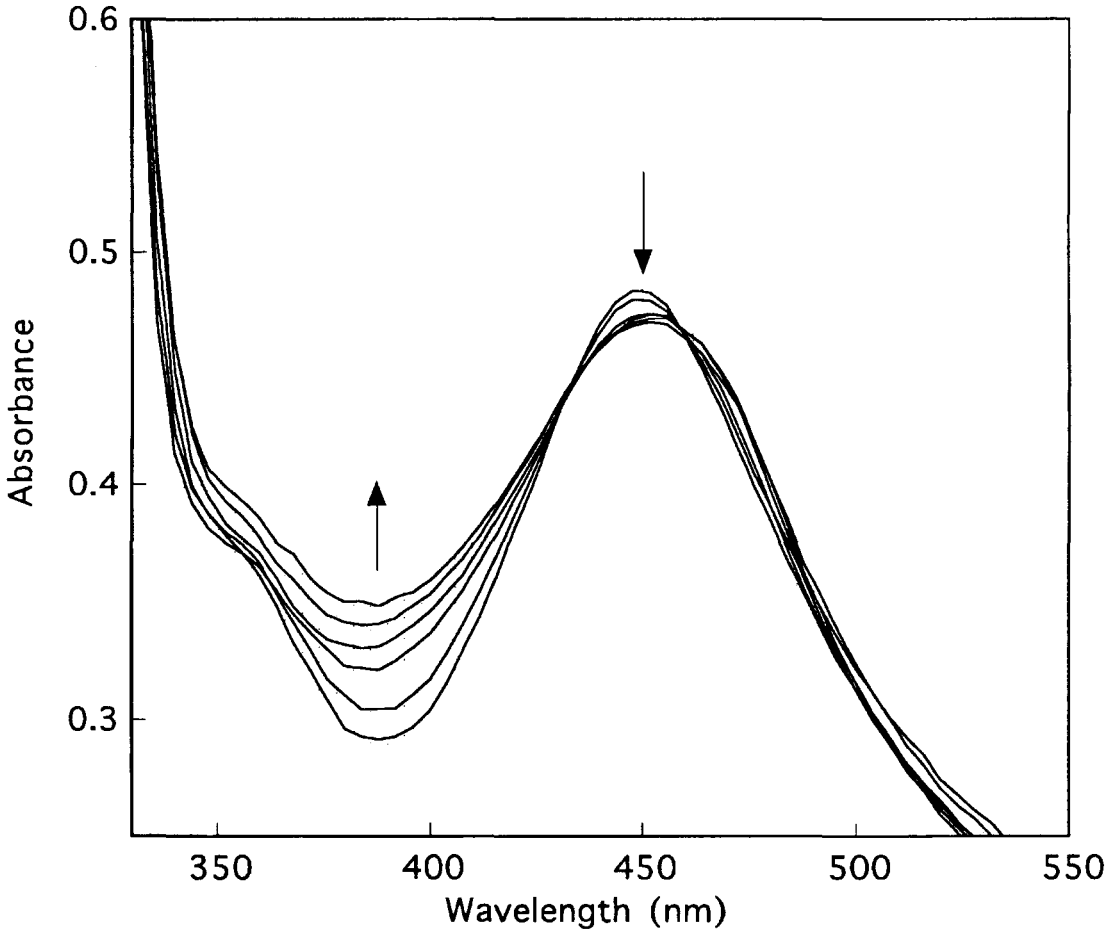
0.6
0.5
0.4
0.3
Absorbance
350
400
450
500
550
Wavelength (nm)

Figure 2.4 Transient difference spectra following picosecond excitation of (——) $[(bpy)(tpy)Ru^{II}(CN)]^{+}$ and (- - - -) $[(bpy)(tpy)Ru^{II}(CN)Ru^{II}(NH_3)_5]^{3+}$ in acetonitrile solution.

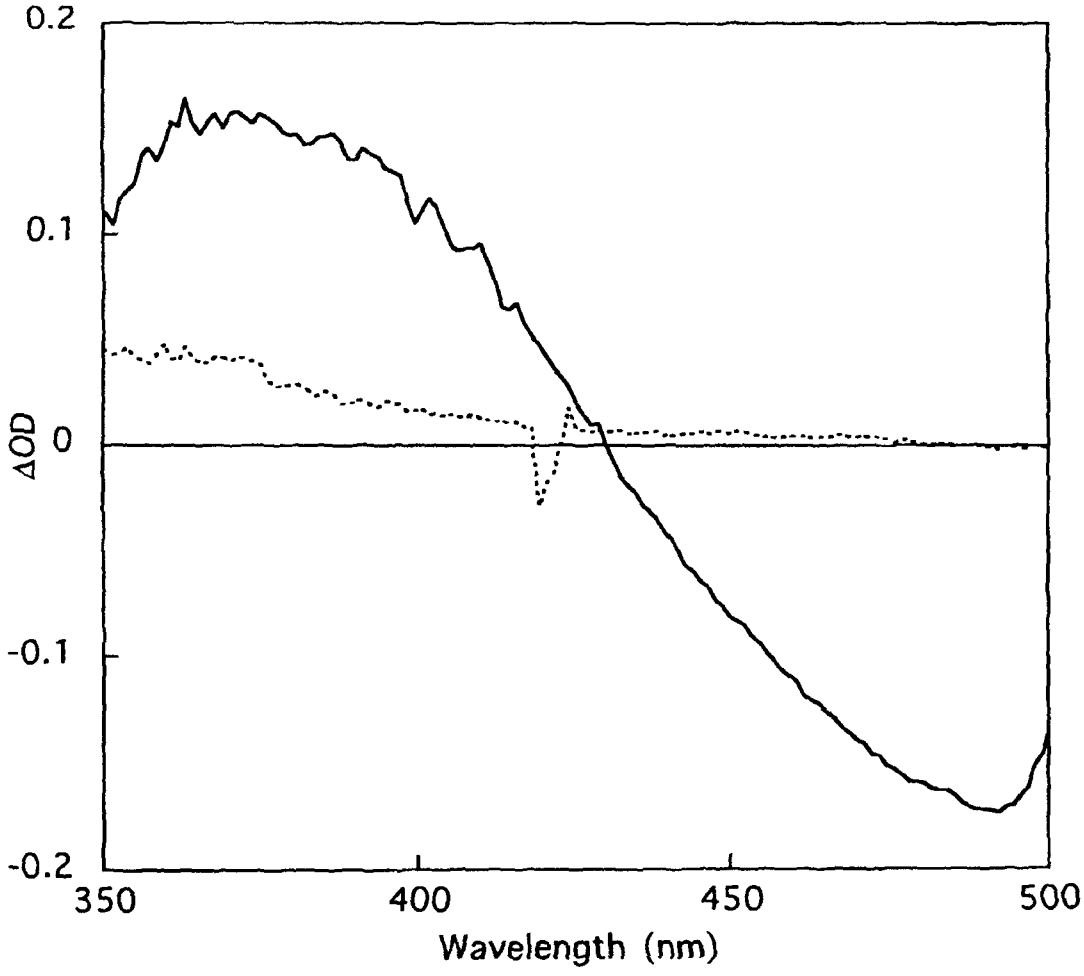
0.2
0.1
0
-0.1
-0.2
ΔOD
350
400
450
500
Wavelength (nm)

Figure 2.5 Transient absorption kinetics of $[(bpy)(tpy)Ru^{II}(CN)]^{+}$ excited at 532 nm in acetonitrile solution observed at (top) 480 nm and (bottom) 375 nm.

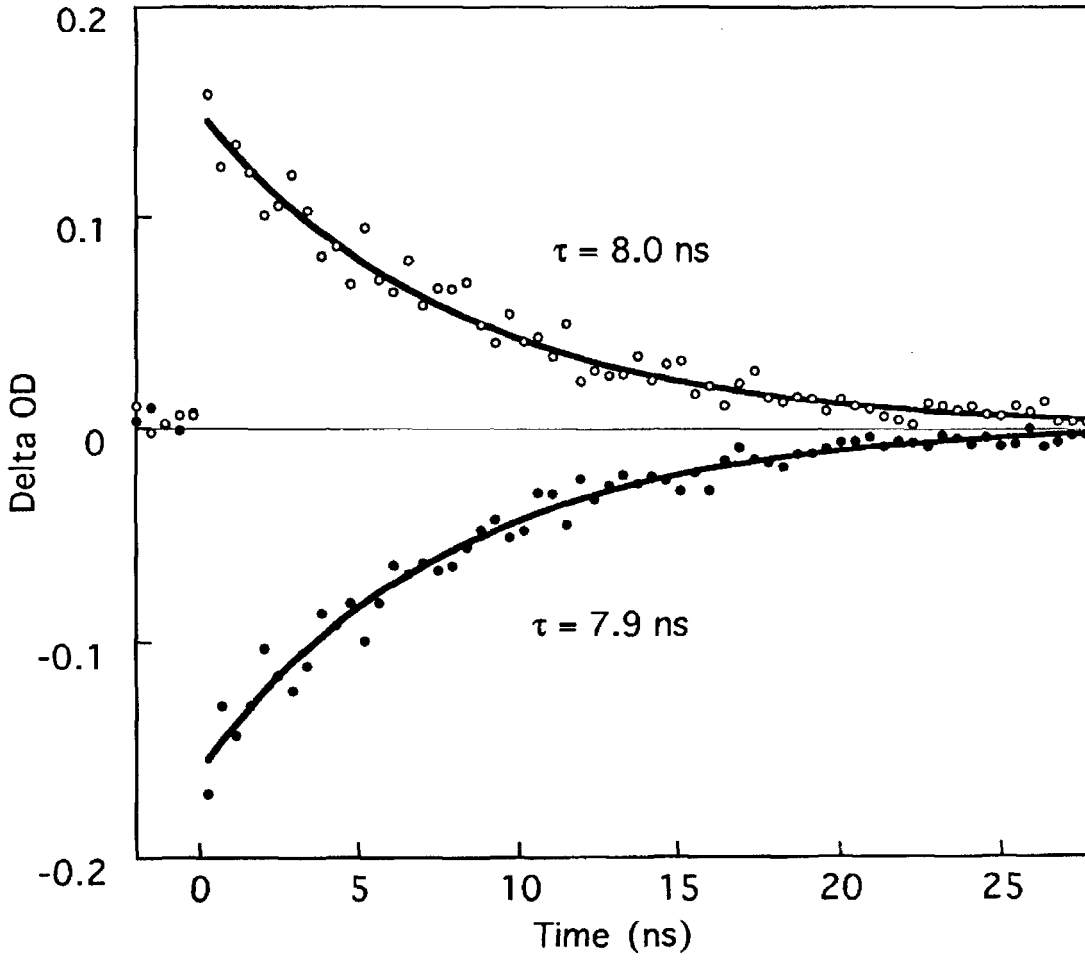
0.2
0.1
0
-0.1
-0.2
Delta OD
τ = 8.0 ns
τ = 7.9 ns
0
5
10
15
20
25
Time (ns)

Figure 2.6 Transient absorption kinetics of $[(bpy)(tpy)Ru^{II}(CN)Ru^{II}(NH_3)_5]^{3+}$ excited with 416 nm and observed at 370-375 nm in acetonitrile solution.

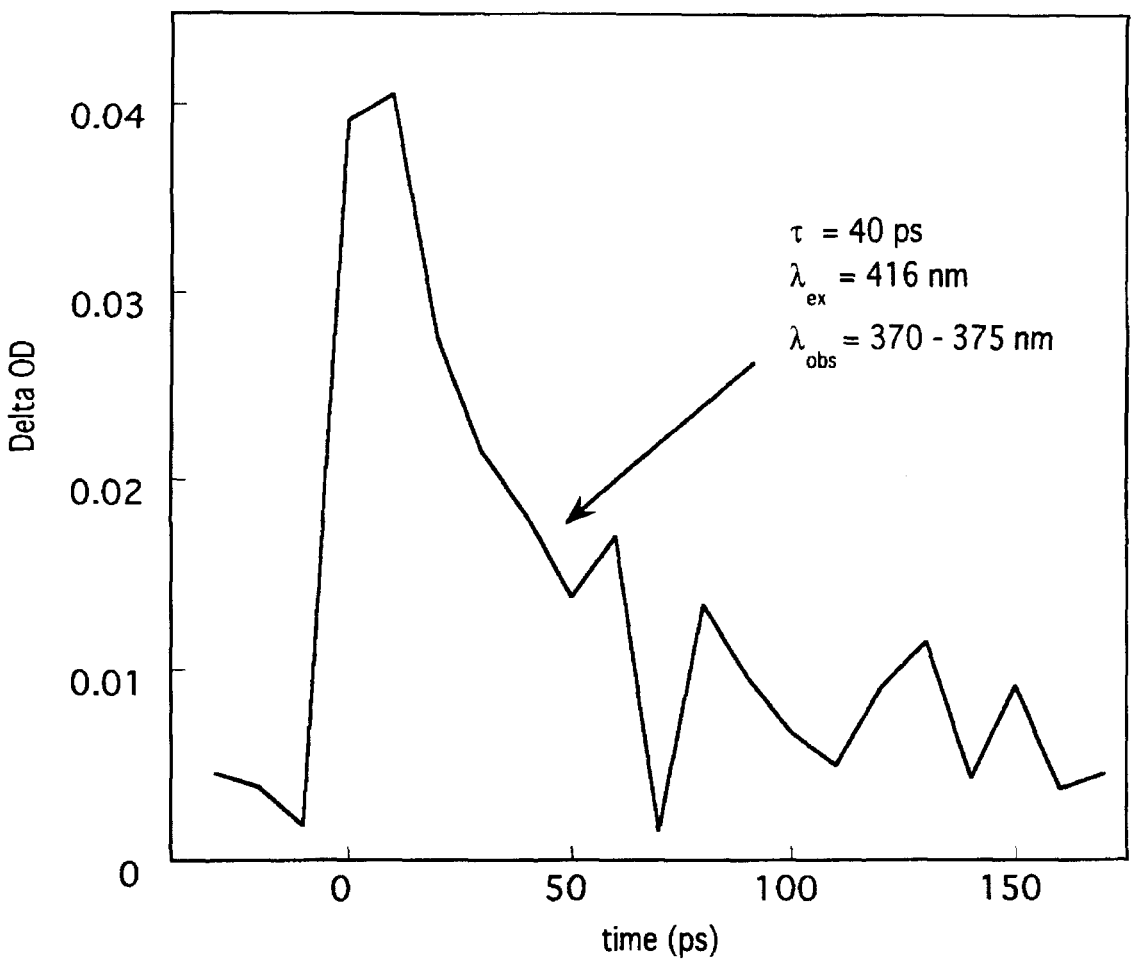
0.04
0.03
0.02
0.01
0
Delta OD
0
50
100
150
time (ps)
τ = 40 ps
λex = 416 nm
λobs = 370 - 375 nm

instrument response function, the transient spectrum of $[(bpy)(tpy)Ru^{II}(CN)]^{+}$, and a detection limit of 0.005, we can place an upper limit of 1 ps on the MLCT excited-state lifetime in $[(bpy)(tpy)Ru^{II}(CN)Ru^{III}(NH_3)_5]^{4+}$.

Excitation of $[(bpy)(tpy)Ru^{II}(CN)Ru^{II}(NH_3)_5]^{3+}$ generates a transient species characterized by a broad, weak absorbance increase near 360 nm (Figure 2.6) that decays with a rate constant of 3.8×10^{10} s^{-1} (τ = 26 ps) (Figure 2.7). No bleach of the MLCT absorption was detected in the transient spectrum of this dimer.

Discussion

The 717 nm absorption feature in $[(bpy)(tpy)Ru^{II}CNRu^{III}(NH_3)_5]^{4+}$ has been assigned previously to a $Ru^{II} \rightarrow Ru^{III}$ MMCT transition [13]. Analysis of this well-resolved absorption band provides information about the electronic-coupling strength and reorganization energy associated with this charge transfer [1]. The energy of the MMCT absorption maximum (1.73 eV) is equal to ($E_0 + \lambda$), where E_0 is the energy difference between $[(bpy)(tpy)Ru^{II}(CN)Ru^{III}(NH_3)_5]^{4+}$ and $[(bpy)(tpy)Ru^{III}(CN)Ru^{II}(NH_3)_5]^{4+}$. We can approximate E_0 using the electrochemical data; these measurements indicate that E_0 = 1.21 eV, leading to an estimate of λ = 0.52 eV. Studies of electron self-exchange reactions of Ru-diimine and Ru-ammine complexes suggest that the inner-sphere contribution to this reorganization energy will be $\lambda_i \sim 0.08$ eV [19]. The 0.44 eV balance is attributed to solvent reorganization (λ_S). Evaluation of the MMCT band by Hush theory [2] also provides an estimate for the electronic-coupling strength (H_{AB}) (Equation 2.1).

Equation 2.1. $$H_{AB} = 2.05 \times 10^{-2} \left[\frac{\varepsilon_{max} \Delta\bar{\nu}_{1/2}}{\bar{\nu}_{max}} \right] \frac{\bar{\nu}_{max}}{r}$$

The crystal structure of the mixed-valence dimer provides a value for the metal-metal distance r = 5.11 Å (Figure 2.2). The maximum extinction coefficient (ε_{max}) and width ($\Delta\bar{\nu}_{1/2}$) of the MMCT absorption band suggests that the electronic-coupling strength (H_{AB}) is 2000 cm^{-1}. This large value of H_{AB} indicates that $Ru^{II} \rightarrow Ru^{III}$ ET reactions will be adiabatic.

MLCT ($Ru^{II} \rightarrow$ imine) excitation of $[(bpy)(tpy)Ru^{II}(CN)Ru^{III}(NH_3)_5]^{4+}$ and $[(bpy)(tpy)Ru^{II}(CN)Ru^{II}(NH_3)_5]^{3+}$ can initiate intramolecular electron-transfer reactions (Figure 2.8). Two of these reactions formally involve $Ru^{II} \rightarrow Ru^{III}$ ET processes (**2**, **3**) and two can be described as $tpy^{\bullet -} \rightarrow Ru^{III}$ reactions (**1**, **4**). No transient absorption could be detected following picosecond excitation of $[(bpy)(tpy)Ru^{II}(CN)Ru^{III}(NH_3)_5]^{4+}$, suggesting that the rate constants for both reactions **1** and **2** are $>10^{12}$ s^{-1}. Picosecond excitation of $[(bpy)(tpy)Ru^{II}(CN)Ru^{II}(NH_3)_5]^{3+}$ produces a transient difference spectrum (Figure 2.7) reminiscent of that obtained by one-electron reduction of $[(bpy)(tpy)Ru^{II}(CN)Ru^{II}(NH_3)_5]^{3+}$ (Figure 2.6). This transient species is most likely $[(bpy)(tpy^{\bullet -})Ru^{II}(CN)Ru^{III}(NH_3)_5]^{3+}$. From this assignment we infer that reaction **3** proceeds with a rate constant > 10^{12} s^{-1} and that the rate constant for reaction **4** is 3.8 × 10^{10} s^{-1}.

We have used a model developed by Jortner and coworkers to analyze the ET reactions of these strongly coupled Ru dimers [19a-19c]. A single-mode representation of

Figure 2.7 Energy diagrams of plausible mechanisms for ET.

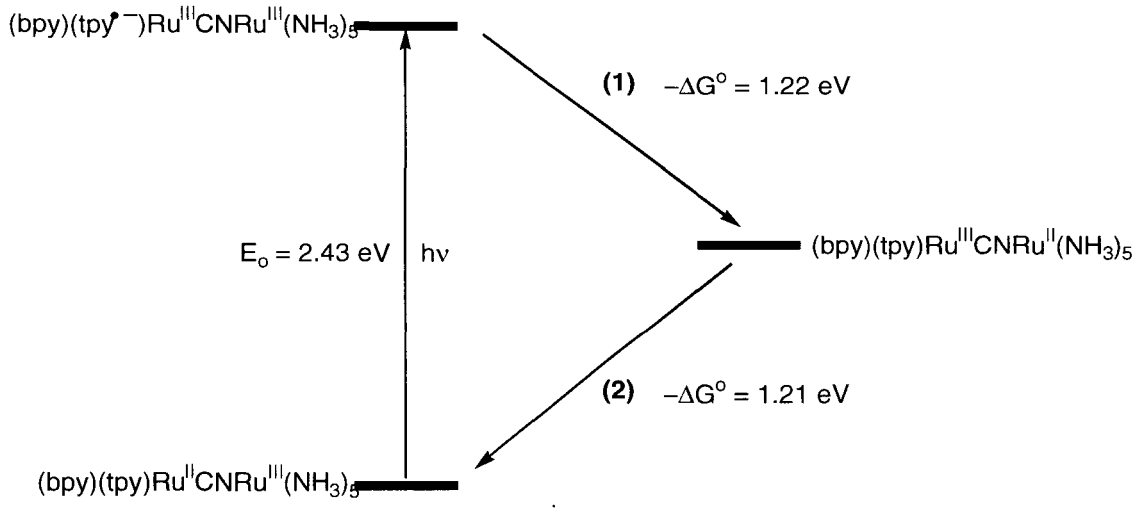
(bpy)(tpy•⁻)Ru^III CNRu^III (NH3)5
(1) −ΔG° = 1.22 eV
E0 = 2.43 eV
hν
(bpy)(tpy)Ru^III CNRu^II (NH3)5
(2) −ΔG° = 1.21 eV
(bpy)(tpy)Ru^II CNRu^III (NH3)5

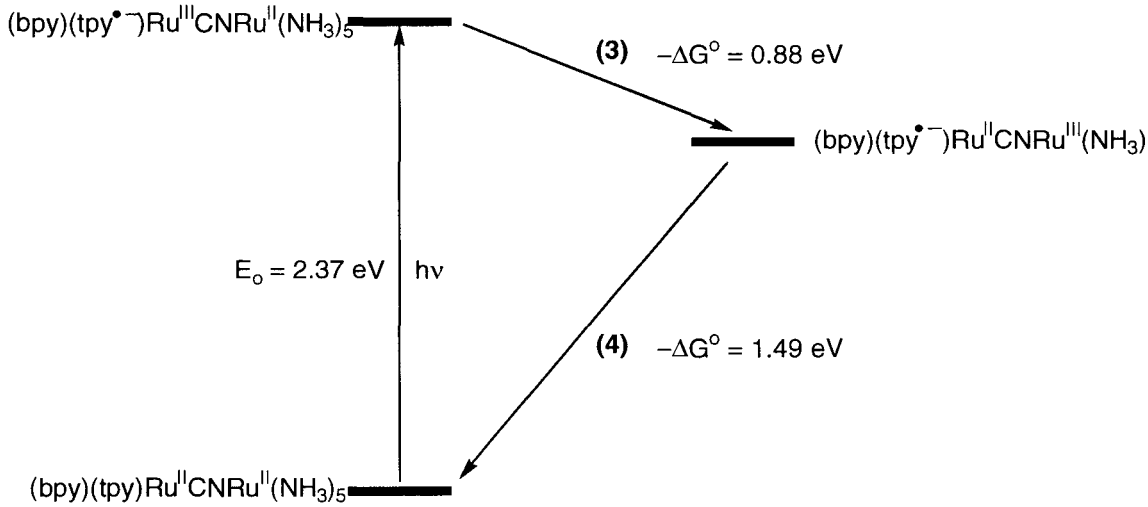
(bpy)(tpy•⁻)Ru^III CNRu^II (NH3)5
(3) −ΔG° = 0.88 eV
(bpy)(tpy•⁻)Ru^II CNRu^III (NH3)
E0 = 2.37 eV
hν
(4) −ΔG° = 1.49 eV
(bpy)(tpy)Ru^II CNRu^II (NH3)5

this model is given by Equation 2.2, where k_{NA}^{0n} is the nonadiabatic rate constant for ET from the ground vibrational state of the reactants to a final (see also Chapter 1, page 27).

Equation 2.2 $$k_{ET} = \frac{k_{NA}^{0n}}{(1 + \mathcal{H}_A^{0n})}$$

state of the products with vibrational quantum number n, and $\mathcal{H}_A^{0n}$ is an adiabaticity parameter for the same transition [19b]. It is important to note that $\mathcal{H}_A^{0n}$ depends upon the longitudinal solvent relaxation time (τ_L = 0.4 ps for CH_3CN) [20] and determines when ET reaction dynamics will be controlled by solvent reorientation.

The simplest application of this model ignores quantum modes and treats all nuclear reorganization classically. For the $Ru^{II} \rightarrow Ru^{III}$ ET reactions (**2**, **3**), we can use the coupling and reorganization parameters extracted from the MMCT analysis. The driving forces for reactions **2** and **3** can be estimated from the electrochemical measurements on the cyanide-bridged dimer (**2**, $-\Delta G = 1.21$; **3**, $-\Delta G = 0.88$ eV). Both reactions are deep in the inverted region ($-\Delta G > \lambda$) and the predicted rate constants (**2**, 2.0×10^8 s^{-1}; **3**, 1.4×10^{11} s^{-1}, Table 2.3) are well below the solvent-controlled limit.

The greater electron-transfer distance in the $tpy^{\bullet-} \rightarrow Ru^{III}$ reactions is likely to produce couplings and reorganization energies different from those associated with $Ru^{II} \rightarrow Ru^{III}$ ET. Furthermore, the involvement of $tpy^{\bullet-}$ radical states should increase λ_i owing to the distortions of the tpy rings upon reduction. The additional inner-sphere reorganization will be similar to that associated with MLCT excited-state formation in $[Ru(bpy)_3]^{2+}$ (0.17 eV) [21]. The solvent reorganization energy also increases due to the increased transfer distance [22]. The irregular shape of the

$[(bpy)(tpy)Ru(CN)Ru(NH_3)_5]^{3+,4+}$ cavity makes this quantity difficult to calculate using dielectric continuum models, but an increase of 0.2 eV in λ_S is reasonable for these reactions, giving a total value of $\lambda \sim 0.89$ eV. Evaluation of Equation 2.1, where quantum modes are neglected, leads to predicted rate constants of (**1**) 6.2×10^{11} and (**4**) 3.9×10^{10} s^{-1} (Table 2.3). Of the four calculated rate constants, only that for reaction **4** agrees with the experimental value and, given the poor agreement for the three other reactions, this is most likely a fortuitous result.

Clearly, the classical treatment of nuclear reorganization does not adequately account for the observed ET rates. Far greater inverted effects are predicted than are found experimentally; similar problems were encountered in the investigations of intramolecular ET in $(H_3N)_5M^{III}(NC)Ru^{II}(CN)_5^-$ (M = Fe, Ru) [8-11]. Explicit account of quantum-mechanical nuclear motions is necessary to explain these data. Quantum-mechanical models require knowledge of the distorting modes that accompany the ET reactions. For $Ru^{III/II}$-ammine reactions, the 0.08 eV inner-sphere distortion [19] primarily involves the Ru-N stretching coordinate which is associated with a ~480 cm^{-1} vibration [8]. Inner-sphere distortions in $Ru^{III/II}$-imine ET reactions are relatively minor and will be neglected [19]. Nuclear reorganization comparable to that estimated for $Ru(bpy)_3^{2+}$ excited-state formation (1350 cm^{-1}, $\lambda_i = 0.17$ eV) [21] will be assumed for reactions involving $tpy^{\bullet-} \rightarrow Ru^{III}$ ET. Finally, distortions in the bridging cyanide ligand might accompany both $Ru^{II} \rightarrow Ru^{III}$ and $tpy^- \rightarrow Ru^{III}$ ET reactions [10,11].

As in the classical treatment, the total reorganization energy and electronic coupling parameters extracted from the analysis of the MMCT absorption profile should provide reliable estimates for predicting the rate of reaction **2**. The inclusion of inner-

sphere reorganization about the Ru-ammine center increases the calculated rate constant by a factor 425 over the classical prediction (Table 2.3), but the calculated value (8.5×10^{10} s^{-1}) is still too small to account for the absence of a detectable transient in $[(bpy)(tpy)Ru^{II}(CN)Ru^{III}(NH_3)_5]^{4+}$. A small distortion in a high frequency mode (*e.g.*, the CN stretching mode, 2050 cm^{-1}, λ_i = 0.025 eV), however, is sufficient to explain the extremely rapid charge-recombination reaction (Table 2.3). Use of the same reorganization and coupling parameters correctly predicts an extremely fast $Ru^{II} \rightarrow Ru^{III}$ ET rate for reaction **3** ($k_{calc} = 1.0 \times 10^{13}$ s^{-1}, Table 2.3).

One of the two $tpy^{\bullet-} \rightarrow Ru^{III}$ ET reactions was too fast to measure (**1**), while the other (**4**) had a rate constant of 3.8×10^{10} s^{-1}. Using inner-sphere distortions for $tpy^{0/\bullet-}$ (λ_i = 0.17 eV) and $Ru^{III/II}$ (λ_i = 0.08 eV), and H_{AB} = 2000 cm^{-1} in the semiclassical expression (Equation 1.11), we predict rate constants of 2.4×10^{13} s^{-1} (**1**) and 1.4×10^{13} s^{-1} (**4**). No reasonable manipulations of the reorganization parameter can rationalize the relatively slow rate observed for reaction **4**. Admittedly, the classical model correctly predicts the rate of reaction **4**, but it is unlikely that nuclear tunneling would be important in reactions **1-3** and not in reaction **4**. Unusually weak electronic coupling can be invoked to explain the slow rate constant for reaction **4**. A coupling strength of H_{AB} = 50 cm^{-1} leads to a good prediction for the reaction **4** rate constant (Table 2.3). The other $tpy^{\bullet-} \rightarrow Ru^{III}$ reaction (**1**), however, requires somewhat greater coupling ($H_{AB} > 160$ cm^{-1}), though it need not be as large as that estimated for $Ru^{II} \rightarrow Ru^{III}$ ET. It is possible that the intervening Ru^{III}-imine center in reaction **1** mediates the coupling between $tpy^{\bullet-}$ and the Ru^{III}-ammine center more effectively than the Ru^{II}-imine center in reaction **4**.

Table 2.3 Comparison of calculated *vs.* experimental rate constants for reactions **1-4**. Rate constants for reactions **1-4** were calculated using the theoretical model described by Equation 2.2.

S_1	$\hbar\omega_1$, eV	S_2	$\hbar\omega_2$, eV	λ_S, eV	H_{AB}, cm^{-1}	k_{calc}, s^{-1}
1, $-\Delta G° = 1.22$ eV						
				0.89	2000	6.2×10^{11}
1.33	0.06	1.00	0.17	0.64	2000	2.4×10^{13}
1.33	0.06	1.00	0.17	0.64	160	2.0×10^{12}
1.33	0.06	1.00	0.17	0.64	50	2.2×10^{11}
2, $-\Delta G° = 1.21$ eV						
				0.52	2000	2.0×10^{8}
1.33	0.06			0.44	2000	8.5×10^{10}
1.33	0.06	0.10	0.25	0.42	2000	2.2×10^{12}
3, $-\Delta G° = 0.88$ eV						
				0.52	2000	1.4×10^{11}
1.33	0.06			0.44	2000	3.4×10^{12}
1.33	0.06	0.10	0.25	0.42	2000	1.0×10^{13}
4, $-\Delta G° = 1.49$ eV						
				0.89	2000	3.9×10^{10}
1.33	0.06	1.00	0.17	0.64	2000	1.4×10^{13}
1.33	0.06	1.00	0.17	0.64	160	4.1×10^{11}
1.33	0.06	1.00	0.17	0.64	50	4.5×10^{10}

[a] S_n is the distortion parameter for the vibrational mode of frequency $\hbar\omega_n$ and $\lambda_{i,n} = S_n\hbar\omega_n$

The time-resolved spectroscopic measurements of ET in the $[(bpy)(tpy)Ru^{II}(CN)Ru^{III}(NH_3)_5]^{4+}$ and $[(bpy)(tpy)^{II}Ru(CN)Ru^{II}(NH_3)_5]^{3+}$ complexes demonstrate that the rates cannot be explained with models that describe nuclear motions classically. Quantum-mechanical refinements to the ET theory improve the agreement between calculated and observed rates. These analyses suggest that high-frequency vibrations of the bridging CN ligand and the imine ligands are involved in nuclear-tunneling processes that enhance the rates of these highly inverted ET reactions.

Conclusions

The complete classical description of the nuclear coordinates is not adequate to explain the ET rates observed in the strongly coupled dinuclear ruthenium complexes studied within. Nuclear tunneling facilitated by a highly inverted energetic landscape compounded with the presence of high frequency vibrational modes must be considered to explain the experimental data.

Photogeneration of the MLCT excited states of $[(bpy)(tpy)Ru^{II}(CN)Ru^{III}(NH_3)_5]^{4+}$ and $[(bpy)(tpy)^{II}Ru(CN)Ru^{II}(NH_3)_5]^{3+}$ results in four distinct electron-transfer events. Only the ET rate of reaction **4** could be measured, while the other reactions proceeded $>10^{12}$ s^{-1}. Weaker coupling between the $tpy^{\bullet-}$ donor and the Ru-ammine acceptor moieties in **4** can account for the slower rate.

References

[1] C Creutz, *Prog. Inorg. Chem.*, **30**, 1-73 (1983).

[2] NS Hush, *Electrochim. Acta*, **13**, 1005-1023 (1968).

[3] RS Mulliken, WB Person, *Molecular Complexes*; Wiley: New York (1969).

[4] RS Mulliken, *J. Am. Chem. Soc.*, **74**, 811-824 (1952).

[5] CA Stein, NA Lewis, GA Seitz *J. Am. Chem. Soc.*, **104**, 2596 (1982).

[6] CA Stein, HJ Taube, *J. Am. Chem. Soc.*, **103**, 615 (1981).

[7] C Creutz, T Matsubara, TL Netzel, N Sutin, *J. Am. Chem. Soc.*, **101**, 5442-5444 (1979).

[8] GC Walker, PF Barbara, SK Doorn, Y Dong, JT Hupp, *J. Phys. Chem.*, **95**, 5712-5715 (1991).

[9] DA Kliner, K Tominaga, GC Walker, PF Barbara,*J. Am. Chem. Soc.*, **114**, 8323-8325 (1992).

[10] K Tominaga, DA Kliner, AE Johnson, NE Levinger, PF Barbara, *J. Chem. Phys.*, **98**, 1228-1243 (1992).

[11a] SK Doorn, RB Dyer, PO Stoutland, WH Woodruff, *J. Am. Chem. Soc.*, **115**, 6398-6405 (1993).

[11b] SK Doorn, PO Stoutland, RB Dyer, WH Woodruff, *J. Am. Chem. Soc.*, **114**, 3133 (1992).

[12] P Belser, A von Zelewsky, A Juris, F Barigelletti, V Balzani, *Gazz. Chim. Ital.*, **115**, 723 (1985).

[13] AB Altabef, SB DeGallo, ME Folquer, NE Katz, *Trans. Met. Chem.*, **18**, 319 (1993).

[14] JV Caspar, TJ Meyer, *J. Am. Chem. Soc.*, **105**, 5583-5590 (1983).

[15] RR Gagne, CA Koval, GC Lisensky, *Inorg. Chem.*, **19**, 2855 (1980).

[16] PC Ford, *Coord. Chem. Rev.*, **5**, 75-99 (1970).

[17] N Sutin, C Creutz, *Inroganic and Organometallic Photochemistry*; N Sutin, C Creutz, Ed.; American Chemical Society: Washington, D.C. (1978).

[18] DF Blair, J Gelles, SI Chan, *Biophys. J.*, **50**, 713 (1986).

[19] GM Brown, N Sutin, *J. Am. Chem. Soc.*, **101**, 883-892 (1979).

[19a] M Bixon, J Jortner, *Chem. Phys.*, **176**, 467-481 (1993).

[19b] J Jortner, M Bixon, *J. Chem. Phys.*, **88**, 167-170 (1988).

[19c] I Rips, J Jortner, *J. Chem. Phys.*, **87**, 2090-2104 (1987).

[20] M Kahlow, W Jarzeba, T Kang, PF Barbara, *J. Chem. Phys.*, **90**, 151-158 (1989).

[21] N Sutin, BS Brunschwig, C Creutz, JR Winkler, *Pure Appl. Chem.*, **60**, 1817-1829 (1988).

[22] B Brunschwig, S Ehrenson, N Sutin, *J. Am. Chem. Soc.*, **106**, 6858-6859 (1984).

[23] RS Farid, IJ Chang, JR Winkler, HB Gray,*J. Phys. Chem.*, **98**, 5176-5179 (1994).

[24] RR Alfano, In *The Supercontinuum Laser Source*, RR Alfano Ed., Springer-Verlag, New York (1989).

Chapter 3

Electron Tunneling in Ruthenium-Modified High-Potential Iron Sulfur Proteins

Abstract

Rates of $[Fe_4S_4]^{2+} \rightarrow Ru^{3+}$ electron transfer (ET) in Ru-modified derivatives of *Chromatium vinosum* High-Potential Iron-Sulfur Protein were measured. Surface histidines introduced by site-directed mutagenesis at positions 18, 50, and 81 (native His42 was replaced by a glutamine) were modified by coordination of $[Ru(bpy)_2(im)]^{2+}$ (bpy = 2,2'-bipyridine, im = imidazole). The rates of ET in the His81 and His50 derivatives vary by a factor greater than 300, despite a difference in distance between the donor and acceptor of < 0.5 Å. PATHWAY and reorganization energy computations provide an explanation consistent with the experimental rate differences. The weak electronic coupling, due to a through space jump, in the pathway linking the donor to acceptor of the His 50 derivative accounts for the dramatic rate difference.

Introduction

High potential iron-sulfur proteins (HiPIPs) are found in photosynthetic purple nonsulfur bacteria [1]. The three-dimensional structure of *Chromatium vinosum* HiPIP (85 aminoacids) [2,3] features two short segments of α-helix, three strands of antiparallel β-pleated sheet, and a small helix near the N-terminus (Figure 3.1). The cubane $[Fe_4S_4]$ cluster occupies an inner protein cavity made up from residues 43 to 80, and is attached covalently to the polypeptide matrix through Fe-S bonds to cysteines 43, 46, 63, and 77. The side chains of Tyr19, Phe48, Phe66, Trp60, Trp76, Trp80, and other nonpolar residues encapsulate the cluster in a hydrophobic cavity that is inaccessible to solvent [4,5].

In order to study intramolecular electron transfer (ET) in HiPIP, $[Ru(bpy)_2(im)]^{2+}$ was bound to a surface histidine to serve as a fixed redox partner for the iron-sulfur active site. Four HiPIPs, the *wild-type* and three mutants, were ruthenium modified. The *wild-type* HiPIP contains one natural histidine at position 42. Site-directed mutagenisis generated the three mutant HiPIPs, which contain one histidine each at positions 18, 50, 81, respectively (His42 was replaced with Gln).

Photoexcitation of the $[Ru(bpy)_2(im)HisX]^{2+}$ chromophore initiated ET reactions by generating a strongly reducing MLCT excited state. The rates of photoinduced forward ET and subsequent thermal back ET were monitored by transient absorption spectroscopy (Figure 3.2). The results of the thermal back ET were compared to PATHWAY calculations, which are based on superexchange models [7-12].

The ET rates presented in this chapter are significant in two respects. First, the ET rates for the His81 mutant is more than 300 times greater than that of His50, although the closest Fe-Ru distances are nearly identical (R = 12 Å ± 0.5 Å). Calculations based on superexchange models are consistent with this observation. This result signifies the importance of the structural details in the protein matrix to the effectiveness in mediating ET. Second, the ET rates represent the fastest rates measured in ruthenium-modified proteins. These rates extend the data available for the 'master' rate *vs.* distance plot (Figure 3.15) (master because the plot incorporates data from various protein ET studies) by one order of magnitude. Moreover, the series of fast ET kinetics show that rates are not limited or gated by protein dynamics.

Figure 3.1 Structural model of Ru-modified HiPIPs. The iron-sulfur cluster and the $[Ru(bpy)_2(im)]^{2+}$ group attached to His42 are highlighted along with the side chains of histidines 18, 50, and 81. The position of the $[Ru(bpy)_2(im)]^{2+}$ complex for each mutant was modeled with XFIT [6b] to maintain proper stereochemistry and avoid close contacts with the protein. Stereochemical and van der Waals constraints place an upper error of about 1 Å on the distance separating the metal centers. The X-ray coordinates for $[Ru(bpy)_2(im)_2]SO_4 \cdot 10H_2O$ [6c] and the X-ray coordinates for (His42Gln)HiPIP (PDB code 1B0Y) were used for modeling. The closest Ru to Fe distances are: 14 Å (His18); 12 Å (His50); 12 Å (His42); 12 (His81).

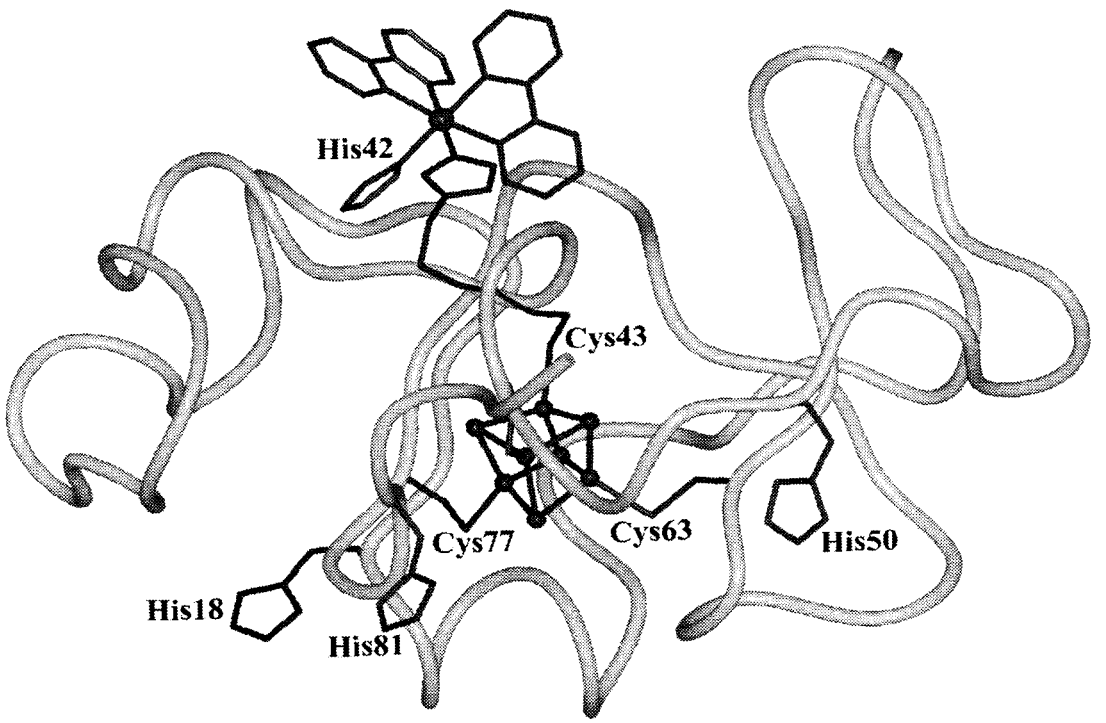
His42
Cys43
Cys77
Cys63
His50
His18
His81

Figure 3.2 Energy diagram of photoinduced forward and thermal back ET.

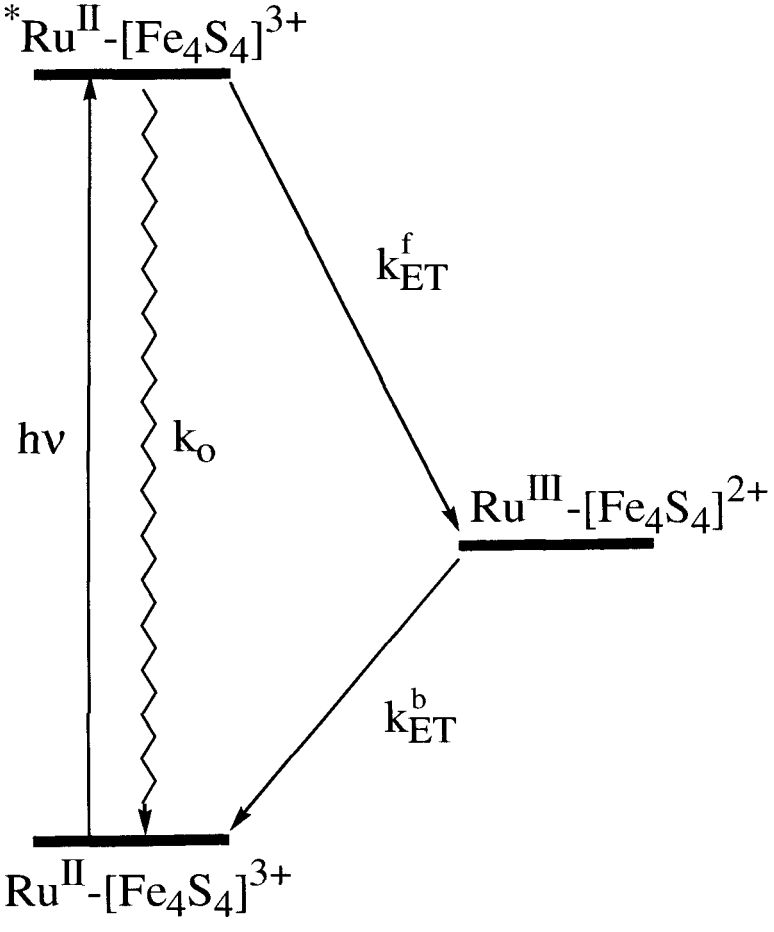
*Ru^II-[Fe4S4]^3+
k_ET^f
hν
k_o
Ru^III-[Fe4S4]^2+
k_ET^b
Ru^II-[Fe4S4]^3+

Background

Intermolecular ET from one biological molecule to another is the fundamental reaction for energy conversion in the processes of respiration and photosynthesis [6]. Many biomolecules in these processes are proteins that contain redox sites buried within the protein matrix. The protein matrix prevents buried active sites from direct collision, and forces electron tunneling to occur over large distances. This leads to weakly-coupled ET reactions, which are frequently described by semiclassical ET theory [7] (Chapter 1, Equation 1.7). Contemporary models for ET in proteins assume that the protein matrix mediates electron tunneling [8-12]. In these models, the 3-dimensional protein structure provides specific pathways for electron tunneling, and the structural details of these pathways govern the efficiency by which ET is mediated by the protein matrix. The necessity to understand these and other factors that control the rates of ET in biological systems has stimulated the study of electron tunneling between redox centers in protein molecules [13,14].

Progress in protein ET has been expedited by achievements in areas such as metalloprotein isolation and purification, site-directed mutagenesis, high-resolution X-ray and NMR structure determination, and time resolved kinetics [15]. Armed with a multitude of structurally characterized metalloproteins and the ability to measure kinetics over 16 orders of magnitude in time, a great deal of experimental data has been compiled [13,14].

The synthetic flexibility of coordinating redox-active molecules to desired protein surface sites has facilitated systematic investigations of driving-force and distance dependencies. Ruthenium complexes have been most frequently employed due to their

favorable binding and redox properties. Stable ruthenium-modified proteins are obtained by reacting a ruthenium aquo complex with surface histidines [16,17]. Depending on the ligand set around ruthenium, the redox potential can be varied from < 0 – > 1.5 eV [13].

In early studies, $[Ru(NH_3)_5(H_2O)]^{3+}$ complexes were coordinated to surface histidines of Fe- [19-20] and Zn-cytochrome *c* [21-23], myoglobin [24-28], HiPIP [29,30], azurin [31], pastocyanin [32,33], stellacyanin [34,35], cytochrome b_5 [36] and cytochrome c_{551} [37]. Fast photochemical electron injection into Ru^{3+} initiated intramolecular ET from Ru^{2+} to the active site. More recently, $[Ru(bpy)_2(im)(His)]^{2+}$ complexes have been the redox partner of choice due to the additional favorable characteristics of long-lived, luminescent metal-to-ligand charge transfer (MLCT) excited states [38-42]. The MLCT excited state of $[Ru(bpy)_2(im)(His)]^{2+}$ is both a good electron donor and acceptor, and allows for direct electron or hole injection, or indirect flash-quench methods [38]. Furthermore, the reduction potential of these ruthenium imine complexes often result in ET reactions that are nearly activationless, and thus allow more reliable determination of H_{AB} and λ parameters from driving force studies [13].

Electronic Structure of $[Fe_4S_4]^{3+}$ and $[Fe_4S_4]^{2+}$

The ground and excited state properties of iron-sulfur cluster centers are very sensitive to intracluster valence delocalization [57]. One finds trapped valence structures, as in the 2Fe ferredoxin in its reduced state, and partially delocalized electronic stuctures as in 4Fe ferredoxin and HiPIP systems. The valence delocalization description for HiPIP is $2Fe^{3+}$:$2Fe^{2.5+}$. Oxidized HiPIP is paramagnetic (S = 1/2), while the reduced protein is diamagnetic (S = 0) [57]. Analyses of ^{57}Fe-coupling constants for high potential iron-

sulfur protein indicates the S = 7/2 is more appropriate for the formal spin state of the valence-delocalized [Fe_2S_2] fragment, with antiferromagnetic coupling to S = 3 giving a S = 1/2 ground state [58]. MCD measurements yielded the spin-dependent resonance delocalization energy, $\beta \sim 4500\ cm^{-1}$. The exchange-coupling constant of a $Fe_2(\mu_2\text{-}S)_2$ fragment in a cubane-type [Fe_4S_4] cluster is $J = -300\ cm^{-1}$ [15].

Experimental

Protein Mutation

All mutations were performed by Dr. Elena Babini and have been described elsewhere [43,44].

Protein Ruthenium Modification

All Ru-modification reactions were performed by Dr. Angelo Di Bilio (Figure 3.3). Ruthenium-modified HiPIPs were prepared by reacting reduced protein (~ 0.1 mM) dissolved in 250 mM $NaHCO_3$/10 mM HEPES buffer (pH 7.7-8.2) for 3-5 days (at RT) with a 3-5 fold excess of $[Ru(bpy)_2CO_3]\cdot 4H_2O$ (freshly dissolved in the same buffer); in the case of (His18)HiPIP a 1:1 protein-$Ru(bpy)_2CO_3$ ratio was used. The reaction was quenched by gel filtration. Ru(HisX)HiPIP (X = 18, 42, 50, 81) was isolated by means of two chromatographic (FPLC) steps: (a) Affinity chromatography (IMAC) was performed as described before [45]. (b) The material that did not bind to the IMAC column was recovered, equilibrated with 20 mM Tris buffer at pH 8.1 (buffer A), and separated with a HR 5/5 Mono Q column using a salt gradient (20 mM Tris/ 300 mM NaCl pH 8.1). $Ru(bpy)_2(H_2O)$(His)HiPIPs were identified by their absorption spectra. Note, however,

Figure 3.3 Synthetic scheme for ruthenium modification of HiPIPs.

Synthesis of Ru-Modified HiPIP

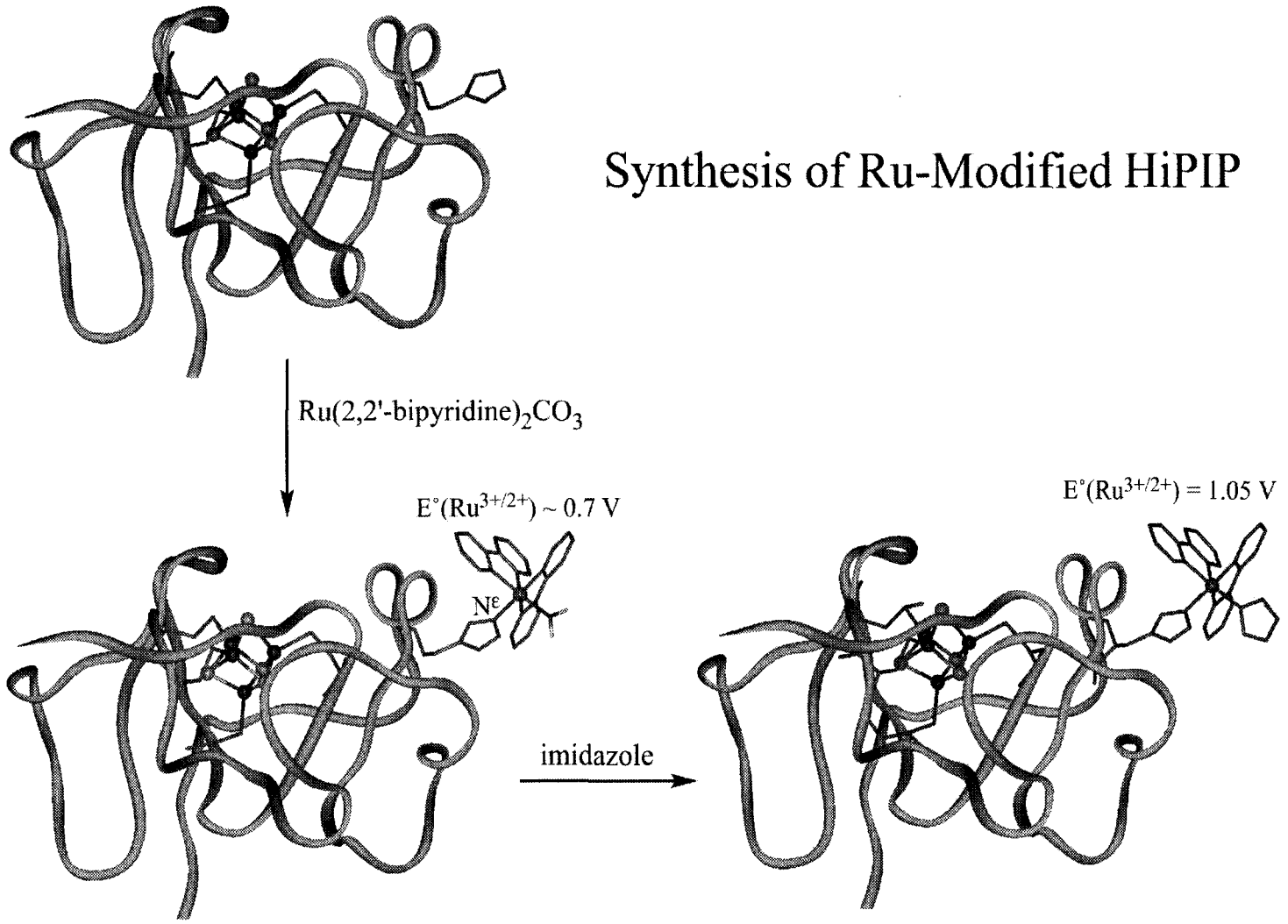

that in most cases a second FPLC run was needed to achieve baseline separation. The yields of protein modified at histidine were moderate (due to ruthenium binding to other amino acids) in all cases, with the exception of (His18)HiPIP, which afforded Ru(bpy)(H_2O)(His18)HiPIP in high yield. Ru(bpy)$_2$(im)(His)HiPIPs were obtained by equilibrating Ru(bpy)$_2$(H_2O)HiPIP[Fe_4S_4]$^{2+}$ with 100 mM im/ 50 mM NaCl (pH 7.0-7.2), and keeping these solutions under argon at RT for 1-2 weeks. Care must be exercised in order to prevent protein denaturation by maintaining the concentration of imidazole $\leq$ 100 mM. Samples were purified by FPLC before use in laser experiments.

Absorption Spectroscopy

Absorption spectra were obtained by Dr. Angelo Di Bilio on an HP diode array spectrophotometer using 1 cm pathlength cuvettes.

Electrochemistry

Electrochemical experiments were performed by Dr. Angelo Di Bilio. Cyclic voltammetry experiments (CV) were performed with a Potentiostat/Galvanostat PAR model 273A. A 1 mm diameter pyrolitic graphite disk (PGE) was used as working electrode and a saturated calomel electrode and a 5 mm diameter Pt electrode were used as reference and counter electrodes, respectively. Reported redox potentials are referenced to the normal hydrogen electrode (NHE). All measurements were carried out under argon using a cell for small volume samples (V = 0.5 ml) under thermostatic control. Scan rates varied from 0.02 to 0.2 V/s. The cleaning procedure of the working electrode is crucial to the voltammetric response. The PGE was first treated with anhydrous ethanol for 10 min, polished with alumina (BDH, particle size of about 0.015

μm) water slurry on cotton wool for 3 min, and finally treated in an ultrasonic pool for about 5 min. Peak separation in CV experiments varied from 60 to 90 mV for scan rates in the range 0.02-0.2 V/s. Anodic and cathodic peak currents were almost identical and both were proportional to protein concentration and $v^{1/2}$ (v = scan rate), indicating a diffusion controlled, reversible (or quasi-reversible) electrochemical processes. Given the reversibility (or quasi-reversibility) of the electrochemical process, the symmetrical shape of the voltammograms and the almost negligible influence of the scan rate on the half-wave potentials, the $E_{1/2}$ values (taken as the average of the cathodic and anodic peak potentials) can be confidently assumed as the E°' values. The temperature dependence of the reduction potential was determined with a "nonisothermal" cell, in which the reference electrode is kept at constant temperature while the temperature of the working electrode is varied. The experiments were performed at least two times and the E°' values were found to be reproducible within ±2 mV.

Transient Absorption Spectroscopy

Sample preparation and nanosecond transient-absorption experiments of the His50 mutant were performed by Dr. Angelo DiBilio. Samples for transient absorption spectroscopy contained oxidized Ru-modified HiPIP in sodium or potassium phosphate buffer at pH 7.0. Oxidation was achieved by reacting the proteins with excess ferricyanide for 3-4 min followed by gel filtration. Samples for laser experiments were under argon. The apparatus for nanosecond transient absorption has been previously described [46]. ET could be monitored at any wavelength in the range 300-600 nm: $\Delta\varepsilon(\text{red-ox})_{\text{HiPIP}} \sim -10{,}800\ \text{mol}^{-1}\text{cm}^{-1}$ (478 nm) [47]; $\Delta\varepsilon(\text{red-ox})_{\text{Ru}} \sim -7{,}000\ \text{mol}^{-1}\text{cm}^{-1}$ (429 nm), and Δε(red-

Figure 3.4 Picosecond Transient Absorption Apparatus. At position 1 is a pulse train of 1 nJ, 1064 nm laser light, in which the pulses are spaced 14 ns apart and have a FWHM of ~100 ps. At position, one pulse of the pulse train is injected and amplified by the regenerative amplifier, yielding 6 mJ, 1064 nm pulses at 10 Hz. After position 2, the pulses undergo temporal compression, which is effected by dual grating pulse compression [48]. Further amplification, just prior to position 3, generates 30 mJ pulses with FWHM of 10 ps.

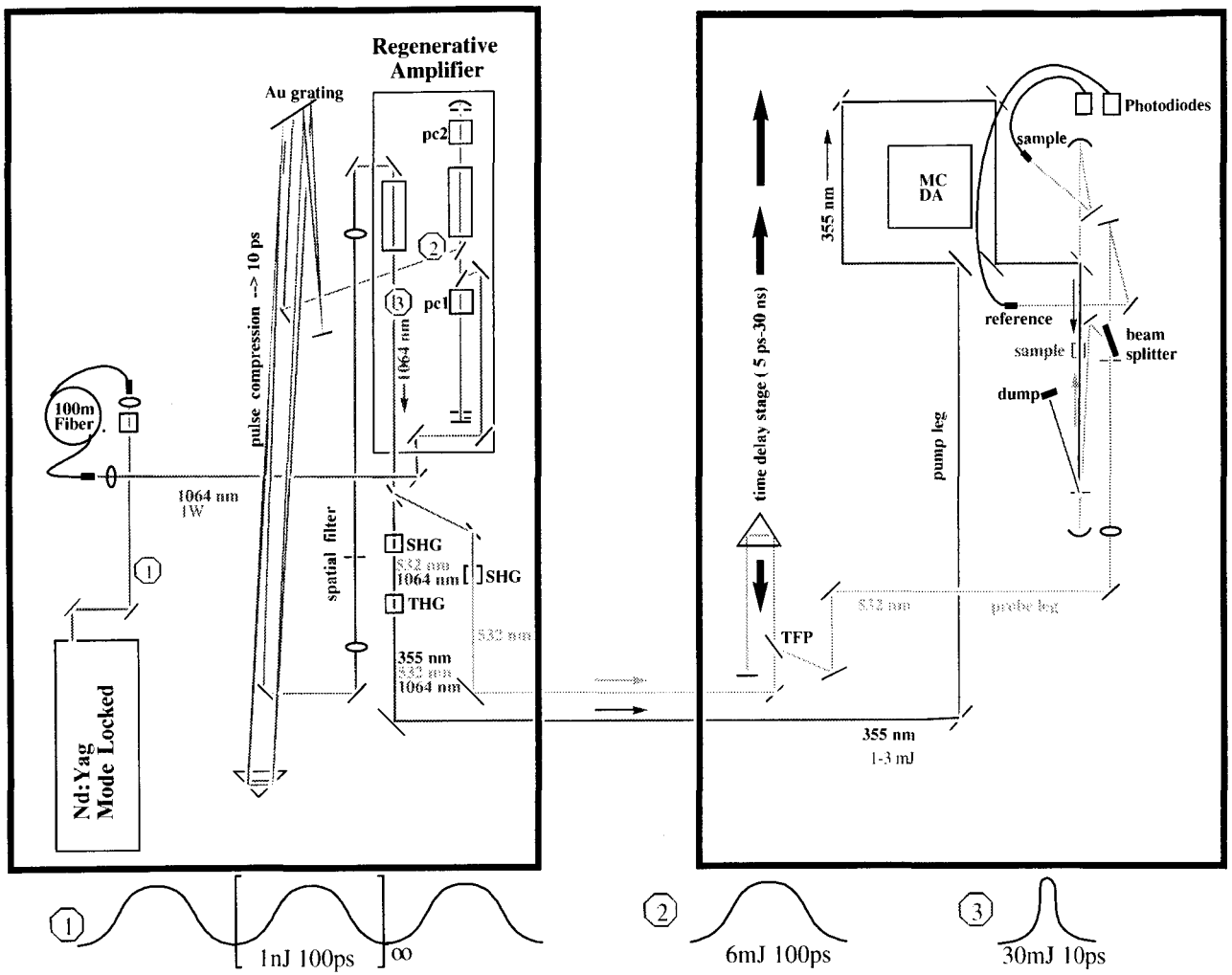
Regenerative Amplifier
Au grating
pc2
pc1
pulse compression ~ 10 ps
1064 nm
100m Fiber
1064 nm 1W
spatial filter
SHG
532 nm
1064 nm
SHG
THG
532 nm
355 nm
532 nm
1064 nm
Nd:Yag Mode Locked
time delay stage (5 ps-30 ns)
355 nm
MC DA
Photodiodes
sample
reference
sample
beam splitter
dump
pump leg
532 nm
probe leg
TFP
355 nm
1-3 mJ
1
1nJ 100ps
∞
2
6mJ 100ps
3
30mJ 10ps

$ox)_{Ru}$ ~17,500 $mol^{-1}cm^{-1}$ (320 nm). Rates greater than ~2 x 10^7 s^{-1} were measured using a picosecond transient absorption spectrometer. Picosecond pulses (10 ps FWHM, 1064 nm) were generated at 10 Hz using chirped pulse amplification and dual grating pulse compression [48] from a mode locked Nd:YAG laser (Coherent) seeding a Nd:YAG regenerative amplifier (Continuum) (Figure 3.4). Excitation (355 nm, 1 mJ) and probe (532 nm, 100 μJ) beams were generated by SHG followed by THG and SHG, respectively. A delay between pump and probe legs was achieved by varying the probe leg distance with respect to the sample leg distance by using a programmable positioning table (Anoride). Light intensity measurements were performed with homebuilt photodiode detector, a sample and hold circuit. The analog signals were converted to digital values with an A/D converter in a personal computer.

Theoretical Analysis

The theoretical analysis was performed in the laboratory of Prof. David Beratan. Pathway analysis of ET in Ru-HiPIP utilized the X-ray structures of HiPIP and Ru model complex [6c]. The Ru complexes were built using HyperChem and partially energy minimized using AMBER 4.1. For structures other than the His 42 derivative, the His at position 42 was changed to Gln and the amino acids at positions 18, 50, or 81 were changed to His.

The standard pathway approximation to the coupling element was used, and is described in detail elsewhere [7-12]:

Equation 3.1

$$H_{AB} = H^{o}_{AB} \prod_{i} \varepsilon_i^{bond} \prod_{j} \varepsilon_j^{H-bond} \prod_{k} \varepsilon_k^{space}$$

Equations 3.2.a-c

$$\varepsilon^{bond} = 0.6$$

$$\varepsilon^{H-bond} = 0.36\exp[-1.7(R-2.8)]$$

$$\varepsilon^{space} = 0.6\exp[-1.7(R-1.4)]$$

Results

The absorption spectrum of $[Ru(bpy)_2(im)_2]^{2+}$, oxidized wt HiPIP, and ruthenium-modified HiPIP are shown in Figure 3.3. The spectrum of the modified protein is a sum of the model complex and unmodified protein, which indicates weak electronic interaction between the redox partners. The absorption spectra of reduced and oxidized HiPIP are shown in Figure 3.4, and the difference spectrum is shown in Figure 3.5. The large difference in optical density at the probe region (532 nm) allowed good signal to noise in the transient absorption experiments. The difference spectrum of the model complex in Ru^{3+} and Ru^{2+} oxidation states is shown in Figure 3.6. At 532 nm the difference in optical density is small. In fact, upon picosecond excitation, the expected instantaneous bleach of the MLCT excited state was undetectable at 532 nm. Figures 3.7-3.12 show the transient-absorption kinetics data for the modified-HiPIPs (His50, 81, 42, and 18). Figure 3.13 shows the kinetics data for His42 on a semilogx plot, which exemplifies that both the rise and the fall of the signal fit well to two exponentials. The rate constants obtained from least squares analysis of the kinetics data are summarized in Table 3.1.

Figure 3.5 Absorption spectra of modified, unmodified oxidized HiPIP, and $[Ru(bpy)_2(im)_2]^{2+}$.

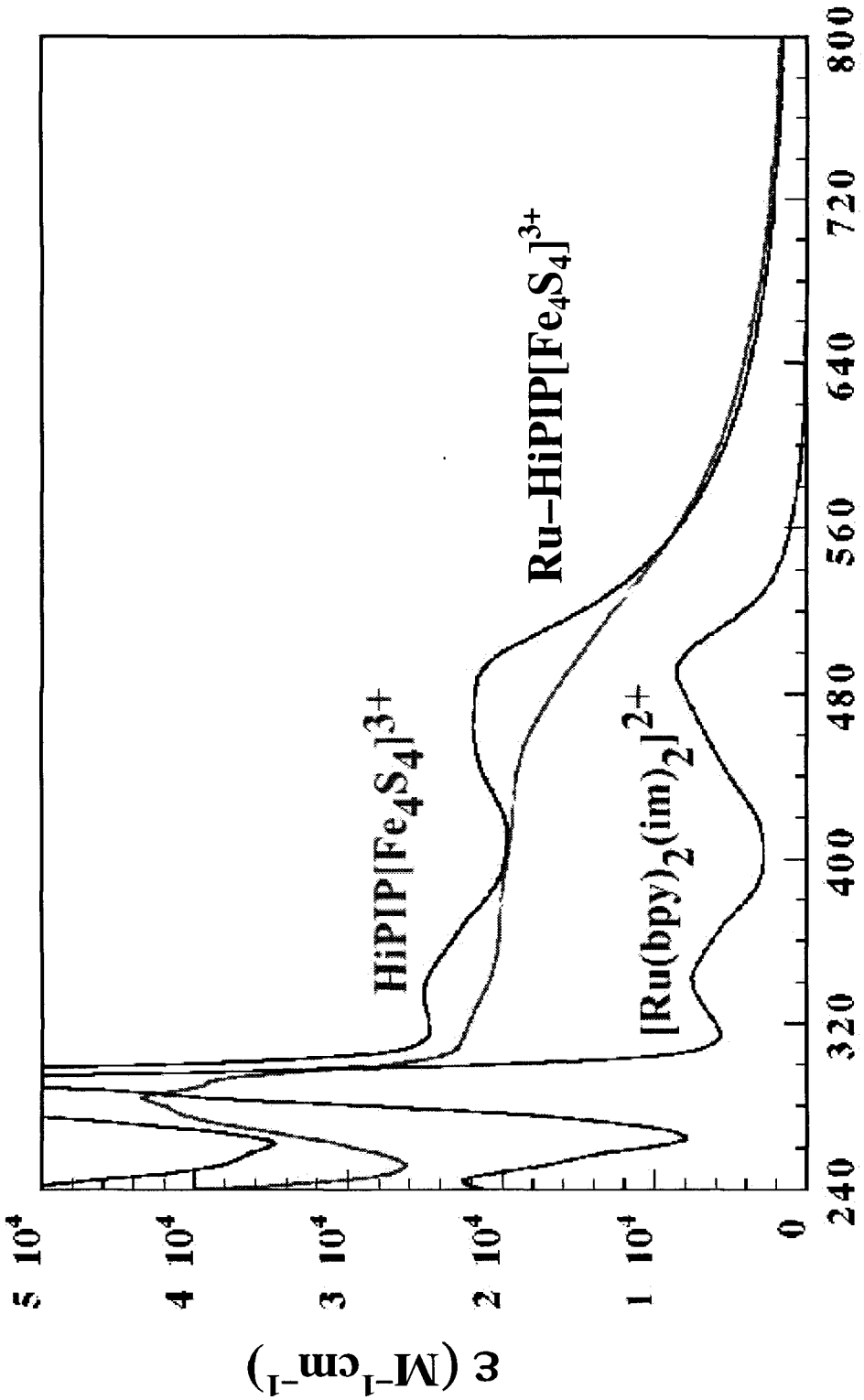
ε (M⁻¹cm⁻¹)
5 10⁴
4 10⁴
3 10⁴
2 10⁴
1 10⁴
0
240
320
400
480
560
640
720
800
Wavelength (nm)
HiPIP[Fe4S4]3+
Ru–HiPIP[Fe4S4]3+
[Ru(bpy)2(im)2]2+

Figure 3.6 Absorption spectra of reduced and oxidized HiPIP.

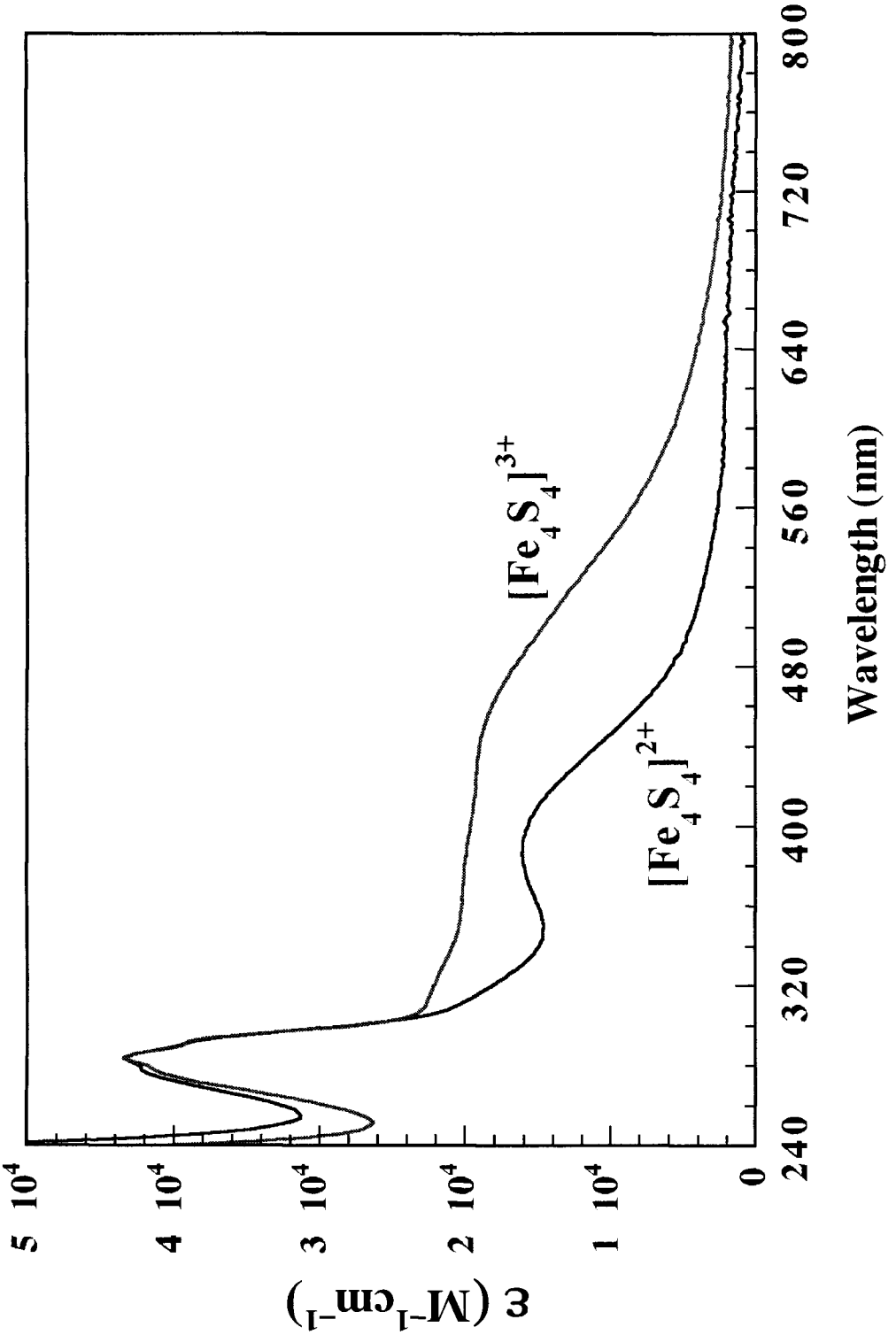
ε (M⁻¹cm⁻¹)
5 10⁴
4 10⁴
3 10⁴
2 10⁴
1 10⁴
0
240
320
400
480
560
640
720
800
Wavelength (nm)
[Fe4S4]3+
[Fe4S4]2+

Figure 3.7 Difference spectrum of reduced and oxidized HiPIP.

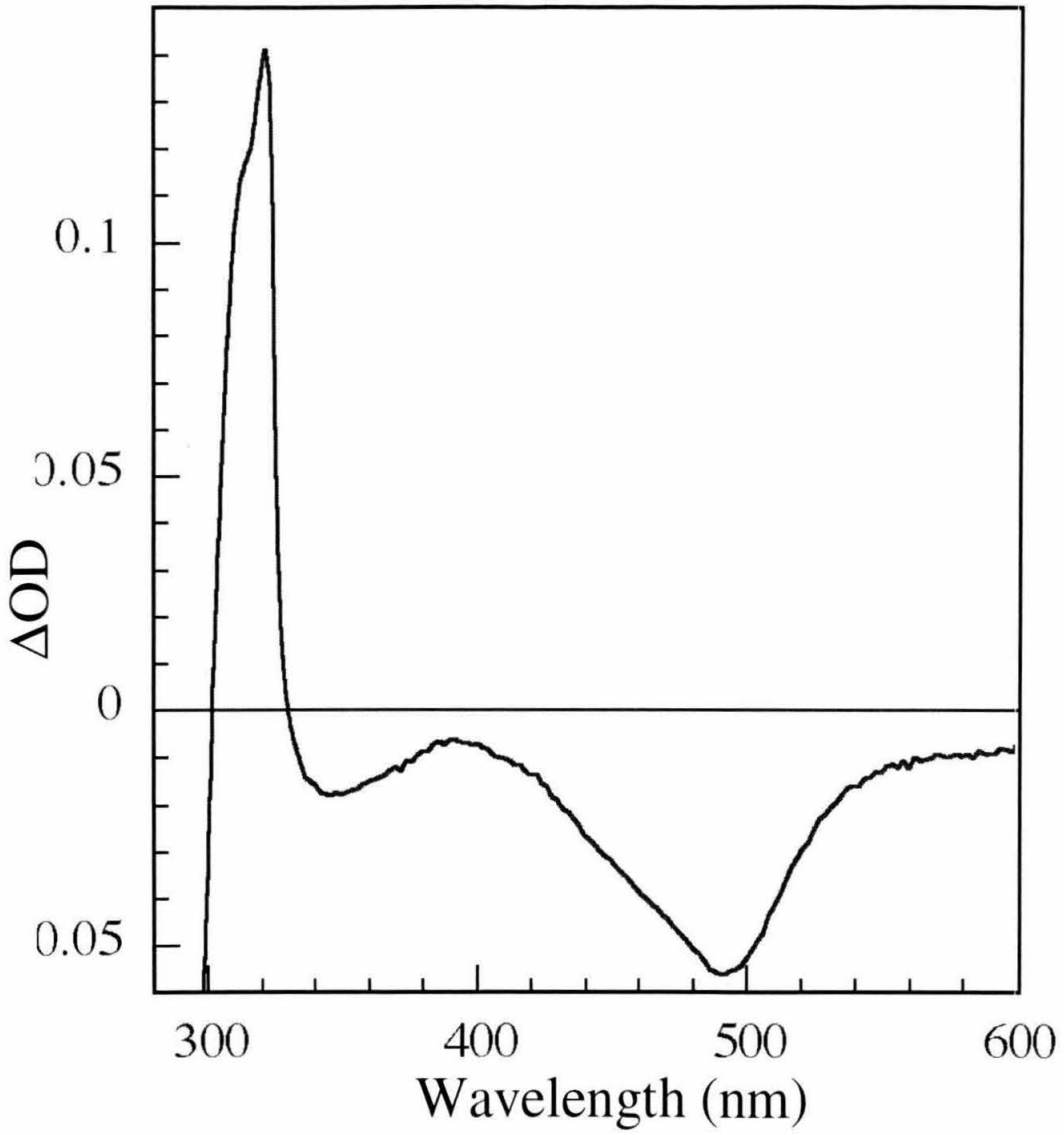
0.1
0.05
0
0.05
ΔOD
300
400
500
600
Wavelength (nm)

Figure 3.8 Difference spectrum of $[Ru(bpy)_2im_2]^{2+/3+}$ model complex.

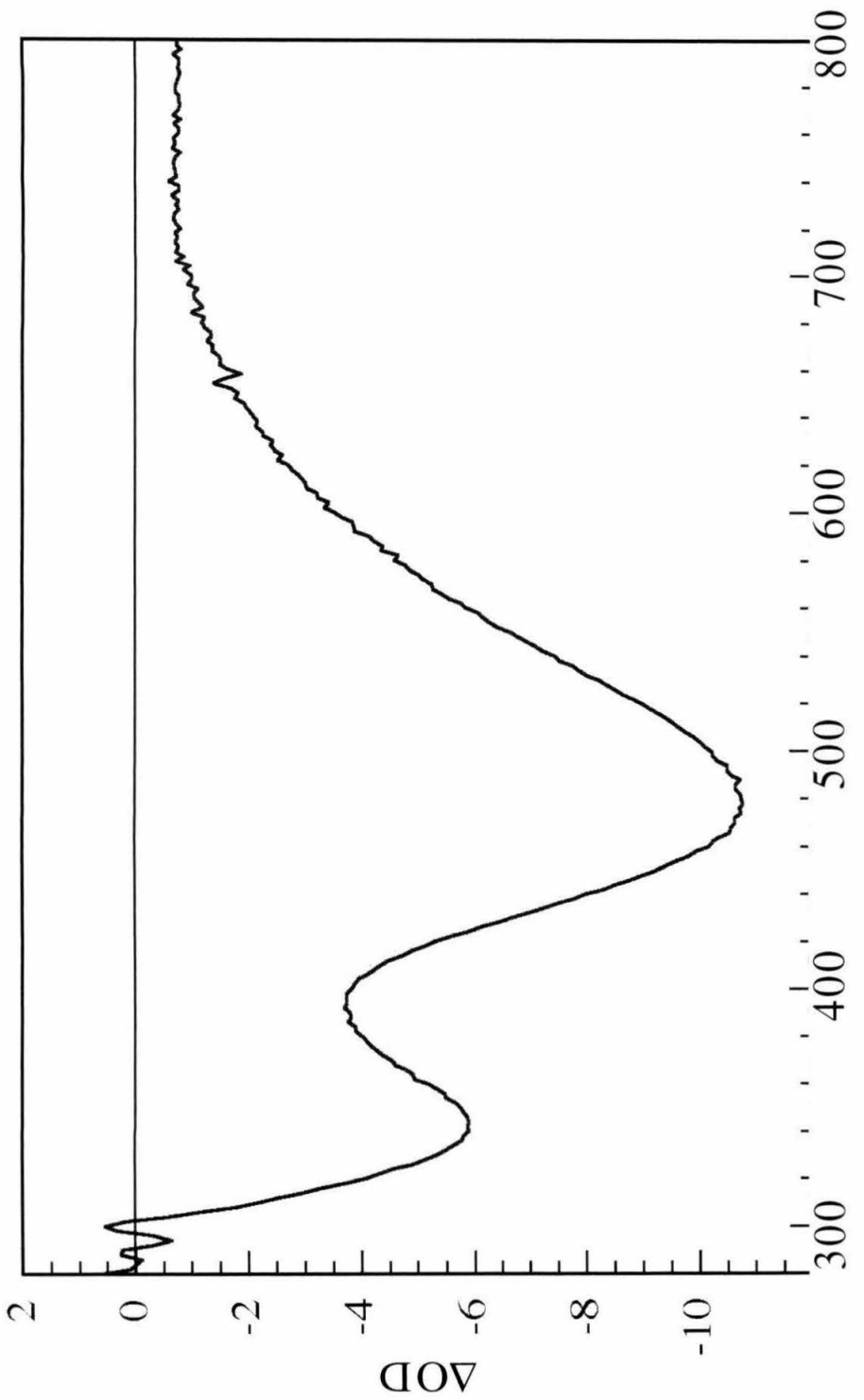
2
0
-2
-4
-6
-8
-10
ΔOD
300
400
500
600
700
800
Wavelength (nm)

Figure 3.9 Transient absorption kinetics of HiPIP-Ru(bpy)$_2$imHis50. The solid line represents the best fit of a singe exponential function.

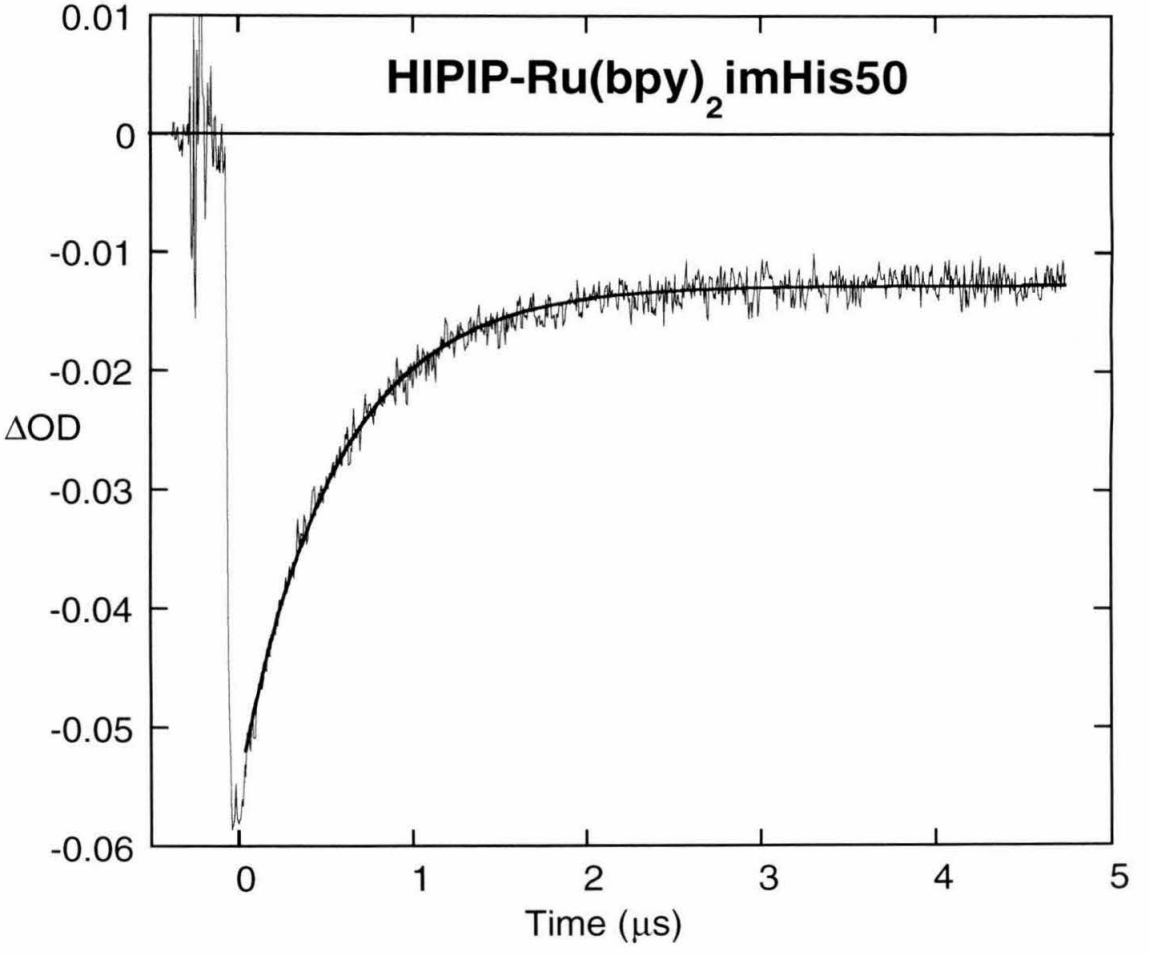
HIPIP-Ru(bpy)2imHis50
0.01
0
-0.01
-0.02
-0.03
-0.04
-0.05
-0.06
ΔOD
0
1
2
3
4
5
Time (μs)

Figure 3.10 Transient absorption kinetics of HiPIP-Ru(bpy)$_2$imHis81. The solid line represents the best fit of a two exponential function that fit the rise and fall of the signal.

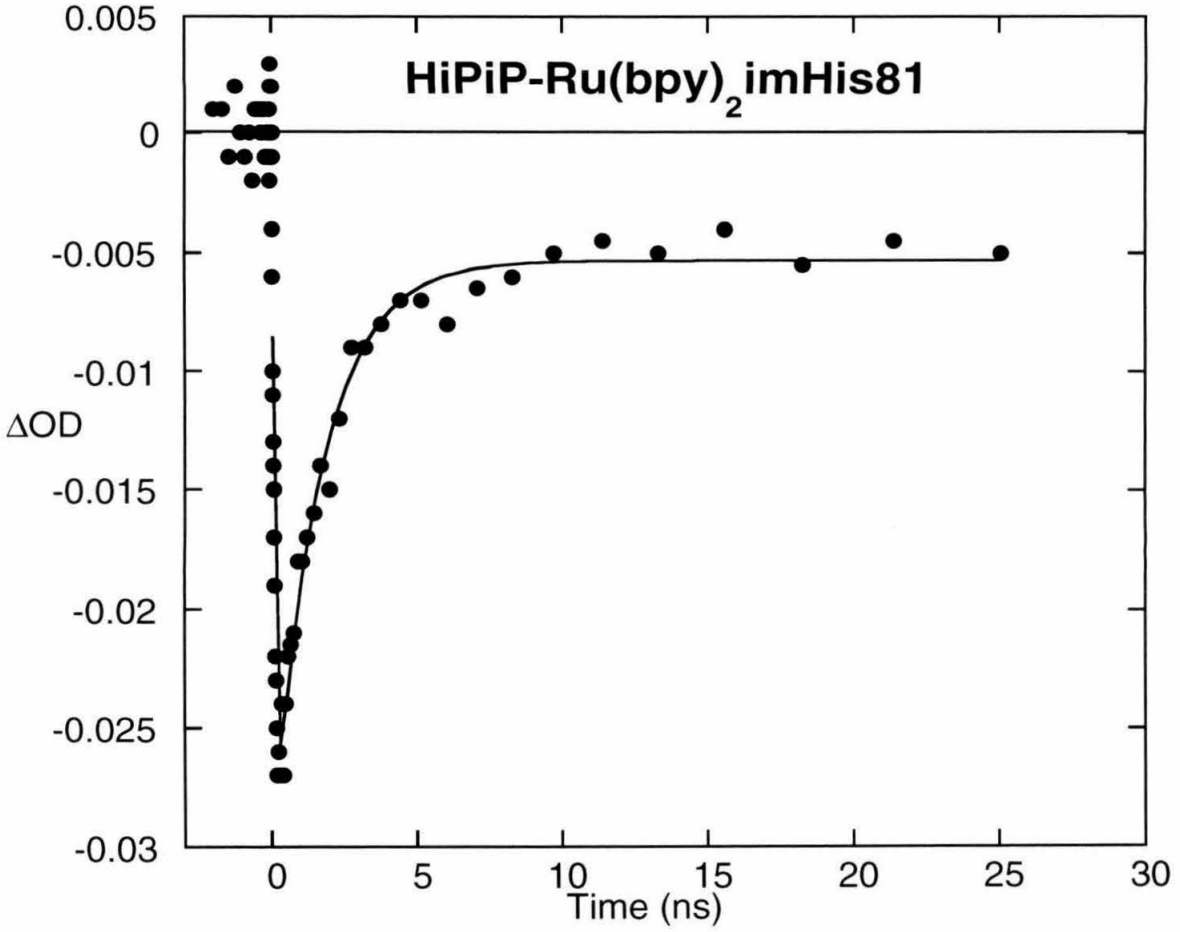
HiPiP-Ru(bpy)2imHis81
0.005
0
-0.005
-0.01
-0.015
-0.02
-0.025
-0.03
ΔOD
0
5
10
15
20
25
30
Time (ns)

Figure 3.11 Transient absorption kinetics of HiPIP-Ru(Me_2bpy)$_2$imHis81. The solid line represents the best fit of a two exponential function that fit the rise and fall of the signal.

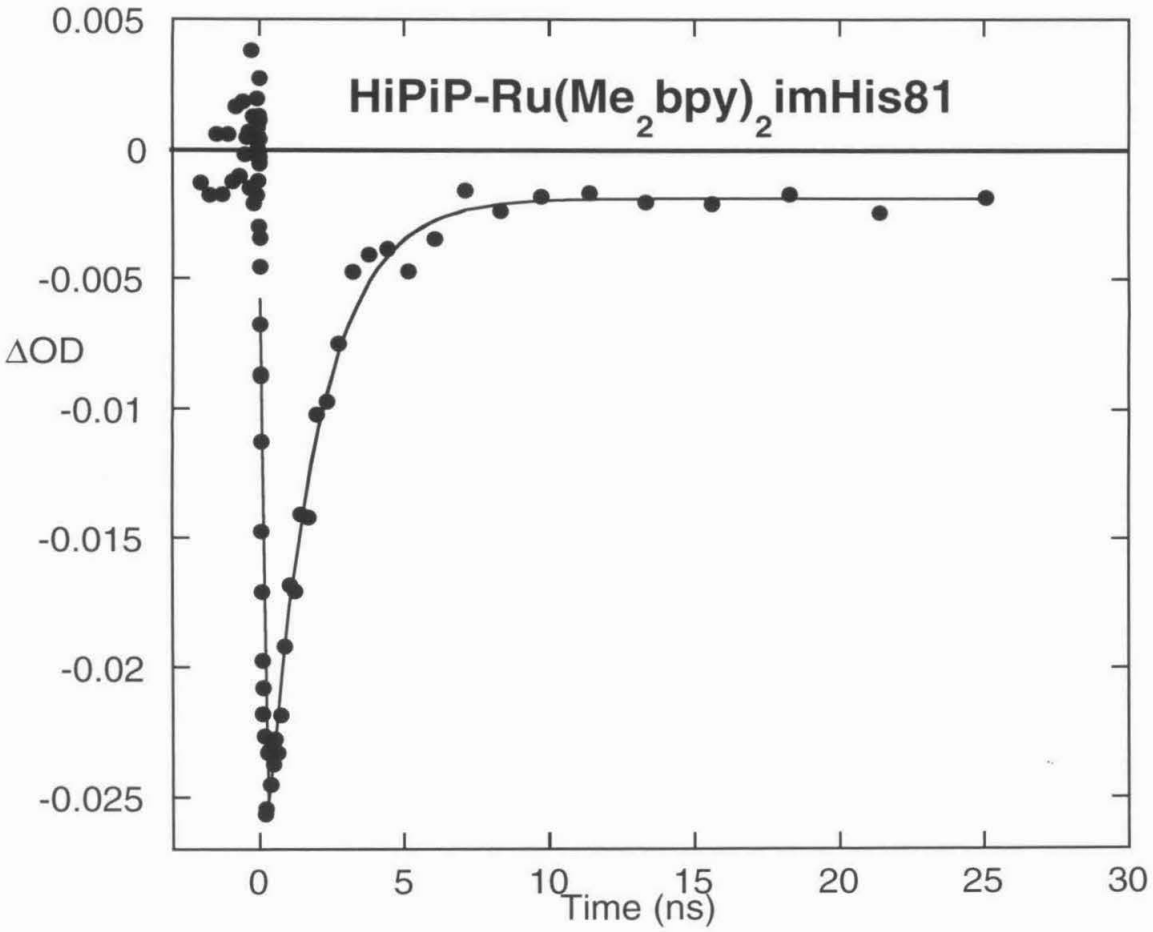
HiPiP-Ru(Me2bpy)2imHis81
0.005
0
-0.005
ΔOD
-0.01
-0.015
-0.02
-0.025
0
5
10
15
20
25
30
Time (ns)

Figure 3.12 Transient absorption kinetics of HiPIP-Ru(bpy)$_2$imHis42. The solid line represents the best fit of a two exponential function that fit the rise and fall of the signal.

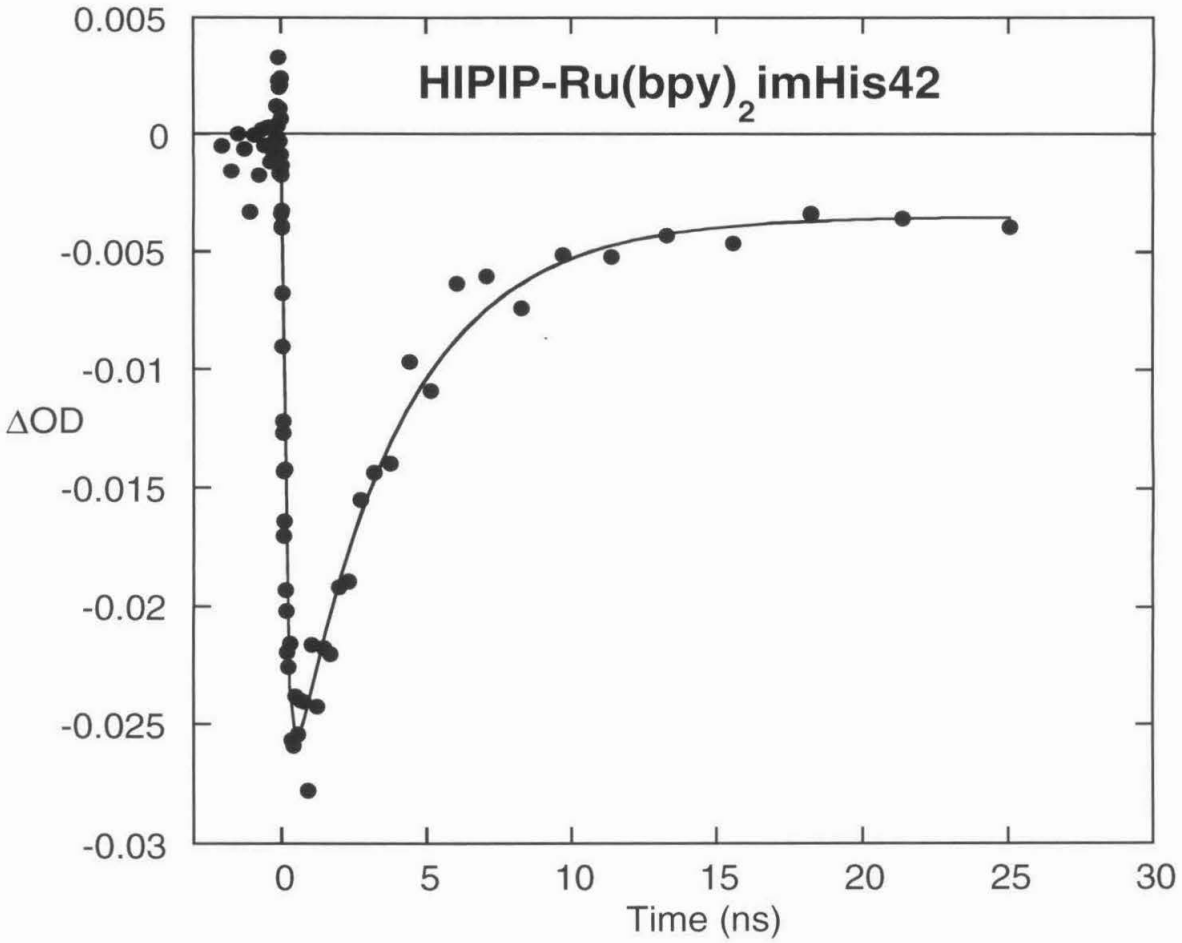
HIPIP-Ru(bpy)2imHis42
0.005
0
-0.005
-0.01
-0.015
-0.02
-0.025
-0.03
ΔOD
0
5
10
15
20
25
30
Time (ns)

Figure 3.13 Transient absorption kinetics of HiPIP-Ru(Me_2bpy)$_2$imHis42. The solid line represents the best fit of a two exponential function that fit the rise and fall of the signal.

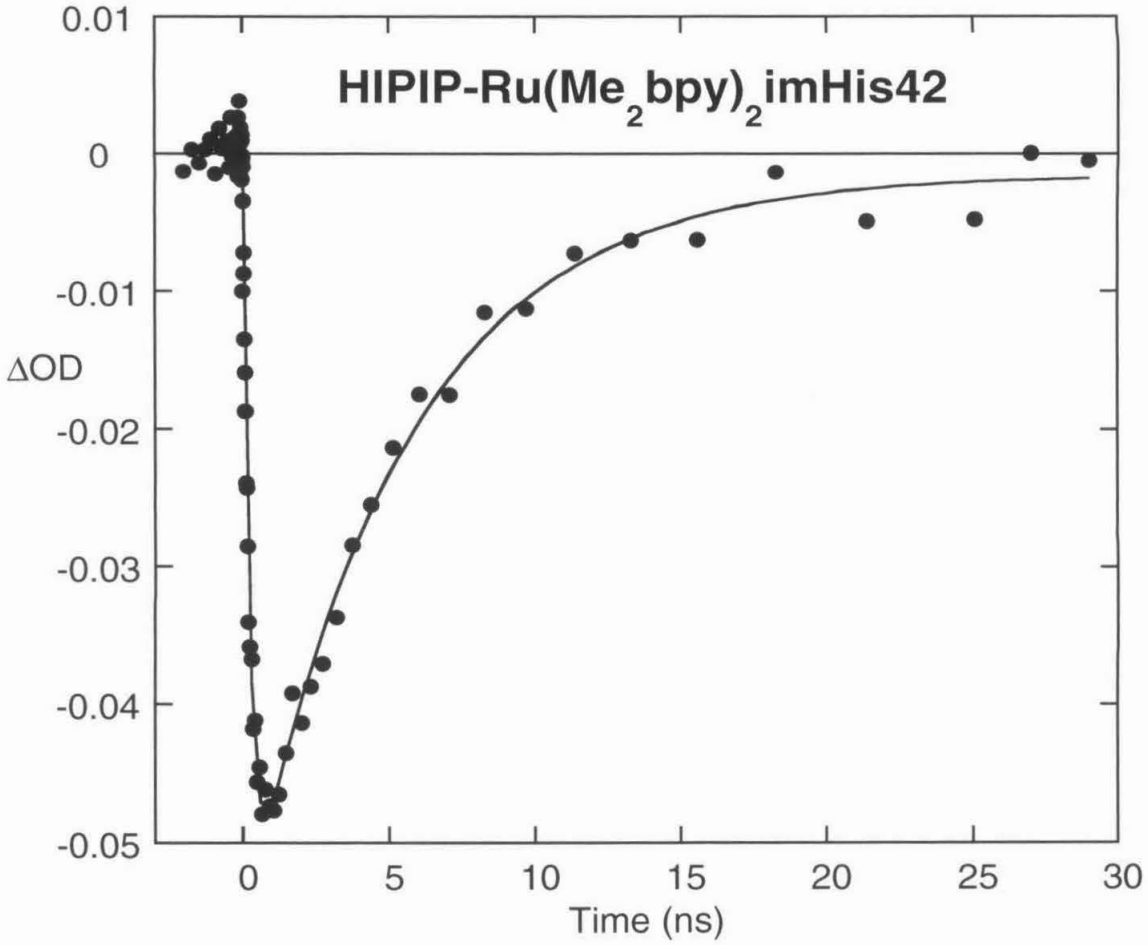
HIPIP-Ru(Me2bpy)2imHis42
0.01
0
-0.01
-0.02
-0.03
-0.04
-0.05
ΔOD
0
5
10
15
20
25
30
Time (ns)

Figure 3.14 Transient absorption kinetics of HiPIP-Ru(bpy)$_2$imHis18. The solid line represents the best fit of a two exponential function that fit the rise and fall of the signal.

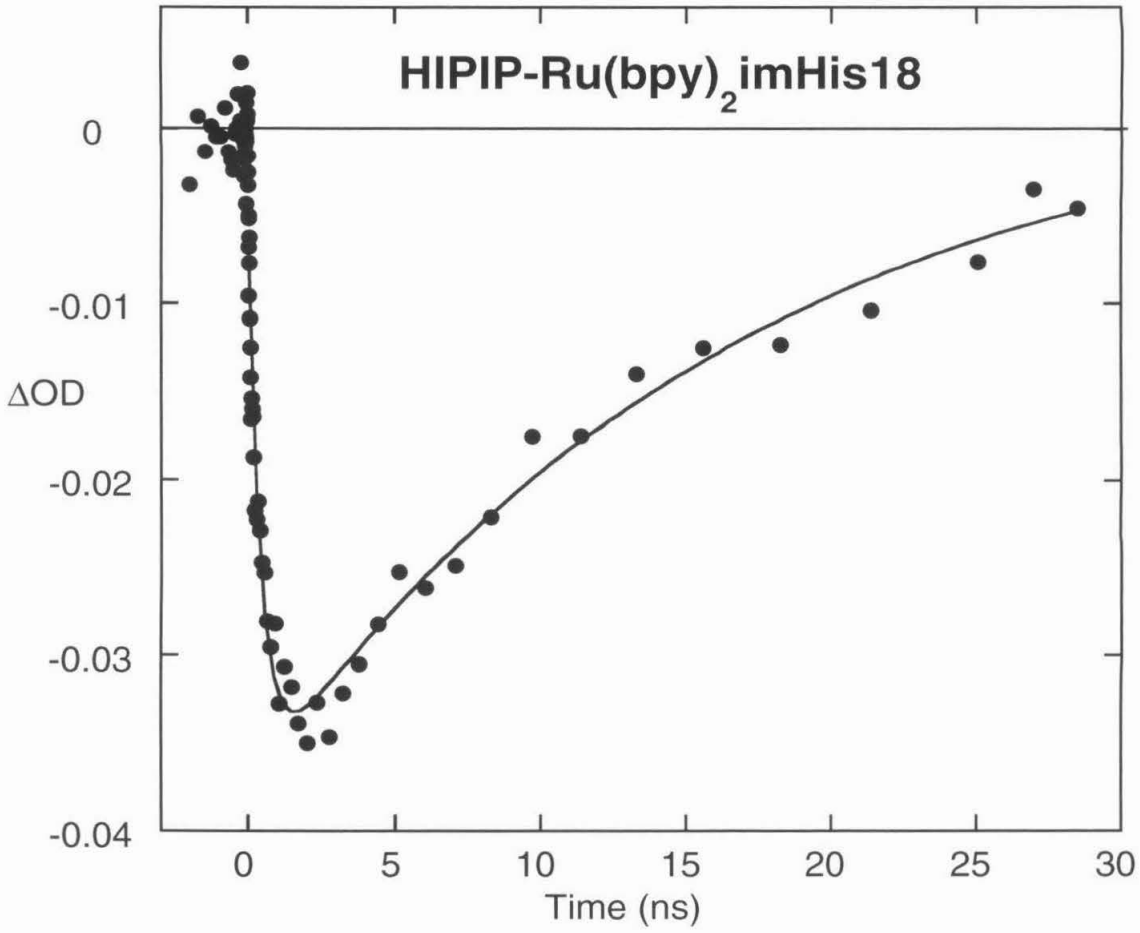
HIPIP-Ru(bpy)2imHis18
0
-0.01
-0.02
-0.03
-0.04
ΔOD
0
5
10
15
20
25
30
Time (ns)

Figure 3.15 Semilogx kinetics plot of HiPIP-Ru(Me_2bpy)$_2$imHis42 illustrating fits for the rise and fall of the signal.

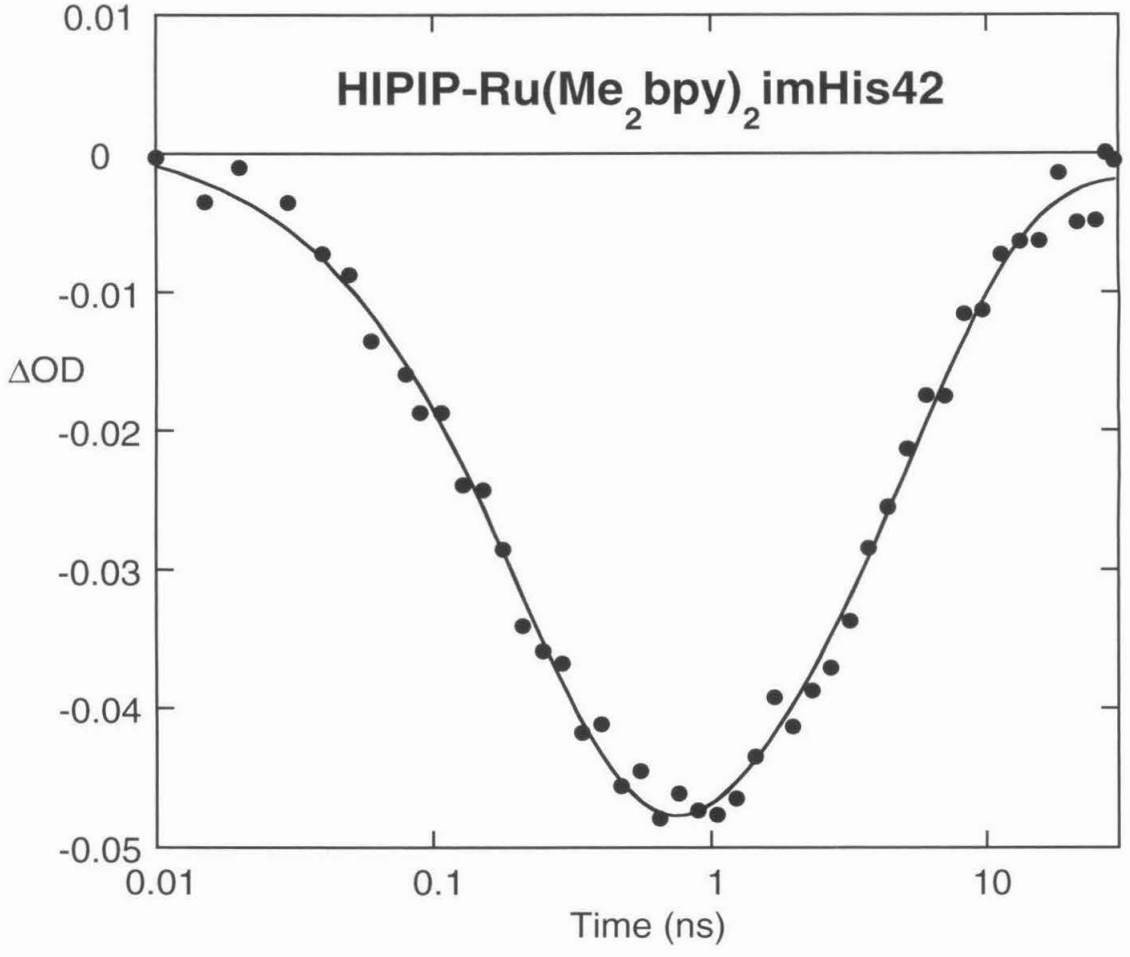
HIPIP-Ru(Me2bpy)2imHis42
0.01
0
-0.01
-0.02
-0.03
-0.04
-0.05
ΔOD
0.01
0.1
1
10
Time (ns)

Table 3.1 Table of rate constants, distances, and driving forces. The driving forces were obtained from redox potentials of iron-sulfur cluster and the ruthenium model complex. For the His42 mutant the redox potential were measured with the modified HiPIP. $E°\{[Ru(bpy)_2(im)(His42)HiPIP[Fe_4S_4]^{3+/2+}] = 0.393$ V; $[Ru^{3+/2+}(bpy)_2(im)(His42)HiPIP = 1.046$ V; For His18,50,81 mutants, the driving force was estimated using the E° for the $(HisX)HiPIP[Fe_4S_4]^{3+/2+}$ (X = 18, 50, 81) and $Ru^{3+/2+}(bpy)_2(im)(His42)HiPIP$. $(His18)HiPIP[Fe_4S_4]^{3+/2+} = 0.341$ V; $(His50)HiPIP[Fe_4S_4]^{3+/2+} = 0.356$ V; $(His81)HiPIP[Fe_4S_4]^{3+/2+} = 0.352$ V } *vs.* NHE. For the Me_2bpy complexes $[Ru^{3+/2+(}Me_2bpy)_2(im)_2] = 0.96$ V was used to calculate the driving force [41].

Sample	k_f (s^{-1})	k_b (s^{-1})	R (Å)	$-\Delta G^o$ (eV)
HiPIP-Ru(bpy)$_2$imHis50	1.7×10^7	1.7×10^6	12.3	0.69
HiPIP-Ru(bpy)$_2$imHis81	1.2×10^{10}	6.1×10^8	12.0	0.69
HiPIP-Ru(Me$_2$bpy)$_2$imHis81	1.2×10^{10}	5.7×10^8	12.0	0.61
HiPIP-Ru(bpy)$_2$imHis42	7.0×10^9	2.7×10^8	11.6	0.65
HiPIP-Ru(Me$_2$bpy)$_2$imHis42	4.5×10^9	1.9×10^8	11.6	0.57
HiPIP-Ru(bpy)$_2$imHis18	1.5×10^9	7.3×10^7	13.7	0.71

Discussion

Arguments for Activationless Back ET

A decrease of ~ 100 meV in $-\Delta G^{o}$ for the $[Fe_4S_4]^{2+} \rightarrow Ru(HisX)^{3+}$ (X = 42, 18) ET reactions has a negligible effect on k_{ET}, which indicates that these reactions occur near the activationless (coupling-limited) regime. A relatively low $[Fe_4S_4]^{3+/2+}$ reorganization energy accords with NMR work that has established that the solution structures of oxidized and reduced *C. v.* HiPIP [49] are very similar. In addition, X-ray studies [3] show only a slight average increase (~ 0.1 Å) in the Fe-S distances upon reduction. Although these data argue for activationless back ET, further driving force dependence data are required to definitively make this point.

Pathways

The ET rates for His81 and His 50 modified HiPIPs differ by greater than two orders of magnitude, despite the fact that the distances between Ru and the closest Fe in the $[Fe_4S_4]$ core are nearly identical (R = 12 Å ± 0.5 Å]) (Table 3.1). Thus, ET studies in these Ru-HiPIPs provides a particularly rigorous test of the tunneling-pathway model. The standard pathway approximation (see page 86) to the coupling element resulted in calculated $[Fe_4S_4]^{2+}$:$[Ru(HisX)]^{3+}$ electronic coupling values consistent with the experimental results (Table 3.2). The calculated couplings of His81 and His50 also varied over two orders of magnitude. This is good evidence that the pathway tunneling model provides a realistic account for the electronic interaction of a donor and an acceptor separated by structural elements of the protein matrix.

The three hundred-fold rate difference between the His 50 and His 81 derivatives is remarkable, given the fact that the closest Ru-Fe distance difference is only 1 Å. This large rate difference is attributable to the relatively weak coupling associated with the 3.8 Å through-space jump in the dominant His50 pathway. Average barrier models, whether calibrated from β values observed in the photosynthetic reaction center [50], or estimated from theoretical analysis of idealized secondary structure elements [13], fail to predict the relative ET rates in Ru-HiPIP by orders of magnitude. The rate differences observed here arise from the connectivity of the superexchange pathways. The relative strengths of these tunneling routes can be understood only in the context of superexchange pathway analysis, which takes the three-dimensional structure of the folded protein into explicit account.

Pathway analysis reproduces the trends in the experimental ET rates, which vary over two orders of magnitude, despite the fact that the metal-to-metal distances vary by just 1 Å or less. The two derivatives with the slowest ET reactions have through-space jumps in their dominant paths (His50, 8 covalent steps and a 3.8 Å through-space jump; His18, 7 covalent steps and a 3.4 Å through-space jump). The better coupled derivatives, His42 (11 covalent steps) and His81 (7 covalent steps, 1 hydrogen-bond), do not require through-space tunneling. The shortest fully covalent bridge available to the His81 derivative is 20 bonds in length, so the strongest superexchange pathway in this derivative includes a hydrogen bond shortcut. Indeed, the relatively rapid electron tunneling in Ru(His81)-HiPIP underscores the importance of hydrogen-bond mediated superexchange. The coupling mediated by hybrid covalent/hydrogen-bonded path in this mutant is comparable in strength to that of the fully covalent bridging unit in the Ru(His42)-HiPIP.

Figure 3.16 Dominant ET path for HiPIP-Ru(bpy_2)im-His50 computed from PATHWAYS model. The His50 path contains 8 covalent steps and a 3.8 Å through-space jump.

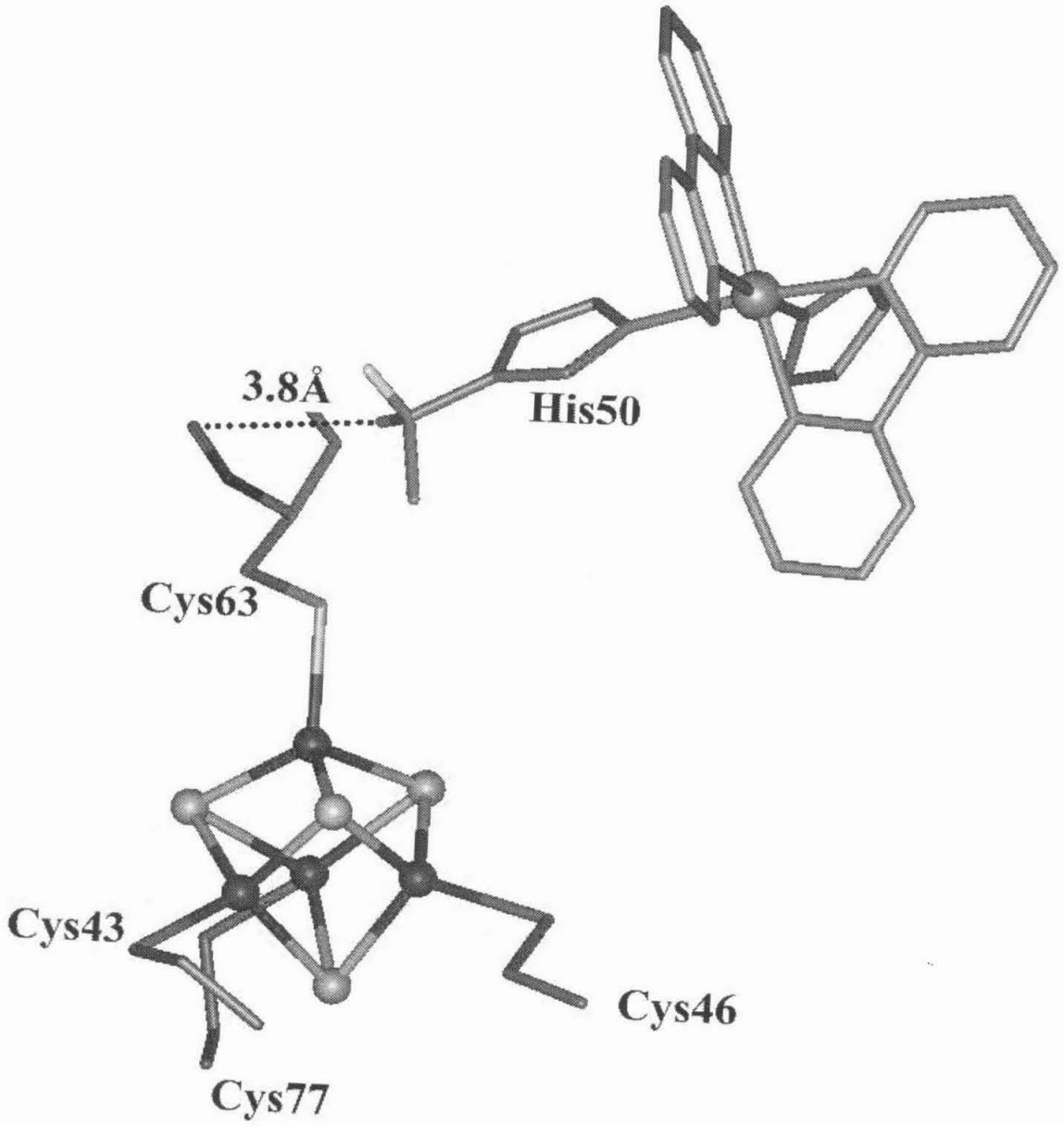
3.8Å
His50
Cys63
Cys43
Cys46
Cys77

Figure 3.17 Dominant ET paths for HiPIP-Ru(bpy_2)im-His81 computed from PATHWAYS model. The His81 path contains 7 covalent steps and one H-bond.

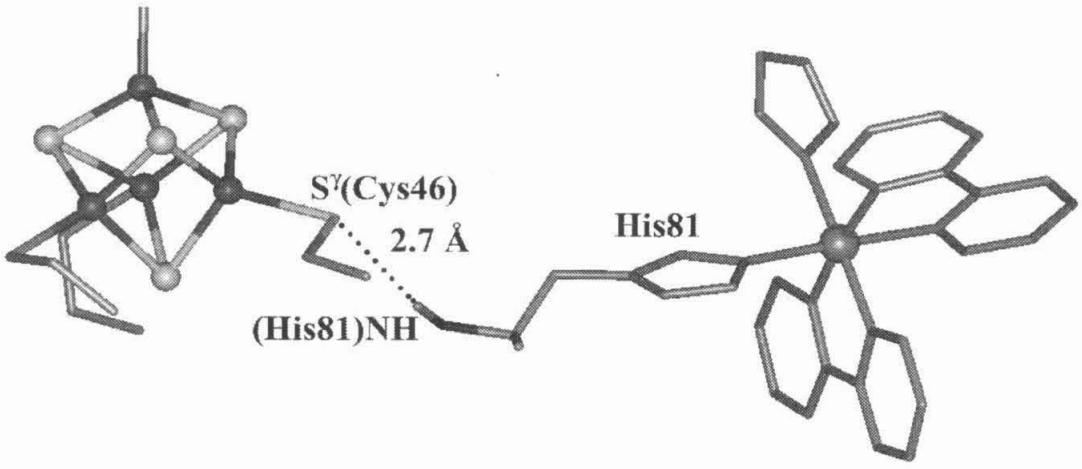
S$^{\gamma}$(Cys46)
2.7 Å
(His81)NH
His81

Figure 3.18 Dominant ET path for HiPIP-Ru(bpy_2)im-His42 computed from PATHWAYS model. The His42 path contains 11 covalent steps.

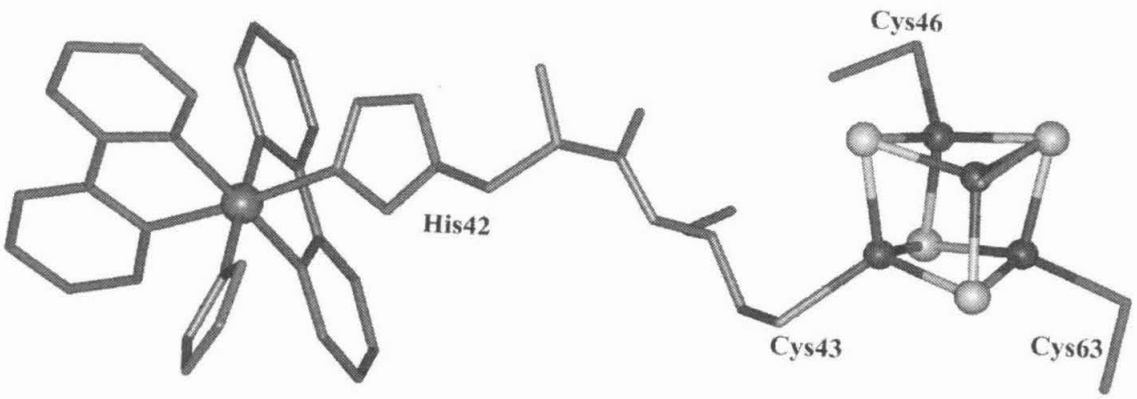
Cys46
His42
Cys43
Cys63

Figure 3.19 Dominant ET path for HiPIP-Ru(bpy_2)im-His18 computed from PATHWAYS model. The His50 path contains 7 covalent steps and a 3.4 Å through-space jump.

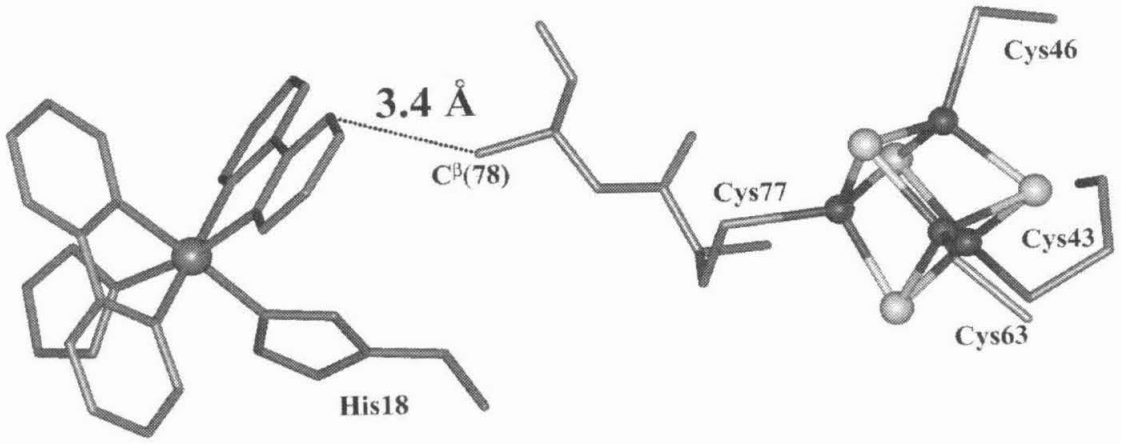
3.4 Å
Cβ(78)
Cys46
Cys77
Cys43
Cys63
His18

Table 3.2 PATHWAY couplings and ET rate constants for Ru(HisX)-HiPIPs.

Ru(HisX)-HiPIP	H_{AB} (calcd) eV	k_{ET} (calcd) s^{-1}; [λ_0(eV)]
His18	5.2×10^{-5}	3.3×10^{7} [0.90]
His42	3.6×10^{-4}	1.7×10^{9} [0.83]
His50	1.5×10^{-5}	2.2×10^{6} [0.91]
His81	3.6×10^{-4}	1.6×10^{9} [0.85]

Figure 3.20 $\log(k_{ET})$ *vs.* D–A distance for a variety proteins and HiPIP. The protein data have been previously compiled [13]. The solid lines that bound the data are distance decays for β values 1.0 $Å^{-1}$ (upper line) and 1.6 $Å^{-1}$ (lower line).

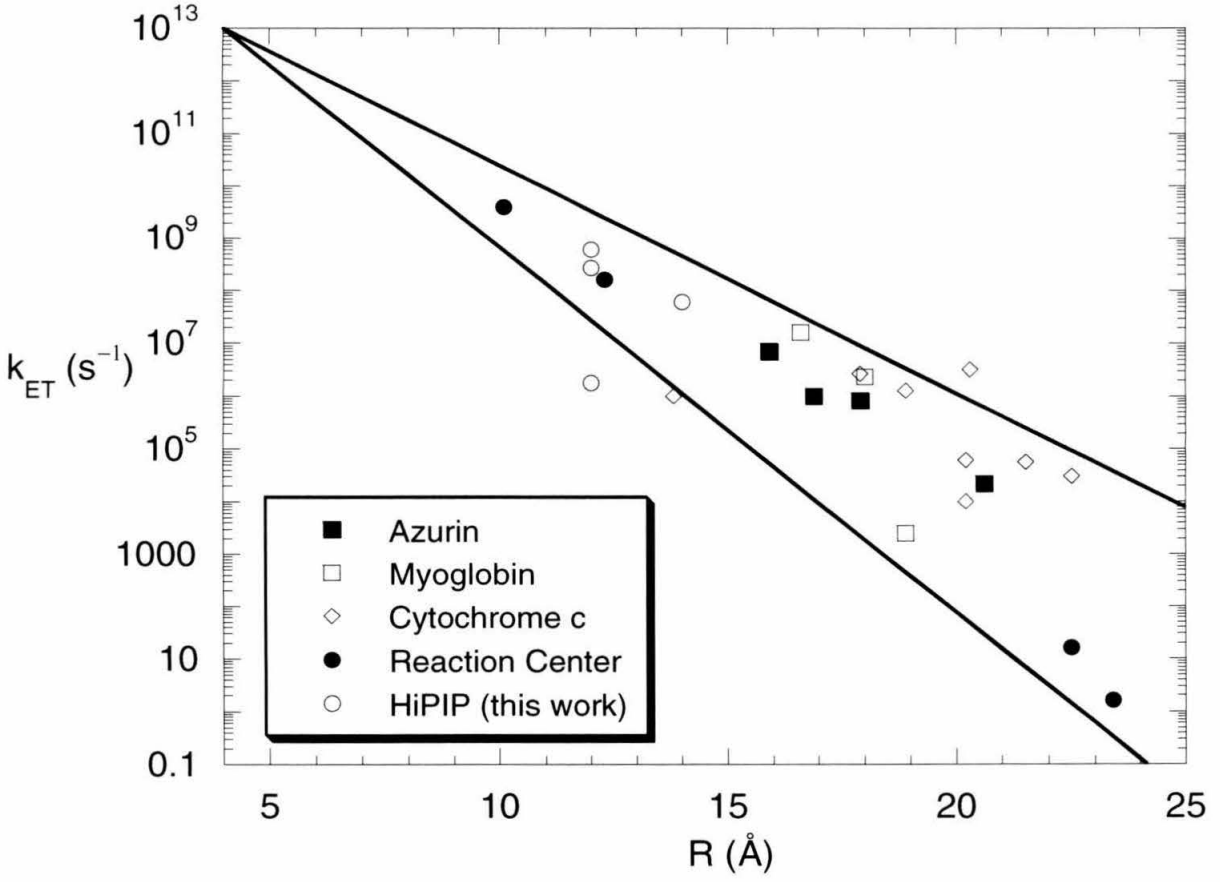
10^{13}
10^{11}
10^{9}
10^{7}
10^{5}
1000
10
0.1
k_{ET} (s^{-1})
5
10
15
20
25
R (Å)
Azurin
Myoglobin
Cytochrome c
Reaction Center
HiPIP (this work)

Effect of Protein Dynamics

Protein structures are in thermal flux, and continuously transfer from one conformational state to another. The nature of protein motions can be divided into an energetic hierarchy or 'landscape' [51-53]. This is paralleled by a hierarchy of relaxation times that ascend from fast lattice-like motion in the protein interior, *via* slower large-amplitude motion of surface residues, to collective dynamics in which large parts of the proteins are engaged. When these motions are required to reach the transition state geometry, then they are part of the reaction coordinate and contribute to the total reorganization energy. Consequently, if the electronic coupling becomes sufficiently strong, then ET can become limited on the timescale of these motions. Specific incorporation of friction, as in the adiabatic-nonadiabatic transition models (Chapter 1, page 27), is then applicable [54].

Further, protein dynamics also involve breaking and forming of hydrogen bonds, and changes in through-space distances. These motions can lead to gated ET, where conformational dynamics constitute separate chemical kinetic steps [55,56]. When populations of more and less strongly coupled conformational isomers exist, multiexponential kinetics can be expected.

The data reported here represent the fastest ET kinetics measured to-date in Ru-modified proteins. In this study we have not found evidence of limiting or gating behavior in the ET kinetics of the various modified HiPIPs. The fastest back ET rate from His81 mutant is 6.1×10^8 s^{-1}, and thus the adiabatic limit occurs on a timescale less than or equal to one nanosecond.

If the observed rise of the His81 transient (k_{obs}) is assigned to forward ET (k_f) (Figure 3.2), then the adiabatic limit is less than or equal to 80 ps. This assignment needs to be confirmed by measuring the yield of ET product, which is a measurement that was not possible at the time of these experiments. However, indirect evidence suggests that $k_{obs} = k_{ET(forward)}$. Consider Equation 3.3, which shows that the rate of excited-state decay (k_{obs}) is equal to the sum the rates of all processes that deactivate the excited state.

Equation 3.3. $$k_{obs} = k_o + k_{et} + k_{ET}$$

Where k_o is the decay rate of the unquenched chromophore, and k_{et} is the rate of energy transfer. In order for $k_{obs} = k_{ET}$, k_o and k_{et} have to be much slower than k_{ET}. First, the rate of the unquenched ruthenium model complex has been independently measured, $k_o = 1.5 \times 10^7\ s^{-1}$, to be ~3 orders of magnitude slower than k_{obs} (His81). Second, the rate of energy transfer by electron-exchange interactions (Dexter) are believed to decay twice as fast with distance as the rate of ET. Third, energy transfer by Coulombic interactions (Förster) is mediated by though-space dipole-dipole interactions, and it has already been dramatized that through-space interactions fail to explain the rate difference between His50 and His81. Thus, this indirect evidence indicates that forward ET occurs in 80 ps and suggests that the adiabatic limit occurs on a timescale less than 80 ps in HiPIP.

Conclusions

The ET kinetics presented here for ruthenium modified HiPIPs clearly show the importance of the structural details of the intervening protein medium. A large through-space jump in His50 explains the factor of 300 in rate difference with His81. Also highlighted is the importance of H-bonds that short-circuit longer covalent paths and lead

to strong coupling and fast ET rates in His81. Finally, these are the fastest ET measured to-date for ruthenium modified proteins, and are not limited by the rate of protein medium reorganization.

References

[1] P Bonora, I Principi, B Monti, S Ciurli, D Zannoni, A Hochkoeppler, A. *Biochim. Biophys. Acta*, **141**, 51-60 (1999).

[2] CW Carter, J Kraut, ST Freer, N-H Xuong, RA Alden, RG Bartsch, *J. Biol. Chem.*, **249**, 4212-4225 (1974).

[3] CW Carter, J Kraut, ST Freer, RA Alden, *J. Biol. Chem.*, **249**, 6339-6346 (1974).

[4] A Soriano, JA Cowan, *Inorg. Chim. Acta*, **251**, 285-290 (1996).

[5] S Bian, CF Hemann, R Hille, JA Cowan, *Biochemistry*, **35**, 14544-14552 (1996).

[6] L Stryer, *Biochemistry*, 3rd edn., Freeman, San Francisco (1995).

[6b] DE McRee, *J. Mol. Graphics*, **10**, 44 (1992).

[6c] S Faham, MW Day, WB Connick, BR Crane, A Di Bilio, WP Shaefer, DC Rees, HB Gray, H. B. *Acta Cryst.*, **D55**, 379-385 (1999).

[7] RA Marcus, N Sutin, *Biochim. Biophys. Acta*, **811**, 265-322 (1985).

[8] DN Beratan, JN Onuchic, JJ Hopfield, *J. Chem. Phys.*, **86**, 4488-4498 (1987).

[9] JN Onuchic, DN Beratan, *J. Chem. Phys.*, **92**, 722-733 (1990).

[10] JN Onuchic, DN Beratan, JR Winkler, HB Gray, *Annu. Rev. Biophys. Biomol. Struct*, **21**, 349-377 (1992).

[11] DN Beratan, JN Betts, JN Onuchic, *J. Phys. Chem.*, **96**, 2852-2855 (1992).

[12] DN Beratan, JN Betts, JN Onuchic, *Science*, **252**, 1285-1288 (1991).

[13] HB Gray and JR Winkler, *Annu. Rev. Biochem.*, **65**, 537-561 (1996).

[14] HB Gray and JR Winkler, *J. Biol. Inorg. Chem.*, **2**,.399-404 (1997).

[15] J Ulstrup, *Charge Transfer Processes in Condensed Media*, Springer-Verlag, Berlin (1979).

[16] KM Yocom, JB Shelton, JR Shelton, WE Schroeder, G Worosila, et al., *Proc. Natl. Acad. Sci.*, **79**, 7052-7055 (1982).

[17] CR Matthews, PM Erickson, DL Van Vliet, M Petersheim, *J. Am. Chem. Soc.*, **100**, 2260-2262 (1978).

[18] JR Winkler, DG Nocera, KM Yocom, E Bordignon, HB Gray, *J. Am. Chem. Soc.*, **104**, 5798-5800 (1982).

[19] DG Nocera, JR Winkler, KM Yocom, E Bordignon, HB Gray, *J. Am. Chem. Soc.*, **106**, 5145-5150 (1984).

[20] SS Isied, C Kuehn, G Worosila, *J. Am. Chem. Soc.*, **106**, 1722-1726 (1984).

[21] H Elias, MH Chou, JR Winkler,*J. Am. Chem. Soc.*, **110**, 429-434 (1988).

[22] TJ Meade, HB Gray, JR Winkler, *J. Am. Chem. Soc.*, **111**, 4353-4356 (1989).

[23] MJ Therien, MA Selman, HB Gray, I-J Chang, JR Winkler, *J. Am. Chem. Soc.*, **112**, 2420-2422 (1990).

[24] RJ Crutchley, WR Ellis, HB Gray, *J. Am. Chem. Soc.*, **107**, 5002-5004 (1985).

[25] AW Axup, M Albin, SL Mayo, RJ Crutchley, HB Gray, *J. Am. Chem. Soc,* **110**, 435-439 (1988).

[26] JL Karas, CM Lieber, HB Gray, *J. Am. Chem. Soc.*, **110**, 599-600 (1988).

[27] JR Winkler, HB Gray,*Chem. Rev.*, **92**, 369-379 (1992).

[28] C Fenwick, S Marmor, K Govindaraju, AM English, JF Wishart, J Sun, *J. Am. Chem. Soc.*, **116**, 2169-3170 (1994).

[29] MP Jackman, MC Lim, GA Salmon, AG Sykes, *J. Chem. Soc. Chem. Comm.*, 179-180 (1988).

[30] MP Jackman, MC Lim, GA Salmon, AG Sykes, *J. Chem. Soc. Dalton Trans.*, 2843-2850 (1988).

[31] NM Kostic, R Margalit, C-M Che, HB Gray, *J. Am. Chem. Soc.*, **105**, 7765-7767 (1983).

[32] MP Jackman, AG Sykes, *J. Chem. Soc.,* 65-66 (1987).

[33] MP Jackman, J McGinnis, R Powls, GA Salmon, AG Sykes, *J. Am. Chem. Soc.,* **110**, 5880-5887 (1988).

[34] O Farver, I Pecht, *FEBS Lett.*, **244**, 379-382 (1989).

[35] O Farver, I Pecht, *Inorg. Chem.*, **29**, 4855-4858 (1990).

[36] BA Jacobs, MR Mauk, WD Funk, RTA Gillivray, AG Mauk, HB Gray, *J. Am. Chem. Soc.*, **113**, 4390-4394 (1991).

[37] P Osvath, GA Salmon, AG Sykes, *J. Am. Chem. Soc.*, **110**, 7114-7118 (1988).

[38] I-J Chang, HB Gray, JR Winkler, *J. Am. Chem. Soc.*, **113**, 7056-7057 (1991).

[39] DS Wuttke, MJ Bjerrum, JR Winkler, HB Gray,*Science*, **256**, 1007-1009 (1992).

[40] DR Casimiro, JH Richards, JR Winkler, HB Gray, *J. Phys. Chem.*, **97**, 13073-13077 (1993).

[41] GA Mines, MJ Bjerrum, MG Hill, DR Casimiro, I-J Chang, JR Winkler, HB Gray, *J. Am. Chem. Soc.*, **118**, 1961-1965 (1996).

[42] R Langen, I-J Chang, JP Germanas, JH Richards, JR Winkler, HB Gray, *Science*, **268**, 1733-1735 (1995).

[43] E Babini, I Bertini, M Borsari, F Capozzi, A Dikiy, LD Eltis, C Luchinat, C. *J. Am. Chem. Soc.*, **118**, 75-80 (1996).

[44] E Babini, I Bertini, M Borsari, F Capozzi, *Inorg, Chim. Acta*, **276**, 230-233 (1998).

[45] AJ Di Bilio, C Dennison, HB Gray, BE Ramirez, AG Sykes, *J. Am. Chem. Soc.*, **120**, 7551-7556 (1998).

[46] DW Low, JR Winkler, HB Gray,*J. Am. Chem. Soc.*, **118**, 117-120 (1996).

[47] RG Bartsch, *Methods Enzymol.*, **23**, 644-649 (1971).

[48] K Yamakawa, CPJ Barty, H Shiraga, Y Kato, *IEEE J. Quant. Elect.*, 288-294 (1991).

[49] I Bertini, A Dikiy, DH Kastrau, DHW Luchinat, P Sompornpisut, *Biochemistry*, **34**, 9851-9858 (1995).

[50] CC Moser, JM Keske, K Warncke, RS Farid, LP Dutton, *Nature*, **355**, 796-802 (1992).

[51] GA Welch, Ed., *The fluctuating enzyme*, Wiley, New York (1986).

[52] RH Austin, KW Beeson, L Eisenstein, H Frauenfelder, IC Gunsalus, *Biochem.*, **14**, 5355 (1975).

[53] PJ Steinbach, A Ansari, J Berendzen, et al.*Biochem*, **30**, 3988 (1991).

[54] H Sumi, *J. Phys. Chem.*, **95**, 3334 (1991).

[55] H Sumi, J Ulstrup, *Biochim. Biophys. Acta*, **955**, 26 (1988).

[56] B Hoffman, MA Ratner, *J. Am. Chem. Soc.*, **109**, 6237 (1987).

[57] MK Johnson, *Current Opinion in Chemical Biology*, **2**, 173-181 (1998).

[58] JM Mouesca, et al., *Inorg. Chem.*, **34**, 4347-4359 (1995).

[59] SJ Yee, RH Holm, E Münck, *J. Am. Chem. Soc.*, **119**, 8732-8733 (1997).

Chapter 4

Electron Tunneling through Water

'The most abundant substance on Earth is the most mysterious material known'.

CH Cho, S Singh, GW Robinson, *Farad. Disc.*, **103**, 19-27 (1996).

Water is 'a still poorly known liquid'.

Y Marechal, in *Hydrogen Bond Networks*, ed MC Bellisent-Funnel and J Dore, NATO ASI series, Kluwer, Dordrecht (1994).

Water is an 'anamalous liquid and solvent'.

J Jonas, A Jonas, *Annu. Rev. Biophys. Biomol. Structure*, **23**, 287 (1994).

'It is the most well-known and the least understood compound'.

HJC Berendsen, *Natuurkd. Voordr.*, **59**, 85 (1981).

Abstract

The distance dependence of photoinduced intermolecular electron transfer between excited $[Ru(tpy)_2]^{2+}$ (tpy = 2,2':6,2"-terpyridine) and $[Fe(OH_2)_6]^{3+}$ ions in aqueous glasses at 77 K has been determined. Luminescence-decay kinetics and quantum yields for a series of ferric ion concentrations are analyzed in the context of semiclassical ET theory and are consistent with an exponential distance decay factor (β) of 1.68 ± 0.03 $Å^{-1}$.

Introduction

Water is the natural solvent for the chemical processes of life. Thousands of chemical reactions that keep an organism alive occur in the aqueous solutions of blood, digestive fluids, and cytoplasm. The simplest type of reaction in nature is electron transfer (ET), since no chemical bonds are formed or broken in its process; nonetheless, ET is the fundamental reaction in photosynthesis and aerobic respiration. Redox sites embedded in a hydrophobic protein matrix are exposed to water in varying degrees. The unique physical properties of water influence ET in a variety of ways and can serve as a tuning element for optimizing the rate of ET.

The polarity of water stabilizes the charge-separated product, and results in a large solvent reorganization energy. Thus, varying water exposure of the redox centers in proteins can influence the rate and directionality of ET (forward *vs.* back). Further, the dynamics of water reorientation can limit the rate of ET at around ~1 ps (see Chapter 1, page 27). Finally, water can mediate electronic coupling between the redox couple *via* a superexchange mechanism, which is the subject of this chapter. Water structures that

reside in the protein matrix range in size from single molecules to larger assemblies or chains, which raises the question if these structures should be considered in ET coupling pathway analysis (Figure 4.1, [1]).

The efficiency of the solvent as a medium for ET remains a relatively unexplored aspect of long-range ET studies. Solvent-mediated ET is difficult to ascertain because, unlike the covalent donor-bridge-accceptor systems, the bridge consists of a dynamic medium with translational degrees of freedom. Diffusion occurs on a nanosecond timescale and accordingly, distance dependence information of ET must be obtained on an even faster time scale. On the subnanosecond timescale, however, ET occurs over a small distance range (~5-7 Å), making distance decay measurements prone to error. Alternatively, solvent glasses at low temperature eliminate the translational degrees of freedom on the timescale of the experiment. In the absence of diffusion intermolecular ET can occur over long distance (>20 Å), providing a suitable range to measure distance decays.

Water-mediated ET is not a new issue and has been discussed since the early days of ET. In 1958, Klotz *et al.* [2] theorized that a number of important long-range biological ET processes might occur *via* water bridges. This was followed in 1963 when Horne performed an experimental study of Fe^{2+}–Fe^{3+} electron-exchange kinetics in ice media [3]. He concluded that ET can occur over 'very great distances' (~100 Å) in aqueous media by a water-bridging mechanism. These results were challenged three years later by Nitzan and Wahl who stated that although exchange does indeed occur, they were unable to reproduce the rate measurements and therefore could not support Horne's suggestion concerning the mechanism [4].

Figure 4.1 Structure of cytochrome *f* containing a chain of 5 water molecules leading from the surface of the protein to the active site.

The following decade, Miller performed pulse-radiolysis experiments in frozen aqueous glasses [5,6]. The tunneling distance of solvated electrons trapped in the glass matrix was described in terms of a barrier penetration model combined with a 'sphere of action' model that assumes all electrons within a critical transfer radius have reacted with acceptors. While, sphere-of-action models can provide good fits to experimental data they provide limited physical insight [7,8]. However, subsequent unpublished analyses of the data in the context of superexchange models with an exponential distance dependence yielded β values of ~ 1 $Å^{-1}$ [9].

Further pulse radiolysis experiments in aqueous glasses were performed by Khairutdinov, Zamaraev, and Zhdanov [10]. In addition, they reanalyzed Miller's pulse radiolysis data of solvated electrons in aqueous glasses. A compilation of data of ET between a spectrum of donor and acceptor types in acidic and basic glasses was analyzed with superexchange type models to give a β range of 0.5-1.0 $Å^{-1}$.

The distance dependence of solvent-mediated ET has also been measured in fluid solution [11-14]. Transient conductance measurements of solvated electrons in fluid aqueous solution determined a β value of 0.75 $Å^{-1}$ [11]. Other interesting experiments in fluid organic solutions in which ET rates in C-shaped molecules were compared to their linear-shaped isomers have provided evidence for solvent-enhanced electronic coupling, although no distance dependence data were reported [12-14]. In addition, intermolecular ET in fluid organic solutions was analyzed with a sophisticated through-solvent theory that includes solvent structure and hydrodynamic effects [7]. Distance dependence

information is inherently difficult to glean from intermolecular ET experiments in fluid solutions (*vide supra*).

McLendon [15] performed photoinduced ET reactions in glucose glasses and was the first to report a distance decay parameter (β = 1.4 $Å^{-1}$) that was derived from a luminescence-decay analysis based on Inokuti-Hirayama theory. The Inokuti-Hirayama theory [16] assumes an exponential distance dependence and a random distribution of donor and acceptor molecules (*vide infra*) and reflects the physical properties of the system more accurately than a 'sphere-of-action' model.

A number of theoretical studies have examined the effects of water mediated electronic coupling. An early study by Larsson [17] considered a simple McConnell superexchange model [18] for Fe^{3+}–Fe^{2+} self-exchange and reported a β value of 2.4 $Å^{-1}$. However, a lower β value would result if the bulk solution ionization potential (~9 eV) for water is used in the calculation rather than the gas–phase ionization potential (12.6 eV). Newton reported a β value of 1.0 $Å^{-1}$ from *ab initio* results of water-mediated electronic-coupling strengths [19]. However, his current unpublished INDO results give β values of around 1.5 $Å^{-1}$ [20]. Recent calculations by Cave [21] report a comparison of *ab initio* and INDO results for electronic coupling in water. The *ab initio* results give a β value range of 1.5–1.8 $Å^{-1}$ depending on the geometry of the intervening water molecules, while the INDO calculations result in a β value of 2.0 $Å^{-1}$.

The β values reported for water [5,6,10,11,17,19-21] (0.75-2.4 $Å^{-1}$) span the range of β values found for ET across covalent bridges (0.8-1.2 $Å^{-1}$) [22-30]. Since ET is mediated by the most efficient pathways, the question arises to what extent

'intramolecular' ET is mediated by the solvent that surrounds a given donor-bridge-acceptor system. In order to address this question, the efficiency of solvent-mediated ET must be known. To this end, we have examined excited-state ET reactions in aqueous glasses to determine the efficiency of water-mediated ET. Here we report the distance decay factor (β) for electron tunneling in aqueous glasses obtained by analysis of luminescence-decay and quantum yield data.

Background

The Nature of the Vitreous State

Upon rapid cooling to temperatures below the freezing point, alcohols, aqueous solutions (concentrated acids, salts and alkalis), and some organic solvents solidify to form amorphous glasses instead of crystals. In general, crystalline solvents are of no use as a medium for ET studies since solutes (i.e., donors and acceptors) are extruded upon crystallization. The structure of the amorphous glass, however, is analogous to the liquid structure, and is often considered the instant mould of liquid. The final state of a liquid upon cooling depends on the relative rates of viscosity increase *vs.* crystal formation. In general, the probability of glass formation is increased by increasing the rate of the temperature drop, and by reducing the volume of the sample [10]. The final density of the glass, and thus the concentration of solutes, depends on the rate of cooling, because the change in volume is delayed with respect to the change in temperature [32]. The scale of the concentration variation from this effect, however, does not exceed 5% in aqueous

glasses, which is the maximum volume change upon a temperature change from 300 to 77 K.

In frozen media, ET that was rapid at room temperature often ceases, which can be ascribed to lower thermal energy and freezing of the solvent coordinate. This was the case in our studies when low reduction-potential organic quenchers like methyl-viologen or tetracyanoethelene were used as electron acceptors. The high reduction potential of ferric ion (0.77 eV), however, provided enough free energy for the ET reaction to occur at 77 K. At room temperature, the orientational motions of the solvent dipoles contribute to the reorganizational energy [33-35]. When these motions are frozen, the solvent reorganization energy becomes part of the free energy change (Figure 4.2) [36-39]. The change in energetics arises because ET occurs with solvent dipoles in the orientations of the initial state. Thus, the products formed in these orientations are at high energy compared to products formed in fluid solution because the charge-separated state is no longer stabilized by the solvent.

Electronic Structure of Water

The electronic properties of bulk water are in general discussed in terms of amorphous semiconductors. The band gap (E_g) between the valence and conduction band and the location of the conduction band edge (E_c) relative to the vacuum level are still current topics in the literature [40,41]. The threshold energy for photoelectron emission by liquid water (E_t) has been estimated from thermodynamic cycles, giving a value of E_t = 9 eV [42]. In addition, it has been directly determined by photoelectrochemical studies

Figure 4.2 Free energy diagram for ET in fluid (solid line) and rigid (dashed line) media.

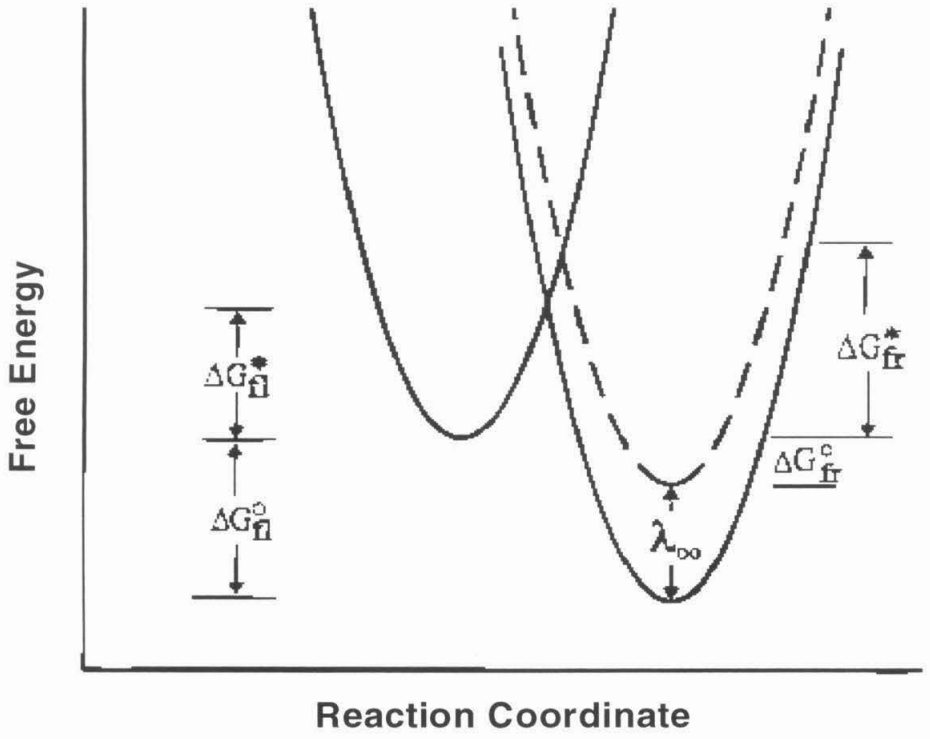
Free Energy
ΔG^{*}_{fl}
ΔG°_{fl}
λ_{oo}
ΔG^{*}_{fr}
ΔG°_{fr}
Reaction Coordinate

Figure 4.3 Energy diagram illustrating the water band gap overlaid with the energy of solvated electrons, $[Ru(bpy)_3]^{2+}$ and Fe_{aq}^{3+} ion for reference. The energy scale on the left originates at the vacuum level, and the right scale originates *vs.* NHE [64].

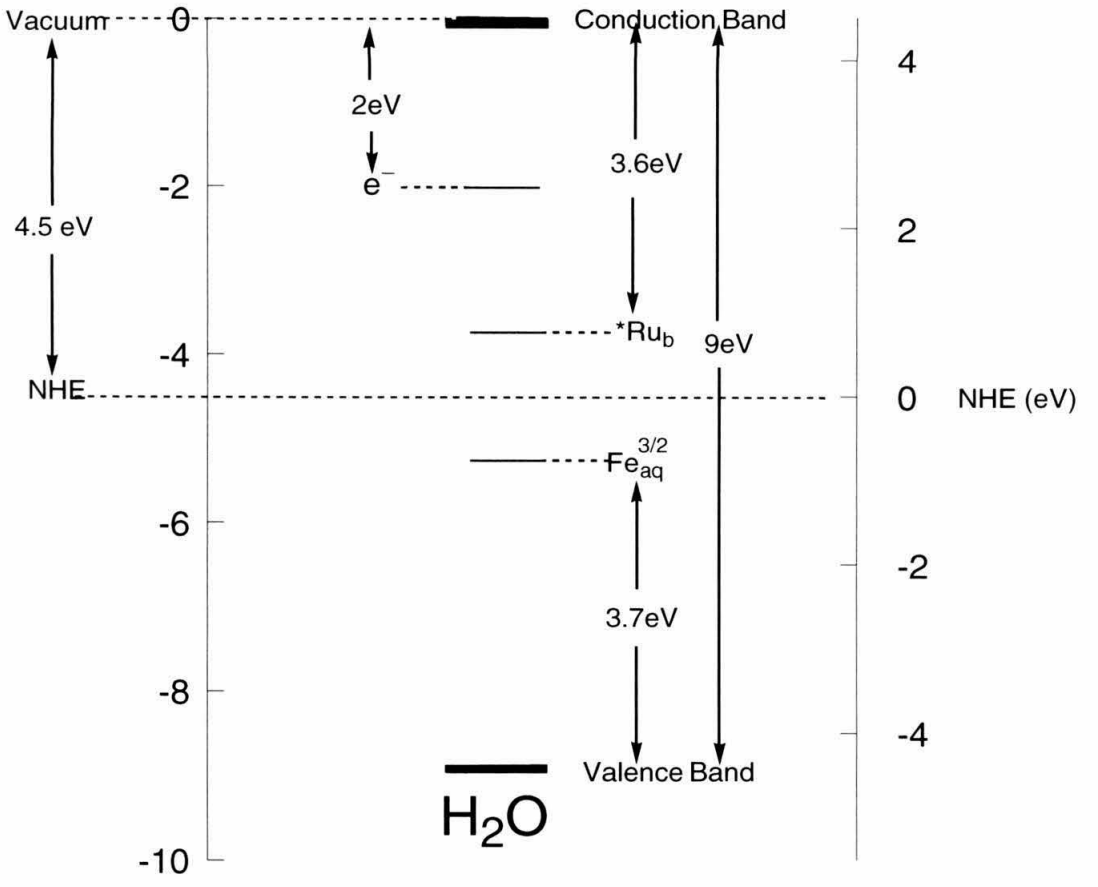
Vacuum
0
Conduction Band
4
2eV
3.6eV
e⁻
-2
4.5 eV
2
*Ru_b
9eV
-4
NHE
0
NHE (eV)
Fe_aq^3/2
-6
-2
3.7eV
-8
-4
Valence Band
H2O
-10

with reported values of E_t = 9.3 ± 0.3 eV [43], 9.3 ± 0.1 eV [44], and 10.06 ± 0.1 eV [45,46].

Estimates of the energy band gap of water, $E_g = E_t - E_c$, from threshold photoelectron energies values (E_t = 9.5 ± 0.5 eV) and conduction-band minimum energy values (E_c = –1± 0.2 eV [47-49] and 0.06 ± 0.6 eV [41]) determine an average band gap E_g =8.6 ± 0.7 eV. This is the average value of all the semi-empirical determinations in the literature [40], which is quite close to the energy gap adopted for ice: 9 eV [50], 7.8 eV [51,52], and 10.9 eV [53]. Figure 4.3 shows the band gap for water in relation to the excited state $[Ru(bpy)_3]^{2+}$ donor and ferric ion acceptor.

Experimental

Materials

$[Ru(tpy)_2]Cl_2$ was synthesized and purified according literature methods [31]. $(NH_4)Fe(SO_4)_2$ (99.99%), H_2SO_4 (double distilled), D_2O (99.9%), D_2SO_4 (99.9%) and HSO_3F (Aldrich) were used without further purification.

Preparation of Glasses

Stock solutions of 25% v/v acid (H_2SO_4, HSO_3F in H_2O and D_2SO_4 in D_2O) containing ~10 μM $[Ru(tpy)_2]Cl_2$ were prepared for each experiment. A 0.5 M $(NH_4)Fe(SO_4)_2$ solution was prepared with the $[Ru(tpy)_2]Cl_2$ stock solution and serial dilution (also with the $[Ru(tpy)_2]Cl_2$ stock solution) gave a $[Fe(H_2O)_6]^{3+}$ concentration range of 0-0.5 M. This procedure insured equivalent concentrations of $[Ru(tpy)_2]^{2+}$ for all the samples in a series. The solutions were degassed with Ar for 5 minutes in a 5 mm OD

tube that fit into a finger dewar (Wilmad). The samples were frozen slowly (dipping rate of ~1 cm/5 sec) in liquid nitrogen to avoid formation of cracks in the aqueous glasses.

Instrumentation

Relative Quantum Yield

The 514 nm line from an argon ion laser (Coherent) was used for excitation. The luminescence was dispersed in a 1.5 m focal length monochromator (Spex) and detected with a liquid nitrogen cooled CCD (Princeton Instruments). The CCD provided reliable luminescence intensity measurements over three orders of magnitude; a large range of quencher concentration (0-0.5 M) could be used without changing the instrument parameters. Luminescence quantum yield experiments at liquid nitrogen temperatures are difficult to perform reproducibly. The experiment is very sensitive to sample positioning and homogeneity of the optical glass. In order to test our ability to reproducibly position samples, we performed both steady-state and time-resolved Stern-Volmer experiments with $[Ru(bpy)_3]^{2+}$ as the chromophore and $[Ru(NH_3)_6]^{3+}$ as the quencher (Figure 4.4). We obtained excellent linear correlation (R=0.9999) when the integrated luminescence intensity was plotted against luminescence lifetime, thus proving that we could position samples reproducibly. Moreover, reflections from small cracks in the optical glass result in large deviations in luminescence intensity by causing directed luminescence and multiple path excitation. In order to minimize the intensity deviations, the finger dewar containing the sample was placed in an integrating sphere. A steady flow of nitrogen gas eliminated water condensation on the optical faces. Each quantum yield experiment was carried out three times with intensity fluctuations ~ 1% (stdev/mean).

Figure 4.4 Steady-state *vs.* lifetime Stern-Volmer quecching plot of $[Ru(bpy)_3]^{2+}$ luminescence quenched by $[Ru(NH_3)_6]^{3+}$. The lifetime measurement is position insensitive while the steady-state measurement is very position sensitive. The degree of linearity attests to the accuracy and reproducibility of the luminescence quantum-yield experiment.

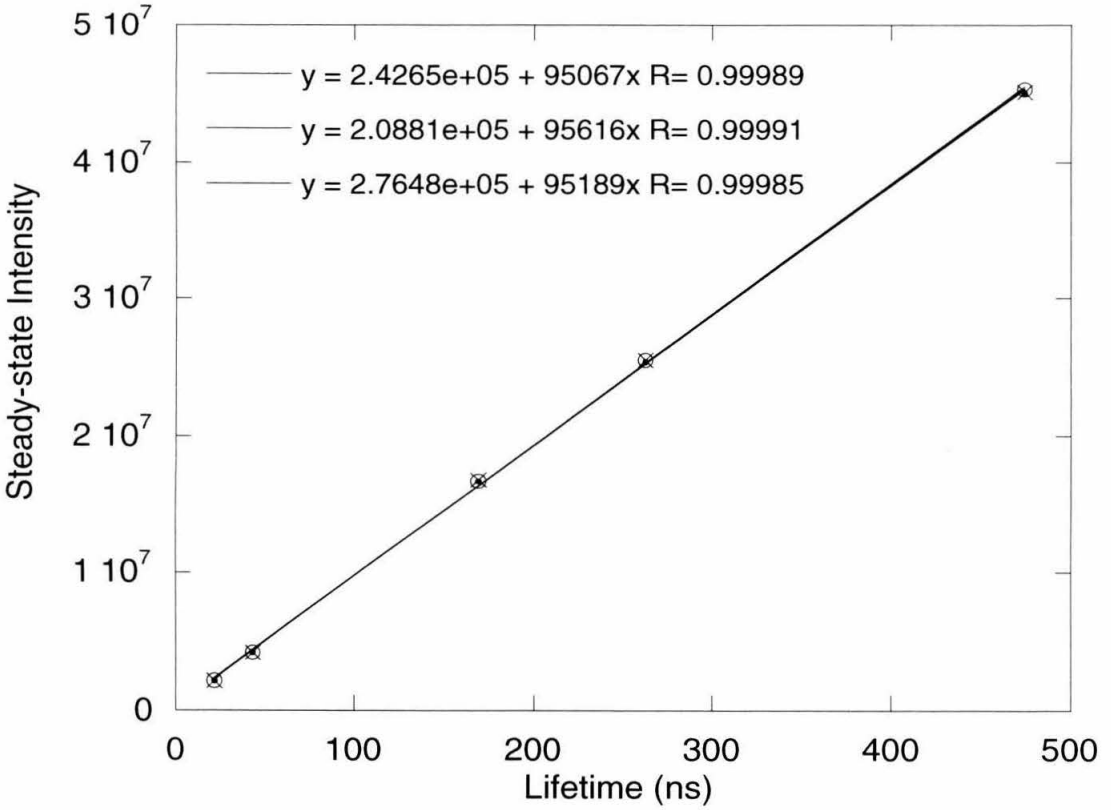
y = 2.4265e+05 + 95067x R= 0.99989
y = 2.0881e+05 + 95616x R= 0.99991
y = 2.7648e+05 + 95189x R= 0.99985
Steady-state Intensity
Lifetime (ns)
0
1 10^7
2 10^7
3 10^7
4 10^7
5 10^7
0
100
200
300
400
500

Luminescence decay

Chirped pulse amplification and dual grating pulse compression [see Chapter 3, page 86] from a mode locked Nd:YAG laser (Coherent) seeding a Nd:YAG regenerative amplifier (Continuum) provided 532 nm excitation (10 ps FWHM, 10 Hz repetition rate). The luminescence was dispersed with a Spex 270M monochromator and detected with a PMT (Products for Research). The PMT signal was amplified and digitized with a digital oscilloscope (LeCroy) and recorded on a PC. The instrument response measured 15 ns FWHM.

Theory and Data Analysis

The semiclassical theory (see Chapter 1, Equation 1.7 and corresponding references) describes that rate of ET decays exponentially with distance, R, from the contact rate, k_o, and is scaled by the distance decay parameter, β.

Equation 4.1.
$$k_{ET} = \left(\frac{4\pi^3}{\hbar^2 \lambda k T} \right)^{1/2} H_{AB}^2 \exp\left(\frac{-(\Delta G + \lambda)^2}{4\lambda k T} \right)$$

The electronic-coupling matrix element, H_{AB}, gives rise to the exponential distance dependence.

Equation 4.2.
$$H_{AB} = H_{AB}^o \exp\left(-\frac{\beta R}{2} \right)$$

The model used here to describe ET in a system of randomly dispersed donor and acceptor molecules derives from one developed by Inokuti and Hirayama [16] for the case of exchange energy transfer. This model was later refined to account for the excluded volumes of the donor and acceptor (Equation 4.3) [54].

Equation 4.3. $$I(t) = I_{t=0} \exp\left(-\frac{t}{\tau_o} - A \cdot [Q] \cdot 3 \int_d^\infty \{1 - \exp[-tk_o \exp(-\beta(R-d))]\} R^2 dR \right)$$

Equation 4.3, which is valid in the [Q] < 5 M concentration regime, describes the luminescence decay, *I(t)*, in terms of the intensity at time zero ($I_{t=0}$), the lifetime in the absence of quencher (τ_o), the distance decay factor (β) and the ET rate at contact distance between donor and acceptor molecules (k_o) (A = 396.417). The function in the integrand describes the time dependent evolution of luminescence quenching by ET in a random distribution of acceptors around donor molecules where ET is governed by an exponential distance dependence. This model allows for excluded volumes to be considered by numerically integrating from d to R_{max}, where d is the distance between the centers of donor and acceptor at van der Waals contact and R_{max} is the maximum distance at which quenching occurs [54].

The function f(R,t) in the integrand of Equation 4.3 depends sharply on distance. Figure 4.5 shows the evolution of f(R,t) at four time points.

Equation 4.4. $$f(R,t) = [1 - \exp(-tk_o \exp[-\beta(R-d)])] R^2$$

Equation 4.3 is applicable if the following four assumptions are valid [16,54]. (1) The donor and acceptor molecules are randomly distributed. (2) Translational motion is slow with respect to ET. (3) The rate of ET is independent of molecular orientation and (4) has an exponential distance dependence. The dependence on molecular orientation is only significant on a time scale of less than a few hundred picoseconds [7].

Figure 4.5 The function f(R,t) (Equation 4.4) which is part of Equation 4.3 evaluated at various times, with constant values for k_o and β taken to be 1×10^{13} s^{-1} and 1.65 $Å^{-1}$, respectively.

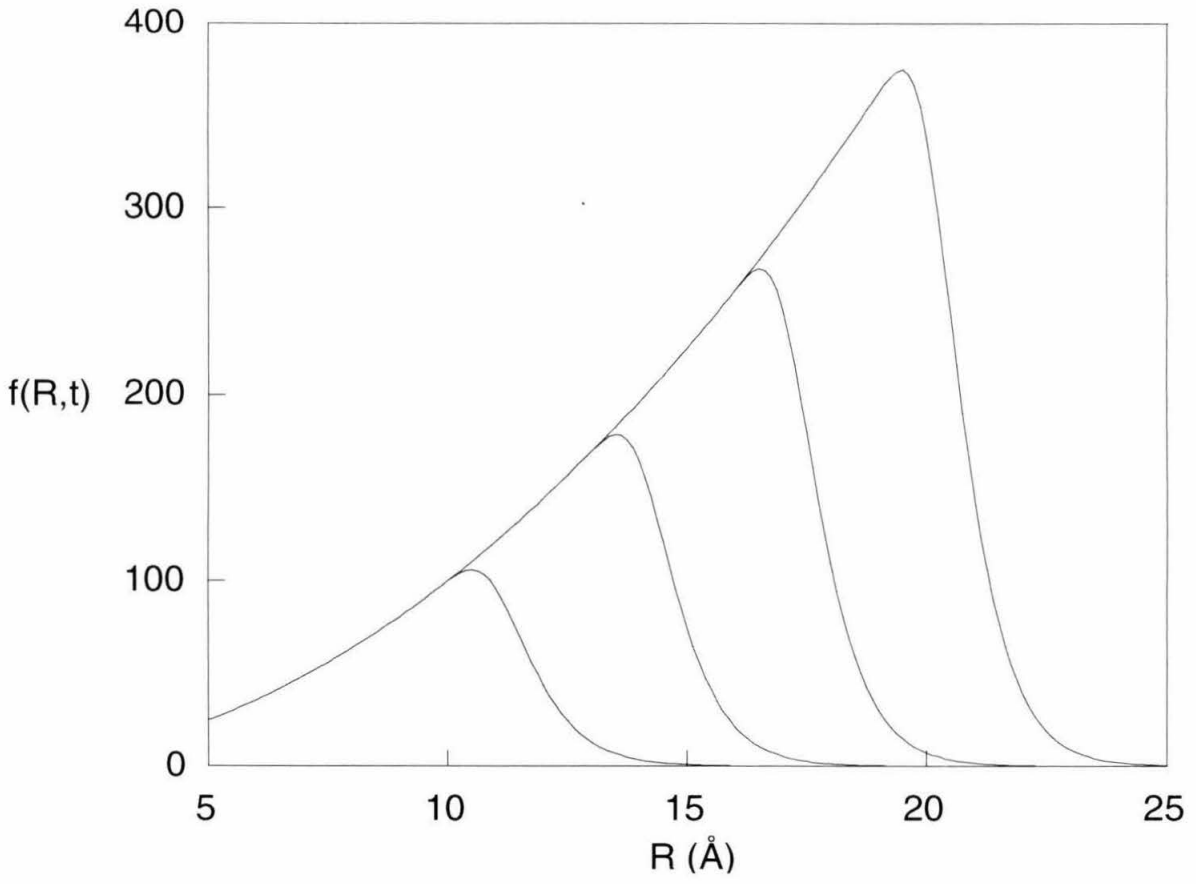
400
300
200
100
0
f(R,t)
5
10
15
20
25
R (Å)

The goal of this analysis is to determine the ET distance-decay factor, β, from a set of luminescence decay data that were measured as a function of quencher concentration. Equation 4.3 contains three unknown parameters—β, k_o, $I_{t=0}$. When luminescence decay data alone are fit to Equation 4.3 with three unknown parameters, then β and k_o are strongly correlated and a unique solution cannot be found. However, one unknown parameter, $I_{t=0}$, is effectively determined by independently measuring the relative luminescence quantum yield for the same set of samples.

The luminescence yield experiments are time-integrated measurements that provide an accurate account of the luminescence intensity. This additional information allows normalization of $I_{t=0}$ parameter in the luminescence decay data. Thus, the luminescence decay experiments combined with the luminescence yield experiments reduces the unknown parameter set to β and k_o. Specifically, the normalization of the luminescence decay data is accomplished if one considers, $A_{I(\lambda)}/A_{Io(\lambda)} = \alpha A_{I(t)}/A_{Io(t)}$, where α is the normalization factor and $A_{I(\lambda)}$, $A_{Io(\lambda)}$, $A_{I(t)}$, $A_{Io(t)}$ are numerical integrated areas of the luminescence yield with and without quencher, and the luminescence decay with and without quencher, respectively. Prior to this normalization, $A_{Io(t)}$ is set equal to τ_o by multiplying the $I_o(t)$ data by a corresponding factor. Finally, the normalized luminescence decays are fit to Equation 4.3 to obtain unique values for the ET parameters β and k_o.

Results and Discussion

The Beta of Water

Photoexcitation of $[Ru(tpy)_2]^{2+}$ embedded in 25% acid aqueous glasses at 77 K results in luminescence that is quenched by ET in the presence of Fe_{aq}^{3+}. Energy transfer quenching can be eliminated as a decay channel because the overlap of Fe_{aq}^{3+} absorption (λ_{max} = 715 nm, ε = < 0.01 $M^{-1}cm^{-1}$) [65] and $[Ru(tpy)_2]^{2+}$ luminescence (λ_{max} = 600 nm) is negligible. The concentration range of Fe_{aq}^{3+} used was 0.01-0.5 M and the glassing media were H_2O/25% H_2SO_4, H_2O/25% HSO_3F, and D_2O/25% D_2SO_4 at 77 K. The steady-state luminescence data used to determine the relative luminescence quantum yields are presented in Figure 4.6. Figures 4.7-4.9 shows integrated intensities obtained from luminescence yield experiments (Figure 4.6) plotted against the concentration of Fe^{3+} quencher. These data were used to normalize the luminescence decays in Figure 4.10.

In the absence of ferric ion quencher, the lifetime of $[Ru(tpy)_2]^{2+}$ is 8.0 μs in H_2O and 10.2 μs in D_2O at 77 K. In these excited-state ET experiments, a long lifetime is essential since ET occurs over a larger distance range for longer lifetimes. Consequently, longer lifetimes result in more reliable distance dependence information. The luminescence lifetimes of the excited-state donor are long enough (~10 μs) to allow a significant distance range (~25 Å) to be probed. The decays of the quencher-containing samples are nonexponential and were fit to Equation 4.3 using a least squares fitting routine (Figure 4.11-4.13). Table 4.1 shows the resulting parameters, β and k_o, from the best fits. The sensitivity of the fits on the value of β for a constant value of k_o are shown

in Figure 4.14, which shows the calculated decays for values of $\beta \pm 0.1$. The β value for the H_2O/25% H_2SO_4 system is 1.68 ± 0.03 $Å^{-1}$. Our experimental β value is in excellent agreement with the most recent *ab initio* calculations by Cave who reports a β-value range of 1.5-1.8 $Å^{-1}$ for water [21].

Deuterium Isotope Effects

The deuterium isotope effect of β (β_H/β_D = 1.03) is negligible. The absence of a deuterium isotope effect of β implies that the electronic coupling between water molecules is equivalent for H_2O and D_2O. There is, however, a pronounced isotope effect of k_H/k_D = 3.2. This observation is consistent with results from early investigations of Fe_{aq}^{2+}–Fe_{aq}^{3+} (k_H/k_D = 2) [55] and Cr_{aq}^{2+}–$[Co(NH_3)_5H_2O]^{3+}$ (k_H/k_D = 3.8) [56] exchange reactions in D_2O. One explanation for k_H/k_D isotope effects is nuclear tunneling (see Chapter 1, page 20). If nuclear tunneling has a large contribution to the rate of product formation, then the smaller O–D vibrational frequency will lead to a smaller Franck-Condon factor, and thus a slower rate constant.

The Role of the Sulfate Ion

A concern was that the sulfate ion from the sulfuric acid could mediate ET. In order to test this, we performed the experiments in H_2O/25% HSO_3F glassing medium. The ionization potential of fluorosulfate is much larger than that of sulfate ion. Thus, if ET were mediated by sulfate ion, we would expect a large effect in distance dependence (See Chapter 1, page 15). The fact that the β value is the same for both H_2O/25% H_2SO_4 and H_2O/25% HSO_3F indicates that the sulfate ion does not mediate ET.

Figure 4.6 Relative luminescence quantum yield data of $[Ru(tpy)_2]^{2+}$ in H_2O/H_2SO_4 (top), D_2O/D_2SO_4 (middle), and $H_2O/HFSO_3$ (bottom) with various Fe_{aq}^{3+} concentrations (0, 0.05, 0.1, 0.25, 0.5 M).

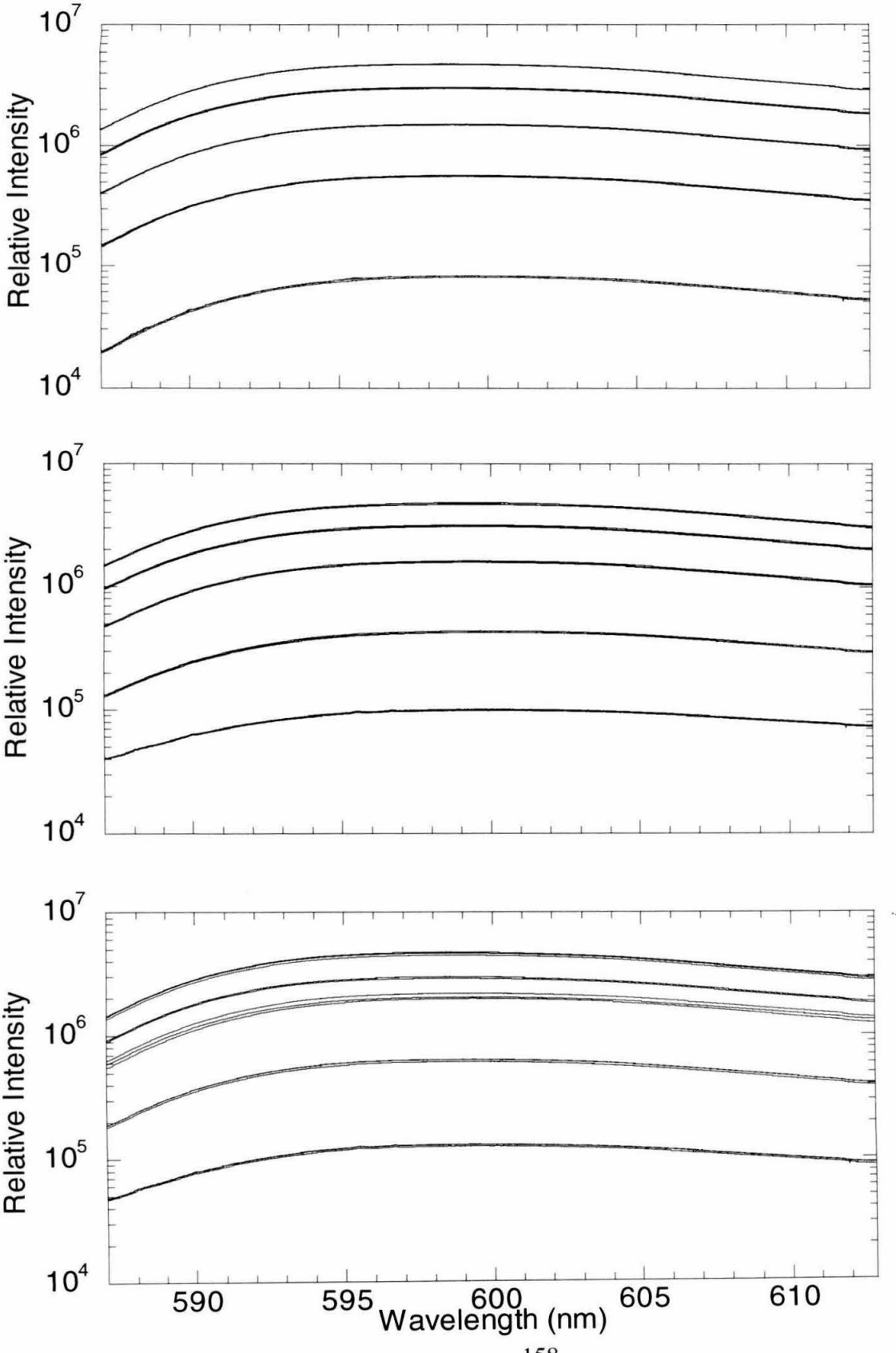
Relative Intensity
10^7
10^6
10^5
10^4
590
595
600
605
610
Wavelength (nm)

Figure 4.7 Semilogy plot of the integrated luminescence intensity of $[Ru(tpy)_2]^{2+}$ as a function of Fe^{3+} concentration in H_2O/25% H_2SO_4 glass at 77 K. The black line represents the best fit to an exponential function.

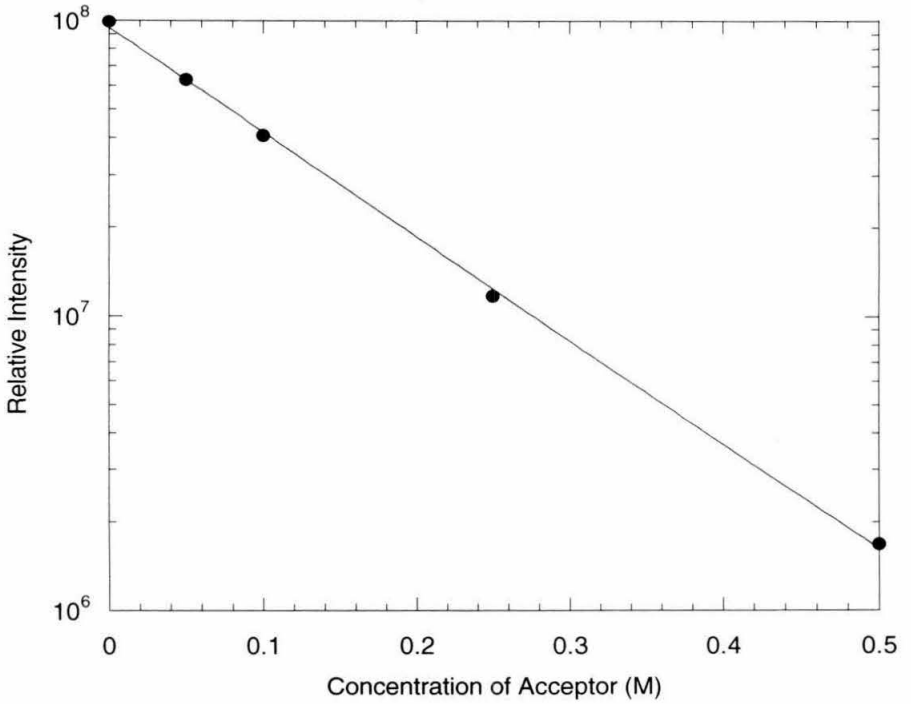
10^8
10^7
10^6
Relative Intensity
0
0.1
0.2
0.3
0.4
0.5
Concentration of Acceptor (M)

Figure 4.8 Semilogy plot of the integrated luminescence intensity of $[Ru(tpy)_2]^{2+}$ as a function of Fe^{3+} concentration in D_2O/25% D_2SO_4 glass at 77 K. The black line represents the best fit to an exponential function.

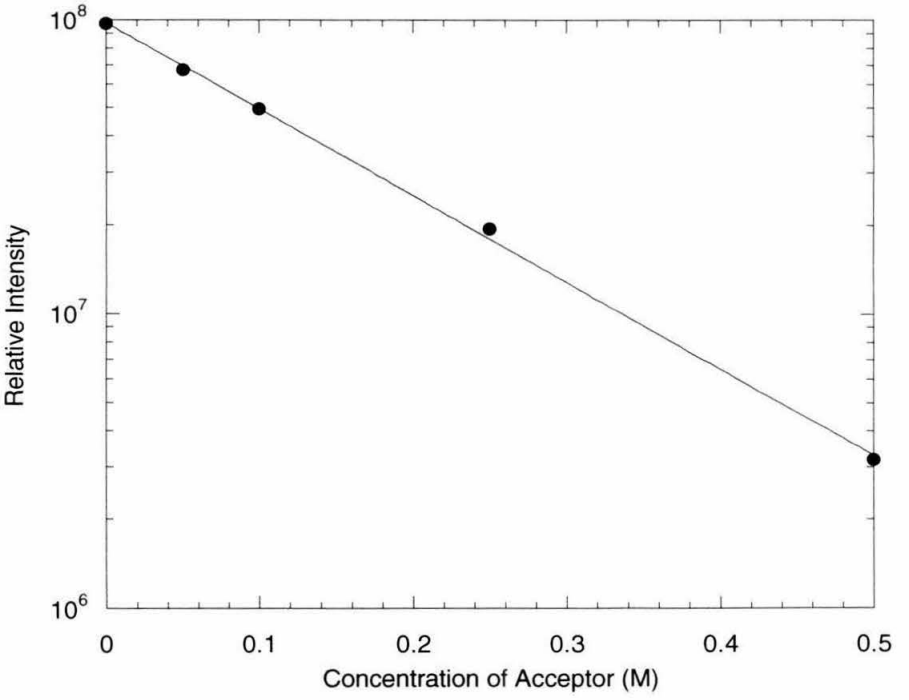
10^8
10^7
10^6
Relative Intensity
0
0.1
0.2
0.3
0.4
0.5
Concentration of Acceptor (M)

Figure 4.9 Semilogy plot of the integrated luminescence intensity of $[Ru(tpy)_2]^{2+}$ as a function of Fe^{3+} concentration in H_2O/25% $HFSO_3$ glass at 77 K. The black line represents the best fit to an exponential function.

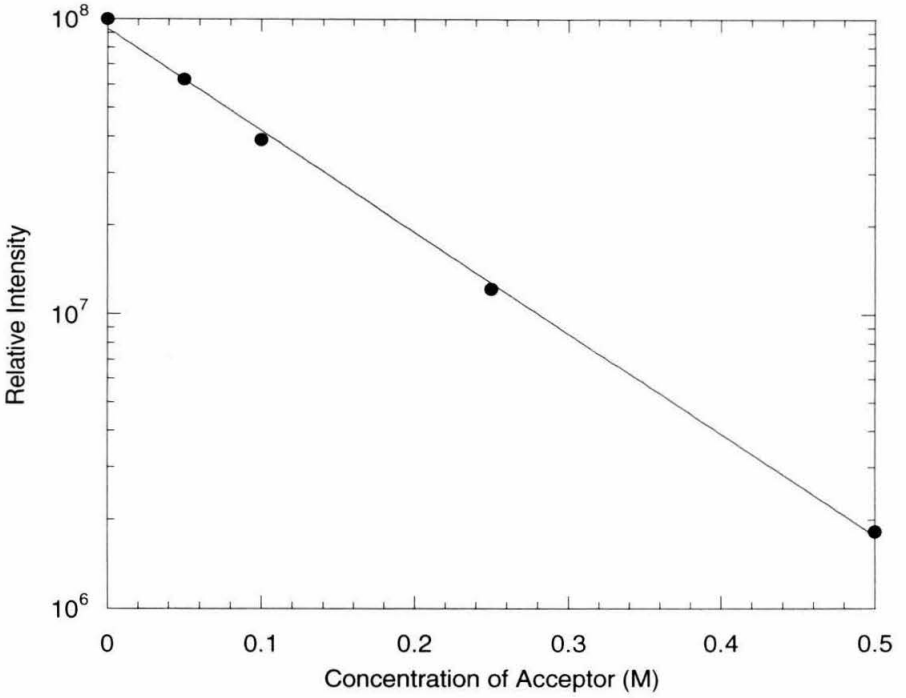
10^8
10^7
10^6
Relative Intensity
0
0.1
0.2
0.3
0.4
0.5
Concentration of Acceptor (M)

Figure 4.10 Normalized luminescence decay data of $[Ru(tpy)_2]^{2+}$ (τ_o = 8 μs) in H_2O/H_2SO_4 glass at 77 K. The concentrations of Fe_{aq}^{3+} quencher used are 0, 0.05, 0.1, 0.25, and 0.5 M.

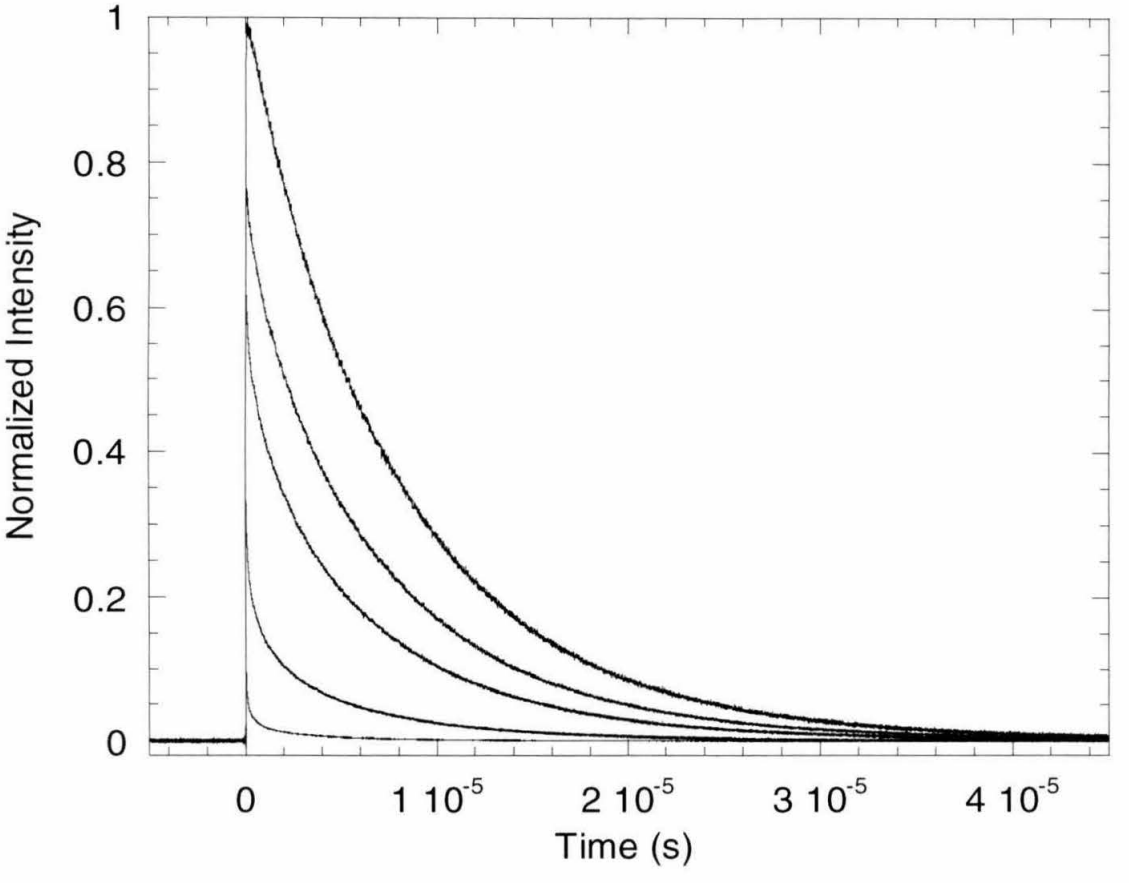
Normalized Intensity
1
0.8
0.6
0.4
0.2
0
0
1 10-5
2 10-5
3 10-5
4 10-5
Time (s)

Figure 4.11 Semilogx plot of the luminescence decays of $[Ru(tpy)_2]^{2+}$ for a range of Fe^{3+} concentration (0, 0.05, 0.1 0.25 and 0.5 M) in H_2O/25% H_2SO_4 glass at 77 K. The black lines are best fits to Equation 4.3. The averaged results from the fits for the four concentrations of the unknown parameters β and k_o are shown in Table 4.1.

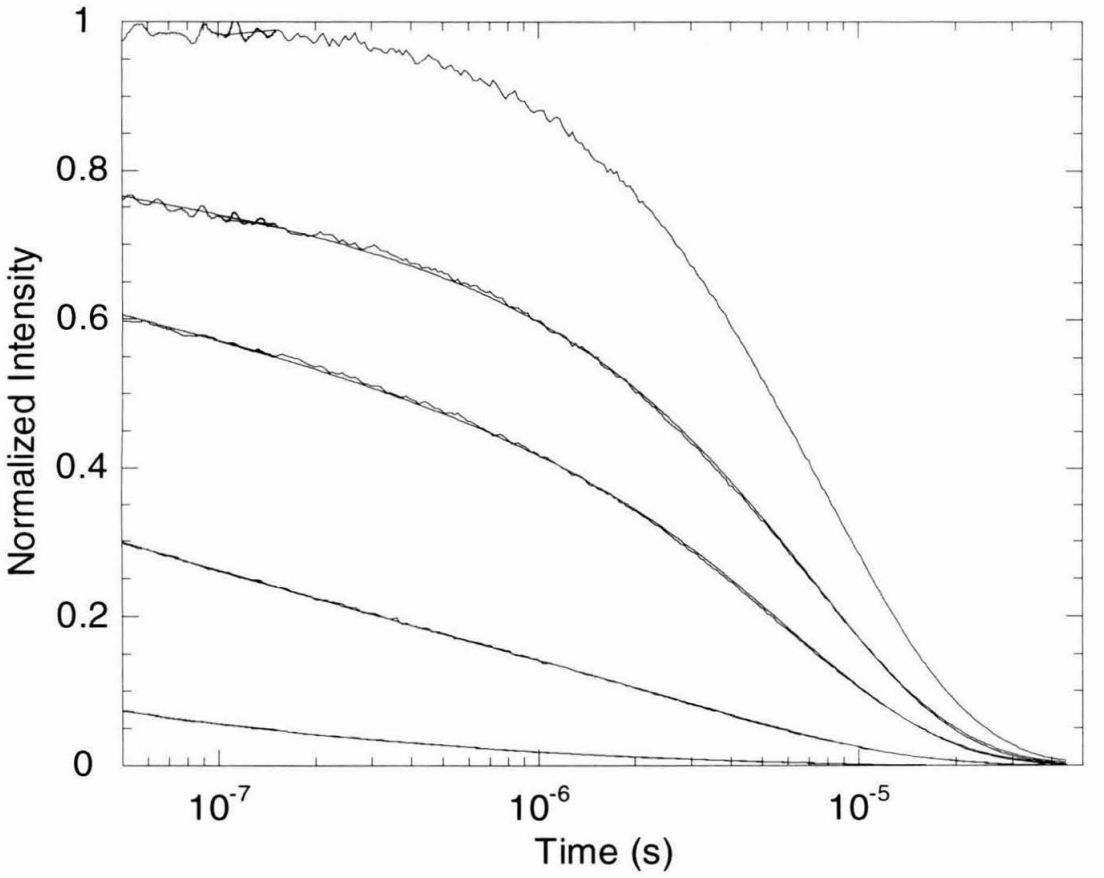
1
0.8
0.6
0.4
0.2
0
Normalized Intensity
10-7
10-6
10-5
Time (s)

Figure 4.12 Semilogx plot of the luminescence decays of $[Ru(tpy)_2]^{2+}$ for a range of Fe^{3+} concentration (0, 0.05, 0.1 0.25 and 0.5 M) in D_2O/25% D_2SO_4 glass at 77 K. The black lines are best fits to Equation 4.3. The averaged results from the fits for the four concentrations of the unknown parameters β and k_o are shown in Table 4.1.

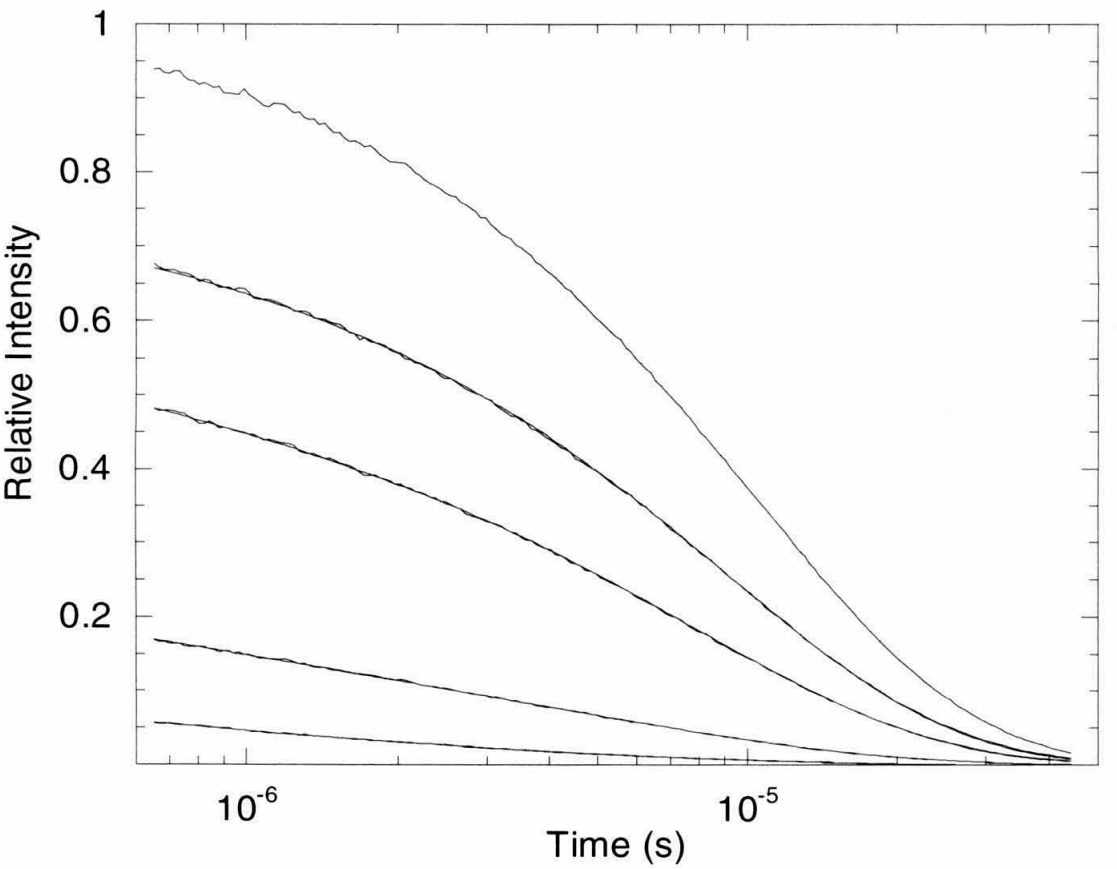
1
0.8
0.6
0.4
0.2
Relative Intensity
10-6
10-5
Time (s)

Figure 4.13 Semilogx plot of the luminescence decays of $[Ru(tpy)_2]^{2+}$ for a range of Fe^{3+} concentration (0, 0.05, 0.1 0.25 and 0.5 M) in H_2O/25% $HFSO_3$ glass at 77 K. The black lines are best fits to Equation 4.3. The averaged results from the fits for the four concentrations of the unknown parameters β and k_o are shown in Table 4.1.

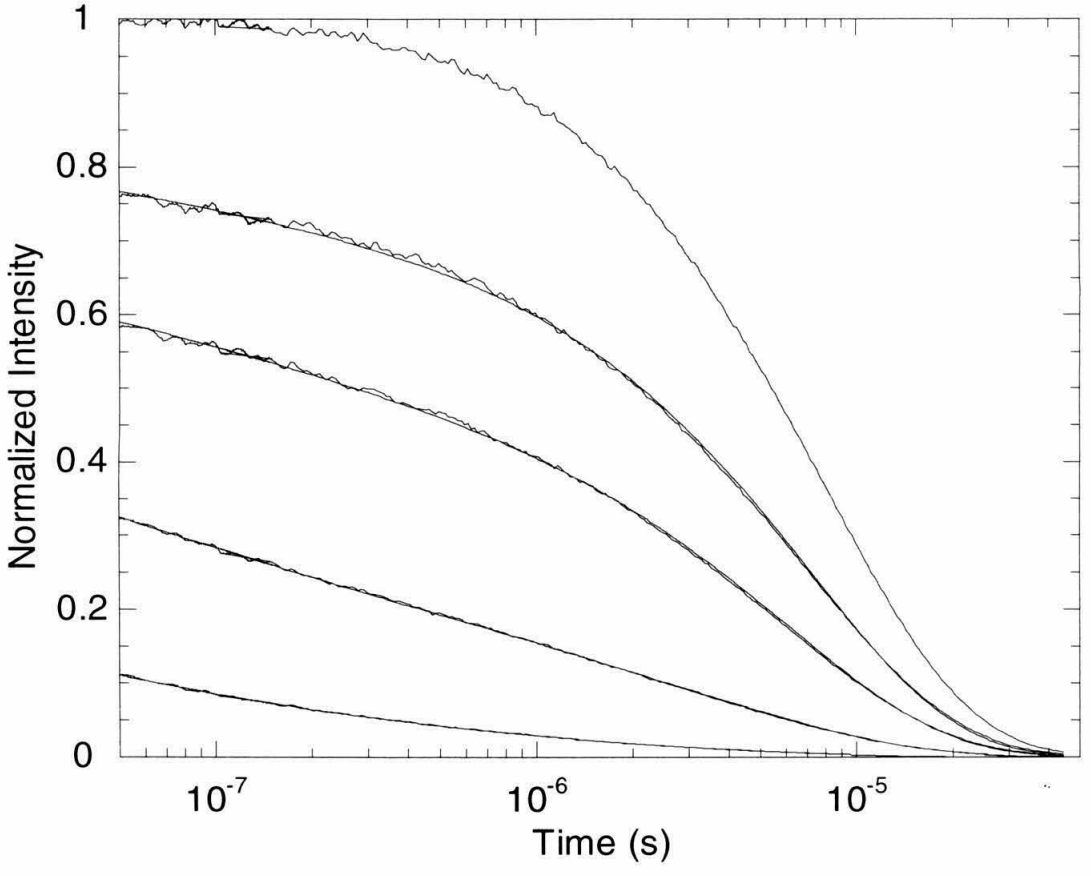
1
0.8
0.6
0.4
0.2
0
Normalized Intensity
10-7
10-6
10-5
Time (s)

Figure 4.14 Simulated kinetics traces illustrating sensitivity to the β parameter. The traces were calculated from Equation 4.3 using the same concentrations used in the experiments (0.05-0.5 M) and a k_o value of 1×10^{13} s^{-1}. The solid trace represent a β value of 1.65 $Å^{-1}$, while the corresponding upper and lower dashed traces represent β values of 1.75 and 1.55 $Å^{-1}$, respectively.

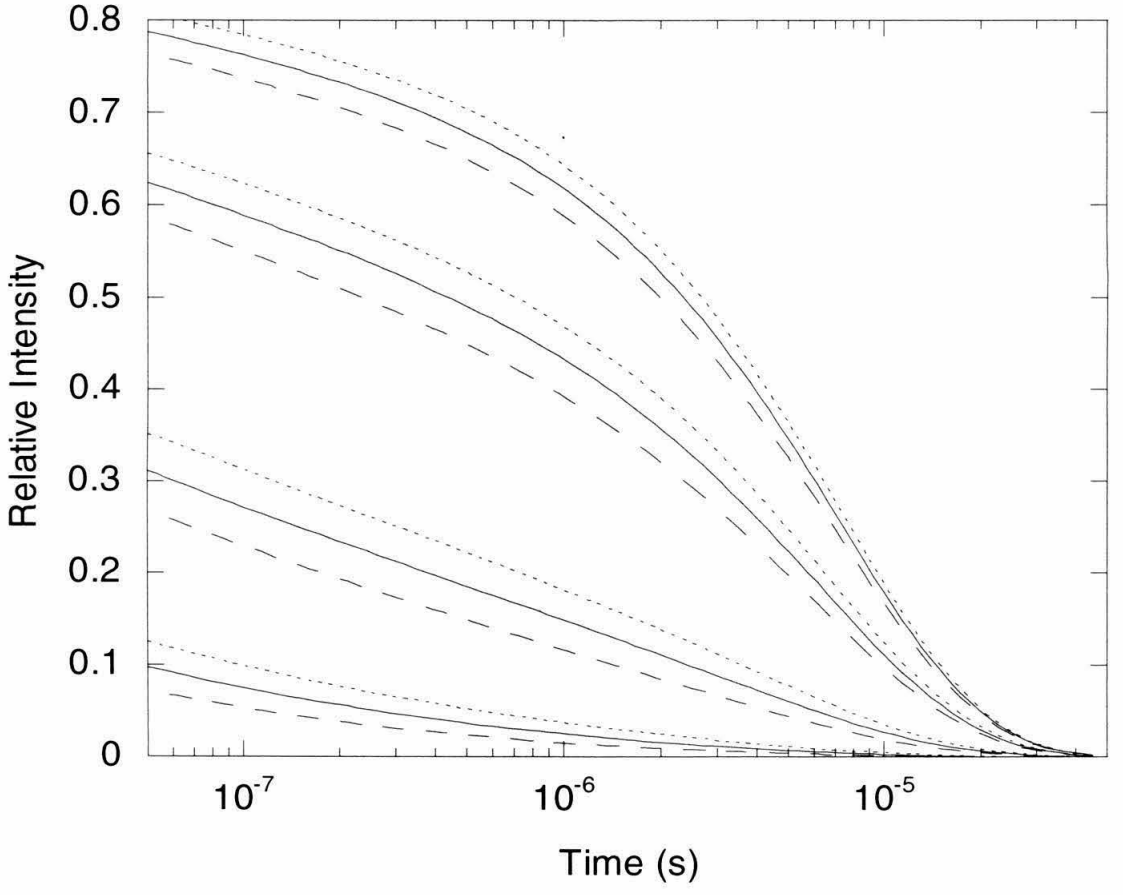
0.8
0.7
0.6
0.5
0.4
0.3
0.2
0.1
0
Relative Intensity
10-7
10-6
10-5
Time (s)

Table 4.1 Parameters, β and k_o, obtained from best fits of normalized luminescence decay data to quenching model (Equation 4.4) for various concentrations of Fe_{aq}^{3+} acceptor.

Bridging Medium	β_{avrg} ($Å^{-1}$)	$k_{o\ avrg}$ (s^{-1})	[Fe_{aq}^{3+}] (M)	β ($Å^{-1}$)	k_o (s^{-1})
H_2O / 25% H_2SO_4	1.68 ± 0.03	$5.7\times10^{12} \pm 2.4\times10^{12}$	0.05	1.70	8.5×10^{12}
			0.10	1.67	4.4×10^{12}
			0.25	1.65	3.2×10^{12}
			0.50	1.71	6.8×10^{12}
D_2O / 25% D_2SO_4	1.63 ± 0.02	$1.8\times10^{12} \pm 1.1\times10^{12}$	0.05	1.64	2.3×10^{12}
			0.10	1.61	1.7×10^{12}
			0.25	1.65	2.9×10^{12}
			0.50	1.62	3.9×10^{12}
H_2O / 25% HSO_3F	1.64 ± 0.03	$3.9\times10^{12} \pm 2.7\times10^{12}$	0.05	1.67	6.1×10^{12}
			0.10	1.67	6.4×10^{12}
			0.25	1.61	1.5×10^{12}
			0.50	1.62	1.5×10^{12}

Water in Protein-ET Pathways

ET between redox sites in proteins is mediated by the most efficient tunneling pathways. Considering that water is contained within and surrounds proteins, it is relevant to question the interplay of water and the protein matrix in mediating ET. To answer this question, the relative efficiencies of protein matrix *vs.* water mediated ET must be known. While protein ET has been measured for many different systems (Figure 4.15) [57], only a few pulse-radiolysis measurements have been performed in aqueous glasses [5,6,10].

The β values obtained for water with pulse-radiolysis measurements (0.5-1.0 $Å^{-1}$) [9,10] are lower than those of covalent paths in protein matrices (1.1-1.5 $Å^{-1}$) [57]. Thus, the pulse-radiolysis experiments predict that electronic coupling through water is better than through the protein matrix. Our photoinduced ET results, however, indicate (Figure 4.15) that the ET rate through water will be much slower than the rate of ET in a protein matrix. Thus, according to our results, ET will proceed most efficiently through direct covalent pathways, rather than water. Nonetheless, the most efficient tunneling pathway might include water structures rather than a circuitous covalent route. For example, the efficiency of a pathway in which a water molecule bridges a 3.5 Å gap would be equivalent to a 5.2 Å covalent path, assuming a β of 1.68 $Å^{-1}$ for the water-bridged gap and 1.1 $Å^{-1}$ for the covalent path.

This difference in distance dependence obtained from pulse-radiolysis and photoinduced measurements is consistent with the tunneling energy gap dependence predicted by superexchange models [58]. These models predict that as the energy gap

Figure 4.15 Plot of $\log(k_{ET})$ *vs.* direct D–A distance (R) illustrating differential electronic coupling through water *vs.* through a variety of proteins. Water-mediated ET is slower than any of the protein-mediated ET data. The protein data have been previously compiled [57], with the exception of the HiPIP data which are compiled in Chapter 3.

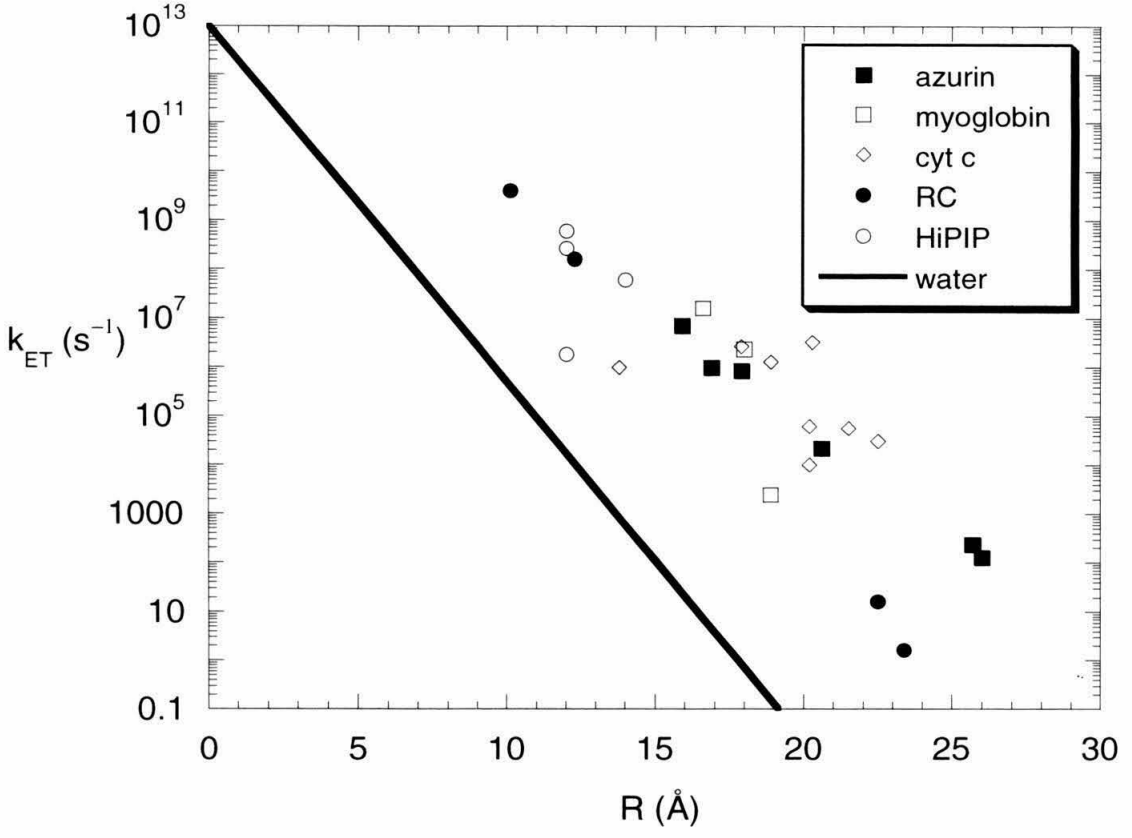
10^{13}
10^{11}
10^{9}
10^{7}
10^{5}
1000
10
0.1
k_{ET} (s^{-1})
0
5
10
15
20
25
30
R (Å)
azurin
myoglobin
cyt c
RC
HiPIP
water

between the mediating bridge state and the tunneling electron becomes smaller, the β value decreases. The energy gap between a solvated electron and the mediating bridge state is 2 eV, while that of the excited state of $[Ru(bpy)_3]^{2+}$ is 3.6 eV (Figure 4.3). A few experimental papers have analyzed ET data in terms of tunneling energy gap dependence [59,60]. However, recent calculations by Dr. Jay Winkler indicate that thermal population of the bridge states will lead to a hopping mechanism before the tunneling energy gap dependence becomes observable.

A more plausible explanation for the difference in β for the two types of experiments is that the distribution of trap-depths for the solvated electrons could lead to an alternate, electron-hopping mechanism. The distribution in trap-depths gives rise to broad optical absorption spectra that have a FWHM of ~ 1 eV [10]. The assignment of a trap-depth distribution of 1 eV is corroborated by a blue-shifting absorption maximum with time, which indicates a deeping of the trap-depths as the solvent stabilizes the solvated electron [61-63]. A solvated electron in a trap is surrounded by more traps, some of which are lower in energy. These lower energy traps can serve as electron hopping intermediates. Consequently, the distance dependence obtained from pulse radiolysis experiments might not be due to a pure electron tunneling mechanism and a β value for extracted from these studies are open to question.

Conclusions

In this work, we investigated the distance dependence of ET through a water solvent system and thus quantified the efficiency of water mediated electronic coupling.

The distance decay factor for ET mediated *via* water bridges was determined to be 1.68 $Å^{-1}$ by analysis of luminescence decays and quantum yield data.

References

[1] MV Ponamrev, WA Cramer, *Biochem.*, **37**, 17199 (1998).

[2] IM Klotz, J Ayers, JYC Ho, MG Horowitz and R.E. Heiney, *J. Am. Chem. Soc.*, **80**, 2132 (1958).

[3] RA Horne, *J. Inorg. Nucl. Chem.*, **25**, 1139 (1963).

[4] E Nitzan, AC Wahl, *J. Inorg. Nucl. Chem,* **28**, 3069 (1966).

[5] JR Miller, *Chem. Phys. Lett.*, **22**, 180-182 (1973).

[6] JR Miller, *J. Phys. Chem.*, **79**, 1070-1078 (1975).

[7] K Weidenmeaier, HL Tavernier, SF Swallen, MD Fayer, *J. Phys. Chem. A,* **101**, 1887-1902 (1997).

[8] CF Shannon, DD Eads, *J. Chem. Phys.*, **103**, 5208-5223 (1995).

[9] JR Miller, personal communication (1998).

[10] RF Khairutdinov, KI Zamaraev, VP Zhdanov, In Electron Tunneling in Chemistry, RG Compton, Ed., Elsevier, Amsterdam (1989).

[11] KH Schmidt, P Han, DM Bartels,*J. Phys. Chem.* **99**, 10530-10539 (1995)

[12] K Kumar, Z Lin, DH Waldeck, MB Zimmt, *J. Am. Chem. Soc.*, **118**, 243 (1996).

[13] AM Oliver, DC Craid, MN Padden-Row, J Kroon, JW Verhoeven, *Chem. Phys. Lett.*, **150**, 366 (1988).

[14] JM Lawson, MN Paddon-Row, W Schuddeboom, JM Warman, AH Clayton, KP Ghiggino, *J. Phys. Chem.*, **97**, 13099 (1993).

[15] S Strauch, G McLendon, M McGuire, T Guarr, *J. Phys. Chem.*, **87**, 3579 (1983).

[16] M Inokuti, F. Hirayama, *J. Chem. Phys.*, **43**, 1978 (1965).

[17] SJ Larsson, *J. Phys. Chem.* **88**, 1321-1323 (1984).

[18] HM McConnell, *J. Chem. Phys.*, **33**, 115-121 (1960).

[19] MD Newton, *J. Electroanal. Chem.*, **438**, 3-10 (1997).

[20] MD Newton, personal communication (1999).

[21] NE Miller, MC Wander, RJ Cave,*J. Phys Chem. A,* **103**, 1084-1093 (1999).

[22] H Oevering, MN Paddon-Row, M Heppener, AM Oliver, E Cotsaris, JW Verhoeven, NS Hush, *J. Am. Chem. Soc.*, **109**, 3258-3269 (1987).

[23] MD Johnson, JR Miller, NS Green, GL Closs, *J. Phys. Chem.*, **93**, 1173-1176 (1989).

[24] A Helms, D Heiler, G McLendon, *J. Am. Chem. Soc.*, **114**, 6227-6238 (1992).

[25] AP Ribou, JP Launay, K Takahashi, T Nihira, S Tarutani, CW Spangler, *Inorg. Chem.*, **33**, 1325-1329 (1994).

[26] JR Winkler, HB Gray,*Chem. Rev.*, 369-379., (1992).

[27] CC Moser, JM Keske, K Warncke, RS Farid, PL Dutton, *Nature*, **355**, 796-802 (1992).

[28] FD Lewis, TF Wu, YF Zhang, RL Letsinger, SR Greenfield, MR Wasielewski, *Science*, 673-676 (1997).

[29] JR Miller, JA Peeples, MJ Schmitt, GL Closs, *J. Am. Chem. Soc.*, **104**, 6488 (1982).

[30] T Guarr, ME McGuire, G McLendon, *J. Am. Chem. Soc.*, **107**, 5104 (1985).

[31] TJ Meyer, *Inorg. Chem.*, **19**, 1405 (1980).

[32] H Rawson, in *Inorganic Glass-Forming Systems*, Academic Press, New York (1967).

[33] RA Marcus, *J. Chem. Phys.*, **24**, 966 (1956).

[34] RA Marcus, *Annu. Rev. Phys. Chem.*, **15**, 155 (1964).

[35] RA Marcus, *Rev. Mod. Phys.*, **65**, 599 (1993).

[36] P Chen, E Danielson, TJ Meyer, *J. Phys. Chem.*, **92**, 3708 (1988).

[37] WJ Jones, P Chen, TJ Meyer, *J. Am. Chem. Soc.*, **114**, 387 (1992).

[38] GL Gaines, MP O'Neil, WA Svec, MP Niemczyk, MR Wasielewski, *J. Am. Chem. Soc.*, **113**, 719 (1991).

[39] MR Wasielewski, DG Johnson, WA Svec, KM Kersey, DW Minsek, *J. Am. Chem. Soc.*, **110**, 7219 (1988).

[40] A Bernas, C Ferradini, J-P Jay-Gerin, *Chem. Phys.*, **222**, 151-160 (1997).

[41] JV Coe, AD Earhart, MH Cohen, GJ Hoffman, HW Sarkas, KH Bowen, *J. Chem. Phys.*, **107**, 6023-6031 (1997).

[42] AJ Frank, M Gratzel, A Henglein, *Ber. Bunsenges. Phys. Chem.*, **80**, 593 (1976).

[43] I Watanabe, JB Flanagan, P Delahay, *J. Chem. Phys.*, **73**, 2057 (1980).

[44] T Watanabe, H Gerischer, *J. Electroanal. Chem.*, **122**, 73 (1981).

[45] P. Delahay, K von Burg,*Chem. Phys. Lett.*, **83**, 250 (1981).

[46] P Delahay, *Acc. Chem. Res.*, **15**, 40 (1982).

[47] D Grand, A Bernas, E Amouyal, *Chem. Phys.*, **44**, 73 (1979).

[48] D Grand, A Bernas, E Amouyal, *J. Phys. Chem.*, **84**, 1259 (1980).

[49] E Amouyal, D Grand, A Bernas, *Photochem. Photobiol.*, **29**, 1071 (1979).

[50] M Michaud, P Cloutier, L Sanche, *Phys. Rev. A*, **44**, 5624 (1991).

[51] G Pastori Parravicini, L Resca, *Phys. Rev B*, **8**,3009 (1973).

[52] VF Petrenko, IA Ryzhkin, *Phys. Rev. Lett.*, **71**, 2626 (1993).

[53] K Kobayashi, *J. Phys. Chem.*, **87**, 4317 (1983).

[54] A Blumen, *J. Chem. Phys.*, **72**, 2632 (1980).

[55] J Hudis, RW Dodson, *J. AM. Chem. Soc.*, **78**, 911 (1956).

[56] A Zwickel, H Taube, *J. Am. Chem. Soc.*, **81**, 1288 (1959).

[57] HB Gray, JR Winkler,*Annu. Rev. Biochem.*, **65**, 537-561 (1996).

[58] MD Newton, *Adv. Chem. Phys.*, **106**, 303-375 (1999).

[59] VV Krongauz, *J. Phys. Chem.*, **96**, 2609 (1992).

[60] WB Davies, WA Svec, MA Ratner, MR Wasielewski,*Nature*, **396**, 60-63 (1998).

[61] DC Walker,*J. Phys. Chem.*, **84**, 1140 (1980).

[62] JR Miller, BE Cliffs, JJ Hines, RF Runowski, KW Johnson, *J. Phys. Chem.*, **80**, 457 (1976).

[63] JX Baxendale, PHG Sharpe, *Int. J. Radiat. Phys. Chem*, **8**, 621 (1979).

[64] H Reiss, A Heller, *J. Phys. Chem.*, **89**, 4207-4213 (1985).

[65] SM Nelson, in *Comprehensive Coord. Chem.*, p219, G Wilkinson Ed., Pergamon` Press, New York (1987).

Appendix

MATLAB Data Analysis Program

```
date=input('What is the date of your data?  ');
fprintf('...loading S-S data...\n');
p1=['load ''d:\work\',date,'\Qy\D\0_1.prn'''];
p2=['load ''d:\work\',date,'\Qy\D\0_2.prn'''];
p3=['load ''d:\work\',date,'\Qy\D\0_3.prn'''];
p4=['load ''d:\work\',date,'\Qy\D\1_1.prn'''];
p5=['load ''d:\work\',date,'\Qy\D\1_2.prn'''];
p6=['load ''d:\work\',date,'\Qy\D\1_3.prn'''];
p7=['load ''d:\work\',date,'\Qy\D\2_1.prn'''];
p8=['load ''d:\work\',date,'\Qy\D\2_2.prn'''];
p9=['load ''d:\work\',date,'\Qy\D\2_3.prn'''];
p10=['load ''d:\work\',date,'\Qy\D\3_1.prn'''];
p11=['load ''d:\work\',date,'\Qy\D\3_2.prn'''];
p12=['load ''d:\work\',date,'\Qy\D\3_3.prn'''];
p13=['load ''d:\work\',date,'\Qy\D\4_1.prn'''];
p14=['load ''d:\work\',date,'\Qy\D\4_2.prn'''];
p15=['load ''d:\work\',date,'\Qy\D\4_3.prn'''];
p16=['load ''d:\work\',date,'\Qy\D\bg_1.prn'''];
p17=['load ''d:\work\',date,'\Qy\D\bg_2.prn'''];
p18=['load ''d:\work\',date,'\Qy\D\bg_3.prn'''];
eval(p1);
eval(p2);
eval(p3);
eval(p4);
eval(p5);
eval(p6);
eval(p7);
eval(p8);
eval(p9);
eval(p10);
eval(p11);
eval(p12);
eval(p13);
eval(p14);
eval(p15);
eval(p16);
eval(p17);
eval(p18);
X0=((X0_1(:,2)-bg_1(:,2))+(X0_2(:,2)-bg_2(:,2))+(X0_3(:,2)-
bg_3(:,2))).*3;
X1=((X1_1(:,2)-bg_1(:,2))+(X1_2(:,2)-bg_2(:,2))+(X1_3(:,2)-
bg_3(:,2))).*3;
X2=((X2_1(:,2)-bg_1(:,2))+(X2_2(:,2)-bg_2(:,2))+(X2_3(:,2)-
bg_3(:,2))).*3;
```

```
X3=((X3_1(:,2)-bg_1(:,2))+(X3_2(:,2)-bg_2(:,2))+(X3_3(:,2)-
bg_3(:,2))).*3;
X4=((X4_1(:,2)-bg_1(:,2))+(X4_2(:,2)-bg_2(:,2))+(X4_3(:,2)-
bg_3(:,2))).*3;
A0=sum(X0);
A1=sum(X1);
A2=sum(X2);
A3=sum(X3);
A4=sum(X4);
R(1)=A1./A0;
R(2)=A2./A0;
R(3)=A3./A0;
R(4)=A4./A0;
x=X0_1(:,1);
clear X0_1 X0_2 X0_3 X1_1 X1_2 X1_3 X2_1 X2_2 X2_3 X3_1 X3_2
X3_3 X4_1 X4_2 X4_3 bg_1 bg_2 bg_3 X0 X1 X2 X3 X4 A0 A1 A2
A3 x;
global Ycfit Yavrg
fprintf('...loading kinetics data...\n');
p0=['load ''d:\work\4Aug98\kin\D\kin'''];
eval(p0);
tau=input('what''s the lifetime?  ');
fprintf('...normalizing data...\n');
y0=-K0+Kbg;
y1=-K1+Kbg;
y2=-K2+Kbg;
y3=-K3+Kbg;
y4=-K4+Kbg;
clear K0 K1 K2 K3 K4 Kbg;
offset0=sum(y0(1:8500))./8500;
offset1=sum(y1(1:8500))./8500;
offset2=sum(y2(1:8500))./8500;
offset3=sum(y3(1:8500))./8500;
offset4=sum(y4(1:8500))./8500;
y0=y0-offset0;
y1=y1-offset1;
y2=y2-offset2;
y3=y3-offset3;
y4=y4-offset4;
A0=(sum(y0)).*5e-10;
A1=(sum(y1)).*5e-10;
A2=(sum(y2)).*5e-10;
A3=(sum(y3)).*5e-10;
A4=(sum(y4)).*5e-10;
Rk1=A1./tau;
Rk2=A2./tau;
Rk3=A3./tau;
Rk4=A4./tau;
alpha(1)=tau./A0;
alpha(2)=R(1)./Rk1;
```

```
alpha(3)=R(2)./Rk2;
alpha(4)=R(3)./Rk3;
alpha(5)=R(4)./Rk4;
y0=y0.*alpha(1);
y1=y1.*alpha(2);
y2=y2.*alpha(3);
y3=y3.*alpha(4);
y4=y4.*alpha(5);
fprintf('...finding time zero...\n');
[del,x0]=delta(tau,y0);
for i=1:length(x0);
   if x0(i)>0;
   break
   end
end
len=length(x0);
x0=x0(i+100:len);
y0=y0(i+100:len);
y1=y1(i+100:len);
y2=y2(i+100:len);
y3=y3(i+100:len);
y4=y4(i+100:len);
fprintf('...compressing data...\n');
[xc0,yc0,yc1,yc2,yc3,yc4]=compress(x0,y0,y1,y2,y3,y4);
len1=length(xc0);
xc0=xc0(2:len1);
yc0=yc0(2:len1);
yc1=yc1(2:len1);
yc2=yc2(2:len1);
yc3=yc3(2:len1);
yc4=yc4(2:len1);
len2=length(xc0);
xfin0(1:len2)=xc0;
yfin0(1:len2)=yc0;
yfin1(1:len2)=yc1;
yfin2(1:len2)=yc2;
yfin3(1:len2)=yc3;
yfin4(1:len2)=yc4;
conc=[0.05 0.1 0.25 0.5];
beta=1.69;
ko=4.0752e15;
pram0=[beta,ko];
clear y0 y1 y2 y3 y4 x0;
fprintf('...fitting data...\n');
Y(:,1)=yfin1';
Y(:,2)=yfin2';
Y(:,3)=yfin3';
Y(:,4)=yfin4';
Y(:,5)=yfin0';
options(1)=1;
```

```
options(14)=35;
t=1e-7:1e-7:1e-5;
for f=1:4;
   pr(f,:)=fmins('IHB3',pram0,options,[],tau,conc(:,f),xfin0
,Y(:,f));
   Yfit(:,f)=Ycfit;
end
len3=length(xfin0);
semilogx(xfin0,Y(:,1),'r',xfin0,Y(:,2),'r',xfin0,Y(:,3),'r',
xfin0,Y(:,4),'r',xfin0,Y(:,5),'r',xfin0(1:len3),Yfit(:,1),'k
-',xfin0(1:len3),Yfit(:,2),'k-',xfin0(1:len3),Yfit(:,3),'k-
',xfin0(1:len3),Yfit(:,4),'k-')
pr
```

```
function [del,x0]=delta(tau,y0);

[a,b]=max(y0);
y0=y0(b+1000:100002,:);
len=length(y0);
x=5e-10:5e-10:50.001e-6;
x=x';
x1=x(1:len,:);
fx=exp(-x1./tau);
yi=sum(y0);
fi=sum(fx);
del=tau*(log(yi/fi));
xdel=x1-del;
x0=x-(x(b+935)+del);
```

```
function[xnew,ynew0,ynew1,ynew2,ynew3,ynew4]=compress(x0,y0,
y1,y2,y3,y4)
xref=-6.2:0.005:-4.35;
xref=10.^(xref);
maxcnt=length(x0);
xnew=zeros(1,fix((length(xref))./2));
ynew0=zeros(1,fix((length(xref))./2));
ynew1=zeros(1,fix((length(xref))./2));
ynew2=zeros(1,fix((length(xref))./2));
ynew3=zeros(1,fix((length(xref))./2));
ynew4=zeros(1,fix((length(xref))./2));
jcnt=1;
cnt=1;
for a=2:2:length(xref)-1;
   icnt=0;
   while ((x0(cnt)<=xref(a+1))&(cnt<maxcnt))
      xnew(jcnt)=xnew(jcnt)+x0(cnt);
      ynew0(jcnt)=ynew0(jcnt)+y0(cnt);
      ynew1(jcnt)=ynew1(jcnt)+y1(cnt);
      ynew2(jcnt)=ynew2(jcnt)+y2(cnt);
     ynew3(jcnt)=ynew3(jcnt)+y3(cnt);
      ynew4(jcnt)=ynew4(jcnt)+y4(cnt);
```

```
      cnt=cnt+1;
       cnt=min(maxcnt,cnt);
       icnt=icnt+1;
    end
    xnew(jcnt)=xnew(jcnt)./(icnt);
    ynew0(jcnt)=ynew0(jcnt)./(icnt);
    ynew1(jcnt)=ynew1(jcnt)./(icnt);
    ynew2(jcnt)=ynew2(jcnt)./(icnt);
   ynew3(jcnt)=ynew3(jcnt)./(icnt);
    ynew4(jcnt)=ynew4(jcnt)./(icnt);
   jcnt=jcnt+1;
end
```

```
function chisqr=IHB3(p,tau,conc,t,Y)
global Ycfit Yavrg
m=396.417;
lent=length(t);
beta=p(1);
ko=p(2);
d=5;
Rmax=25;
R=d:Rmax./100:Rmax+d;
y=beta.*R;
kdo=ko.*exp(-beta.*d);
for i=1:lent
   f=(1-exp(-t(i).*kdo.*exp(beta.*d).*exp(-y))).*y.^2;
  A(i)=trapz(y,f);
end
g=3.*A;
phi=conc.*(beta.^-3).*g./m;
I=exp(-t./tau-phi);
I=I';
lenI=length(I);
Ycfit=I(1:lenI);
Y1fit=Y(1:lenI);
Yexp(:,1)=Y1fit;
chisqr=(Yexp-Ycfit)'*(Yexp-Ycfit);
```

Chapter 5

Excited-State Dynamics of Ruthenium-Modified Amino Acids

Abstract

The pH dependent photophysical properties of a series of polypyridyl ruthenium substituted amino acids ([$Ru(bpy)_2$(bpy-CONH-AA)], where bpy = 2,2'-bipyridine, CONH is an amide linkage, and AA are the attached amino acids in dapa (**1**), daba (**2**), orn (**3**), and lys (**4**)) were investigated by steady-state and time-resolved luminescence spectroscopy. Due to negligible electronic interactions between the ruthenium chromophore and the amino acid moieties, the absorption spectra of **1-4** do not change as a function of pH (within detection limits). The luminescence lifetimes of these complexes, however, show a marked dependence on pH. At low pH (< 2), quenching *via* excited state protonation of the amide link leads to short lifetimes (τ = 65 ns). In the pH 2-8 range, the lifetime (τ = 337-427 ns) depends on the side-chain length of the amino acid in the complex. At high pH (> 9), lifetimes (τ = 430 ns) approach that of $[Ru(bpy)_3]^{2+}$, suggesting that the amino acid moiety has a negligible effect on nonradiative pathways of the ruthenium excited state.

Introduction

The unique photophysical properties of polypyridyl ruthenium complexes have generated an increasing interest in the application of these complexes structure/function sensors in the chemistry of biological macromolecules [1-12]. Their use as spectroscopic and mechanistic probes for protein [1] and DNA structures [2,3] is well established. Recent developments involving proteins as target sites include the molecular recognition of $[Ru(bpy)_3]^{2+}$ and $[Ru(phen)_3]^{2+}$ derivatives by a monoclonal antibody [4] and ruthenium modified proteins as anisotropy probes for solution dynamics and immunoassays of

antigens [5]. In the latter work, amino acid side chains have been selectively labeled with $[Ru(bpy)_3]^{2+}$ complexes. This approach has also been successfully used for the construction of several redox active peptides [6] and proteins [7-9]. Further applications, such as labeling of transition metal pharmaceuticals with amino acids [10,11] or probing substrate-surface interactions in peptide modified monolayers [12] may be envisioned. These examples illustrate the potential of metal-modified biological systems as powerful tools for structural and mechanistic studies.

An important feature of these applications is the response of the photophysical properties of ruthenium chromophores to changing conditions of the microenvironment provided by biological macromolecules. It is therefore of fundamental interest to study the mechanisms that perturb the photophysical properties in detail. This understanding is necessary in order to fully exploit the wealth of information provided by emission spectroscopy. A number of studies have already shown that the excited state properties of polypyridyl ruthenium complexes are sensitive to medium effects, such as solvent polarity [13-15] or pH [16,17].

This investigation examined the pH dependent emission data of a series of $[Ru(bpy)_3]^{2+}$ substituted amino acids (**1**-**4**, Figure 5.1). The synthetic amino acids feature bidentate binding sites for transition metal centers and can serve as building blocks for biomimetic assemblies [18]. The effect of protonation state of amino acid and amide linkage functional groups on the photophysical properties of $[Ru(bpy)_3]$ excited state are explored.

Figure 5.1 Structures of the Ru-substituted amino acids **1-4**, and **5**.

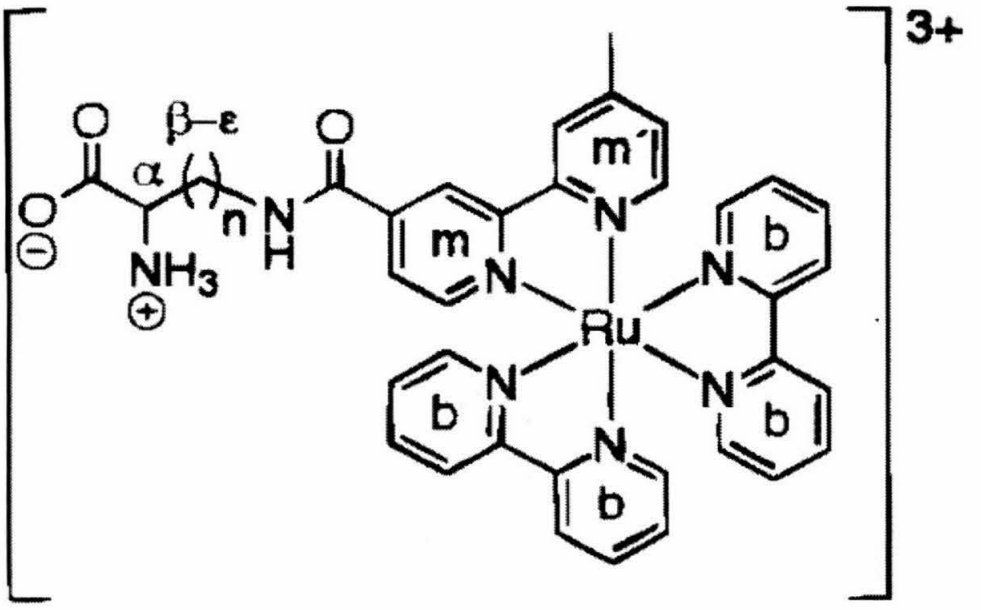

(1) n=1 [Ru(bpy)$_2$(bpy-CONH-DAPA)]
(2) n=2 [Ru(bpy)$_2$(bpy-CONH-DABA)]
(3) n=3 [Ru(bpy)$_2$(bpy-CONH-ORN)]
(4) n=4 [Ru(bpy)$_2$(bpy-CONH-LYS)]

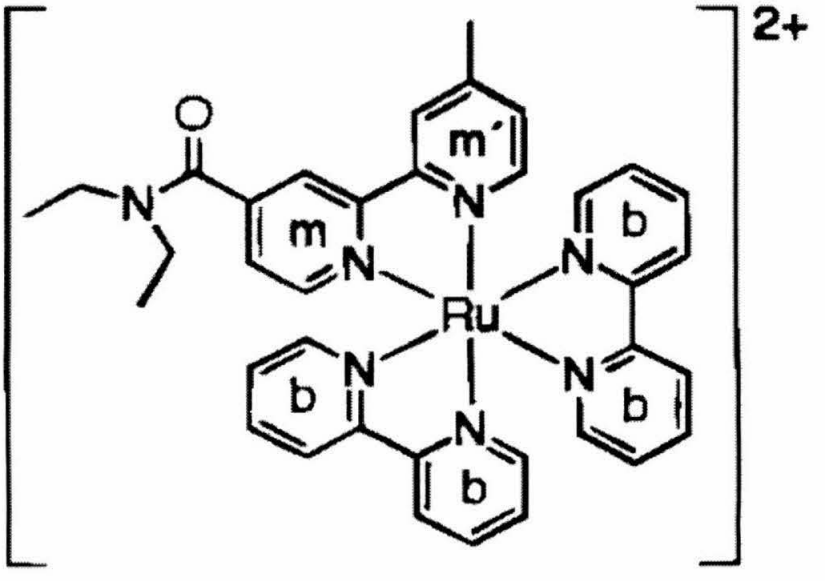

(5) [Ru(bpy)$_2$(bpy-CONEt$_2$)]

Experimental

Materials

$RuCl_3$ was a donation from Degussa. $[Ru(bpy)_2Cl_2]$ [20], $[Ru(bpy)_2(bpy')](PF_6)_2$ (bpy' = 4'-methyl-2,2'-bipyridine-4-carboxylic acid) [21], and $[Ru(bpy)_2(bpy'')](PF_6)_2$ (bpy'' = 4--carboxysuccinimidoester-4´-methyl-2,2´-bipyridine) [21] were prepared as described in the literature. $^{\alpha N\text{-}t}$Boc protected amino acids were purchased from Bachem and used as received. Reagent grade solvents were obtained from Roth, NMR solvents and all other chemicals from Aldrich. DMF and acetonitrile were purified by distillation over CaH_2 under N_2. Water for preparations and mechanistic studies was deionized.

Synthesis and Characterization

All compounds were synthesized and characterized by Bernd Geißer. The details of the synthesis can be found elsewhere [28].

C,H,N elemental analyses were performed on a Carlo Erba Elemental Analyser Model 1106.

The synthesis of $[Ru(bpy)_3]^{2+}$ modified amino acids followed the original preparation of $[(Ru(bpy)_2(bpy\text{-}Lys\text{-}^{\alpha N\text{-}t}Boc)]^{2+}$ ($^{\alpha N\text{-}t}$Boc-**4**) [21]. The succinimido ester $[Ru(bpy)_2(bpy'')](PF_6)_2$ was reacted with the respective $^{\alpha N\text{-}t}$Boc-protected L-amino acid to afford the ruthenium substituted $^{\alpha N\text{-}t}$Boc-derivatives of **1**-**4** (Figure 5.1) with over 90% yields. A number of photoredox active peptides [5,21] and peptide analogues, [22-24] as well as ruthenium-modified proteins [4,7,25] containing the lysine derivative **4** have

been reported earlier. However, little is known about the photophysical and chemical properties of the constituting ruthenium-modified amino acid itself.

Acid deprotection of $^{\alpha}$N-^{t}Boc-(**1-4**) is easily achieved in dioxane/HCl. Ion exchange chromatography followed by precipitation of the ruthenium complexes with ammonium hexafluorophosphate was used for purification of the free amino acids. It was difficult to remove excess salts, which accumulated during chromatography (NaCl) and precipitation (NH_4PF_6). Analytically pure compounds were obtained only by repeated stirring of suspensions of the amino acid complexes in water followed by acidification with HPF_6. As a consequence of this workup we always isolate the pure complexes in their +3 state with the amino acid carboxylate functions protonated. Losses during the purification process cause the yields to vary between 60 and 80% based on the protected ruthenated amino acids. Elemental analysis data indicate the presence of one equivalent of water which could not be removed by drying the compounds several days over silica gel under vacuum. The hexafluorophosphate salts are poorly soluble in water. However, concentrations below 0.1 mM can be obtained and the compounds readily dissolve in 0.01 M aqueous NaCl solutions permitting studies on aqueous solutions.

Proton NMR spectroscopy is the most valuable tool for structural characterization of the modified amino acids. Formation of the amide link during the synthesis of $^{\alpha}$N-^{t}Boc-**1-4** is accompanied by a characteristic low field shift of the amino acid ω-CH_2 signals (~ 0.5 ppm). For the diaminopropionic acid (DAPA) derivative $^{\alpha}$N-^{t}Boc-**1** a concomitant shift of the $^{\alpha}$CH signal from 4.04 to 4.39 ppm is also observed. Successful deprotection is evident from loss of the ^{t}Boc resonance at ~ 1.4 ppm.

Spectroscopy

UV-vis spectra were recorded on a Shimadzu UV-2101PC scanning spectrophotometer. Molar extinction coefficients were obtained from absorbance measurements as a function of complex concentration. IR spectra were recorded on a Mattson Polaris FT IR spectrophotometer using KBr pellets.

Proton NMR spectra were obtained on a Bruker Avance DPX 300 spectrometer. Solvent resonances were used as internal standards for measurements in methanol-d_4.

Luminescence spectra were recorded on a Perkin Elmer LS 50B spectrophotometer (λ_{exc} = 450 nm, λ_{obs} = 550-850 nm) equipped with a Hamamatsu R928 photomultiplier tube. 10 μM solutions of the complexes at different pH values were used and the data corrected for detector response.

Lifetimes

Luminescence lifetimes were obtained by exciting the samples with 480 nm light (20 ns FWHM, 2-3 mJ) obtained from a Lambda Physik FL 3002 dye laser (coumarin 480) pumped with a Lambda Physik LPX210i XeCl excimer laser. Shot selection was performed using a leading edge peak trigger directly linked to the digitizer. Single-wavelength kinetics were obtained by passing the emission from sample through a 160B Instruments SA double monochromator and detecting the light with a Hamamatsu R928 photomultiplier tube. The signal was fed to a 200 MHz amplifier then to a Tektronix RTD710A 200-MSs 10-bit transient digitizer interfaced to a PC.

Titration Curves

pH values were measured using a pH537 WTW microprocessor pH meter equipped with an Ingold 402-M6-S7 Ag/AgCl reference electrode. Solutions of the complexes in Britton Robinson buffers [19], at 0.1 M ionic strength, were used in a pH range from 1.8 to 12. Lower pH values were adjusted with calculated volumes of 2 M or 12 M HCl, and higher pH values with 2 M NaOH, respectively. The differences of ionic strength at extreme pH lead to negligible changes in luminescence intensities. This was tested by monitoring the luminescence intensity while varying the ionic strength from 0.1 and 5 M (adjusted with $NaClO_4$). The final complex concentration was 10 μM in all cases. Emission titration curves were followed by uncorrected luminescence spectra obtained on the instrument described above (λ_{exc} = 450 nm, λ_{obs} = 550-850 nm).

Results

NMR Titrations

The $^{\alpha}$CH resonances of **1-4** are pH dependent and shift to higher fields with increasing pH. This behavior is expected and typical for amino acids [26,27]. The ground state pK_A values of the amino acid functions of **1-4** were determined by plotting the chemical shifts of the $^{\alpha}$CH groups *vs.* pH (D_2O) and fitting the data to a three state acid base equilibrium [29]. The titration curve obtained for **1** is shown as an example in Figure 5.2. It has been shown by other authors that pK_A values obtained in D_2O usually agree well with pK_A values observed in H_2O and that a correction for deuterium effects is not necessary [30]. The results are summarized in Table 5.1 together with literature data [31].

Figure 5.2 pH Titration of **1** followed by NMR spectroscopy (chemical shift of the $^{\alpha}$-CH group *vs.* pH).

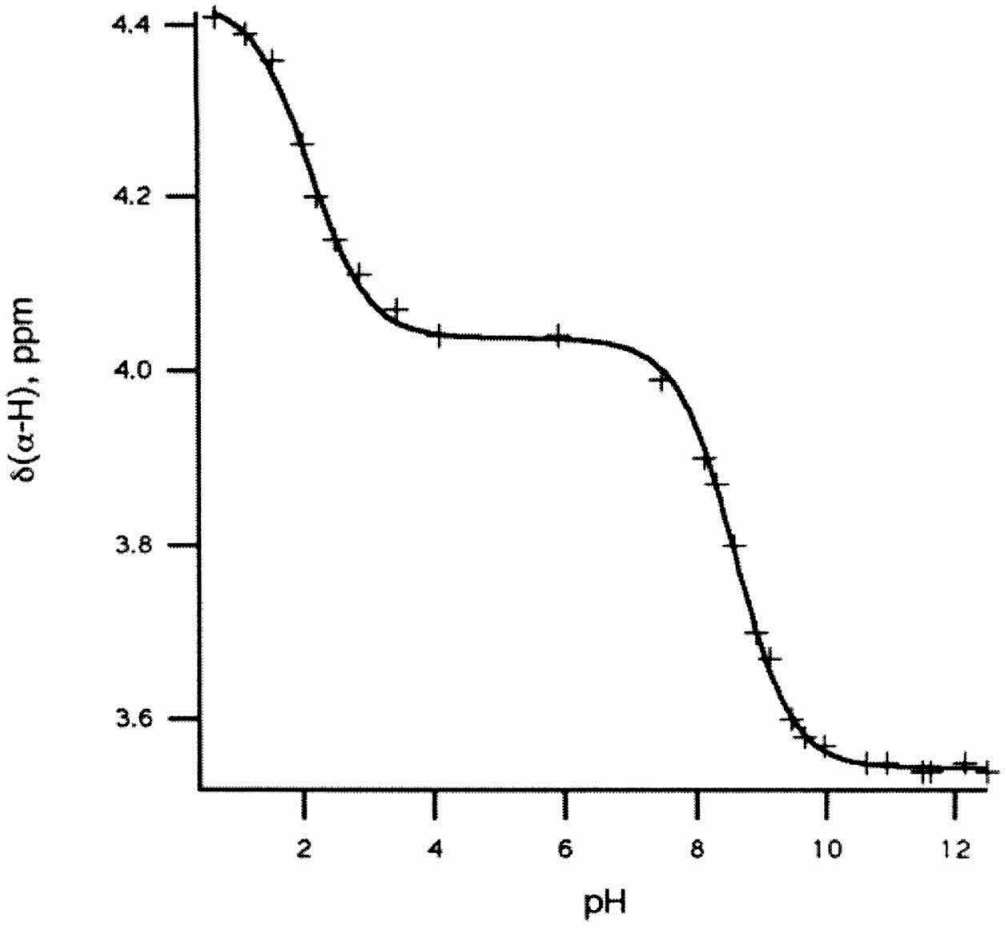
4.4
4.2
4.0
3.8
3.6
δ(α-H), ppm
2
4
6
8
10
12
pH

Absorption and Emission Spectra

The UV-visible spectra of **1-4** in aqueous solution are indistinguishable and typical for polypyridyl ruthenium complexes. The most significant feature is an MLCT band with a maximum at 457 nm (ε = 17700 $M^{-1}cm^{-1}$) and a shoulder at 427 nm. A strong intraligand π-π^* band appears at 287 nm (ε > 50000 $M^{-1}cm^{-1}$). No significant spectral changes were observed at pH values ranging from 0 to 14. In strongly acidic solutions (pH –1) the MLCT bands start to broaden and a shoulder at lower energies appears. This is shown in Figures 5.3a and 5.3b for the complexes **1** and the N,N-diethylamide **5**, respectively. Complex **5** was prepared as a control, which allowed comparison between contributions from the amide link and the amino acid functions in **1-4**. The MLCT band shift to lower energies is thus assigned to the ruthenium complex with protonated amide oxygen.

The emission spectra of **1-4** do not shift in wavelength from pH 0-14 significantly (Table 5.2, Figure 5.4). The intensity of the emission spectra, however, are very sensitive to pH (*vide infra*). Below pH –1, the emission spectra for **1-4** are undetectable. Compound **5**, however, exhibits a weak red-shifted emission band at pH –1 (Figure 5.5).

In Figure 5.6 the relative emission intensities of **1-4** are plotted as a function of pH. The complexes contain three protonation sites, the amide link, the carboxylate function, and the amine function. Two protonation steps corresponding to protonations of the amide (pH ~ 0.5) and the amine functions (pH ~ 9) are clearly distinguishable in each case. The inflection points around pH 9 for **1-4** and pH 3 (poorly resolved) for **1,2** are assigned to

Figure 5.3 Absorption spectra of a) MLCT bands of **1** and **5** (b) at pH 12 (—), 0 (- -), –0.78 (–·), and –1.1 (–··).

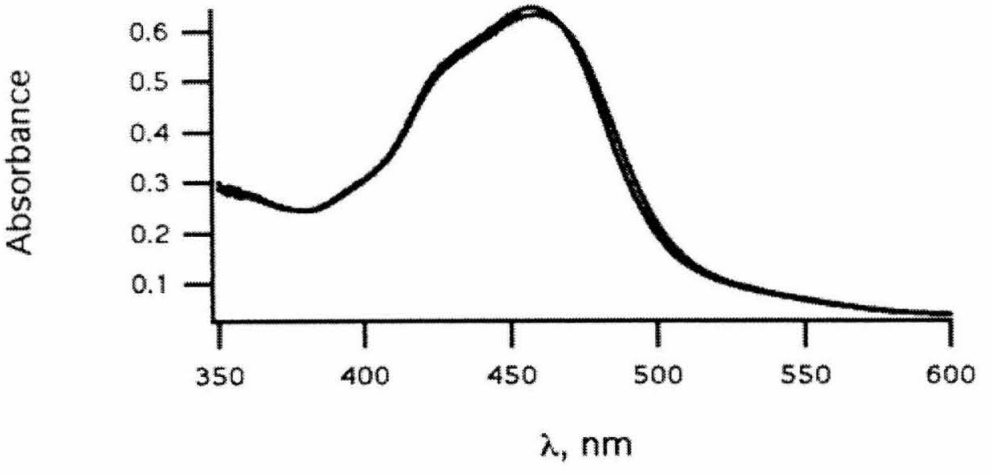
Absorbance
0.6
0.5
0.4
0.3
0.2
0.1
350
400
450
500
550
600
λ, nm

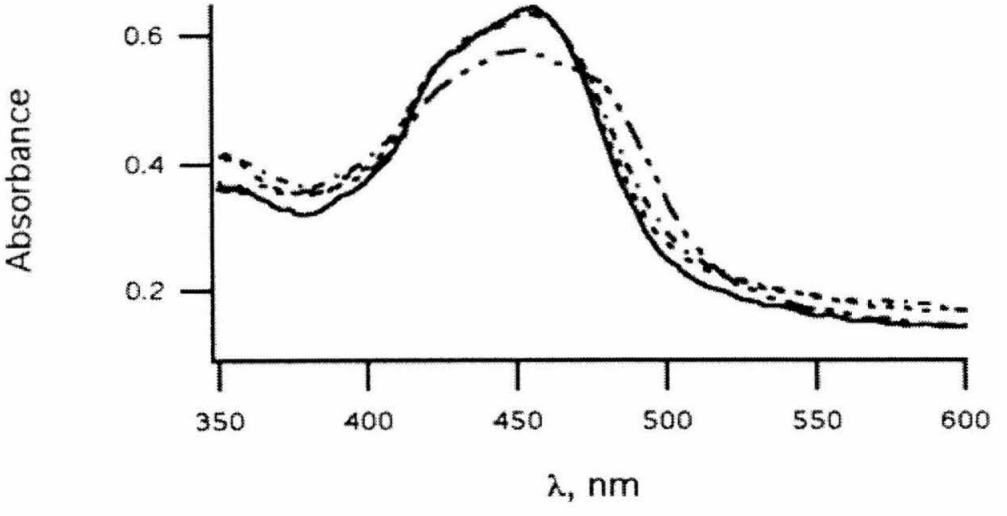
Absorbance
0.6
0.4
0.2
350
400
450
500
550
600
λ, nm

Figure 5.4 Luminescence spectra of **1-4** at pH 14 (highest intensities), pH 4.75 (-·-·; compounds indicated; intensities decrease with the number of methylene spacers), and pH 0 (lowest intensities).

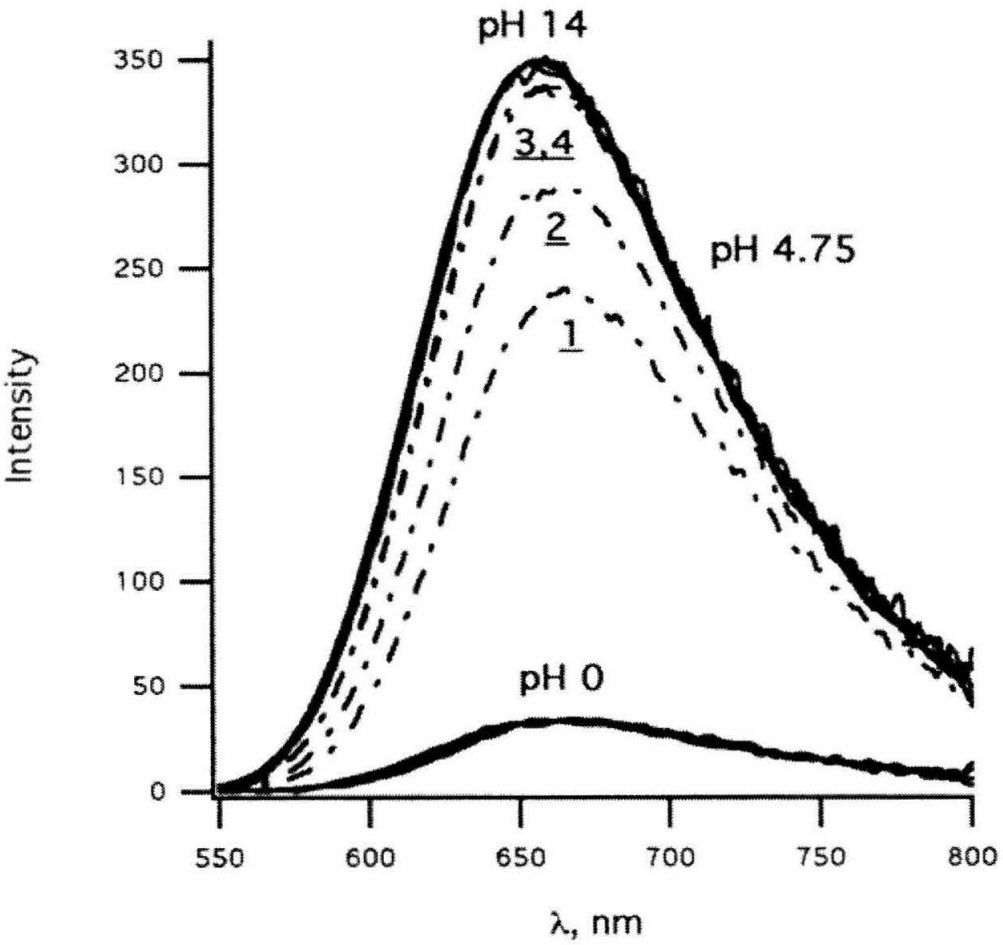
pH 14
3,4
2
1
pH 4.75
pH 0
Intensity
350
300
250
200
150
100
50
0
550
600
650
700
750
800
λ, nm

Figure 5.5 Luminescence spectra of 5 at pH 14, 2, 1, 0.5, 0, and –1.1 (decreasing intensities); Inset: Spectrum at pH –1.1.

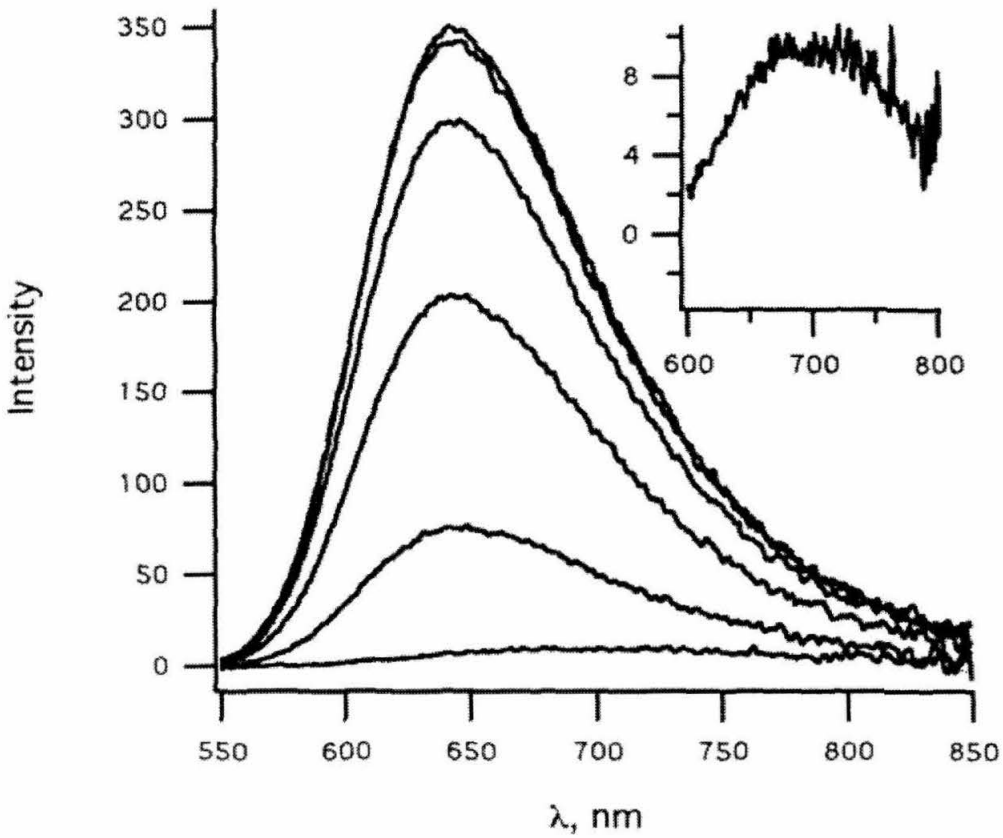
Intensity
350
300
250
200
150
100
50
0
550
600
650
700
750
800
850
λ, nm
8
4
0
600
700
800

Figure 5.6 pH dependence of emission intensities of **1** (Δ), **2** (#), **3** (◊), **4** (∇), and **5** (+) (intensities are relative to the values measured at pH 12; λ_{exc} = 450 nm).

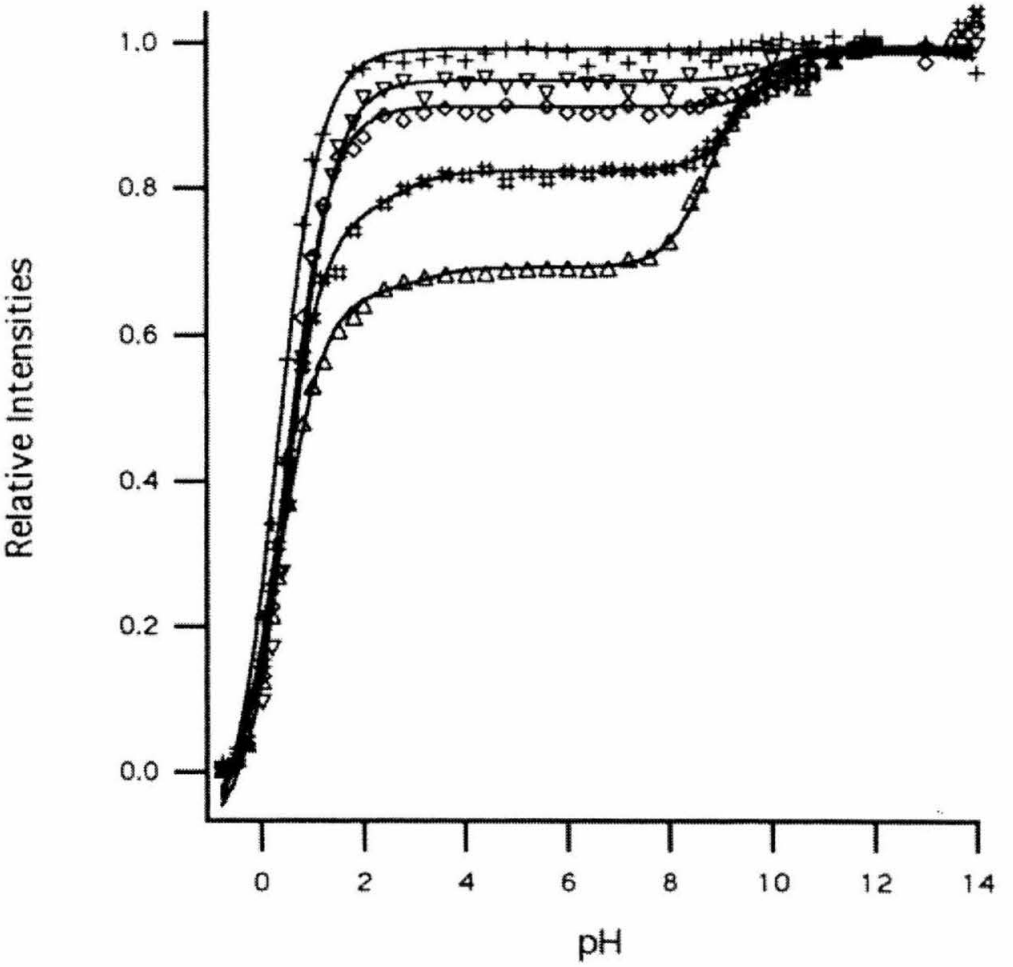
Relative Intensities
1.0
0.8
0.6
0.4
0.2
0.0
0
2
4
6
8
10
12
14
pH

Table 5.1 Ground state and apparent excited state pK_A values for **1-5** determined by NMR and luminescence spectroscopy, respectively, and some selected pK_A(amino acid-NH_3^+) data.

cmpd	pK_{Amide}*	pK_{COOH}	pK_{COOH}*	pK_{NH_3}	pK_{NH_3}*
1	0.37 ± 0.04	2.14 ± 0.03	3.19 ± 0.80	8.59 ± 0.02	8.82 ± 0.05
2	0.37 ± 0.04	2.14 ± 0.04	2.81 ± 0.52	9.33 ± 0.02	9.37 ± 0.09
3	0.49 ± 0.02	2.29 ± 0.04	-	9.64 ± 0.02	10.21 ± 0.19
4	0.60 ± 0.02	2.31 ± 0.05	-	9.80 ± 0.03	10.10 ± 0.51
DAPA[31]	-	1.3	-	6.68	-
DABA[31]	-	1.7	-	8.19	-
Orn[31]	-	1.9	-	8.78	-
Lys[31]	-	2.19	-	9.12	-
Asn[31]	-	2.15	-	8.72	-
Gln[31]	-	2.16	-	9.01	-
5	0.31 ± 0.02	-	-	-	-

Figure 5.7 Luminescence decay kinetics of **1** at pH 12, 4.8, 2.0, and 0.55. The lifetimes become shorter with decreasing pH.

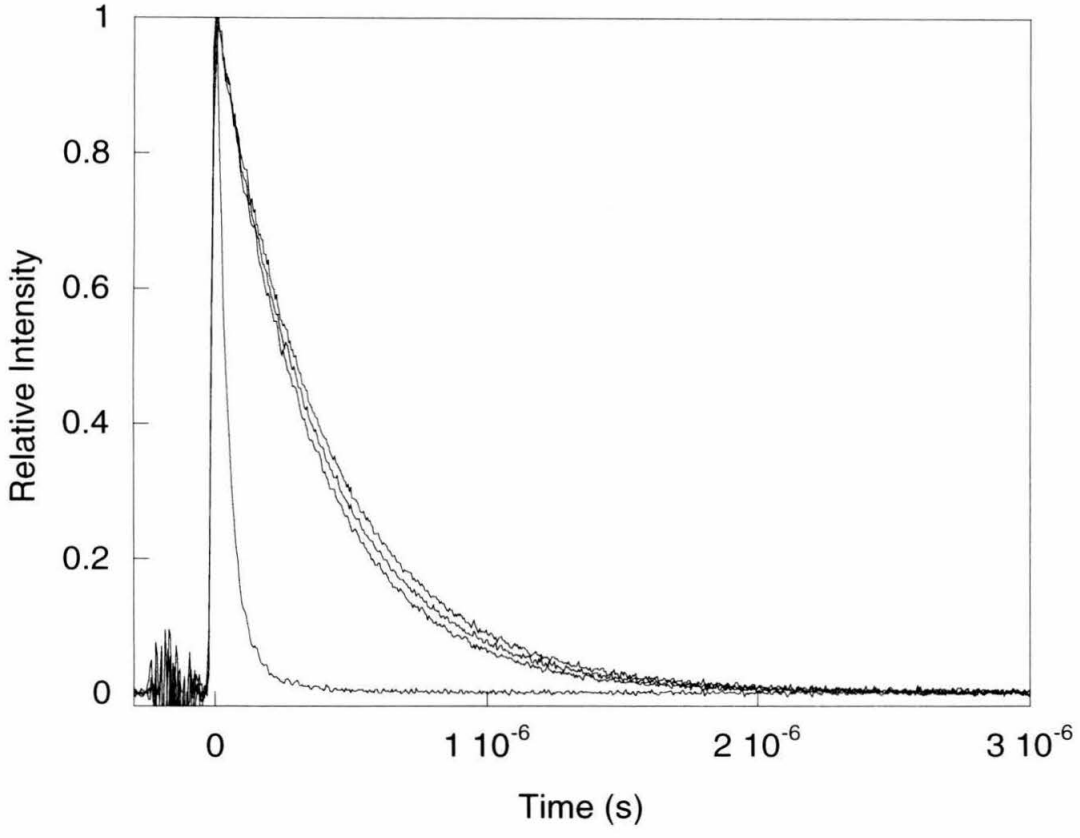
1
0.8
0.6
0.4
0.2
0
Relative Intensity
0
1 10-6
2 10-6
3 10-6
Time (s)

Figure 5.8 Luminescence decay kinetics of **1-4** at pH 12.

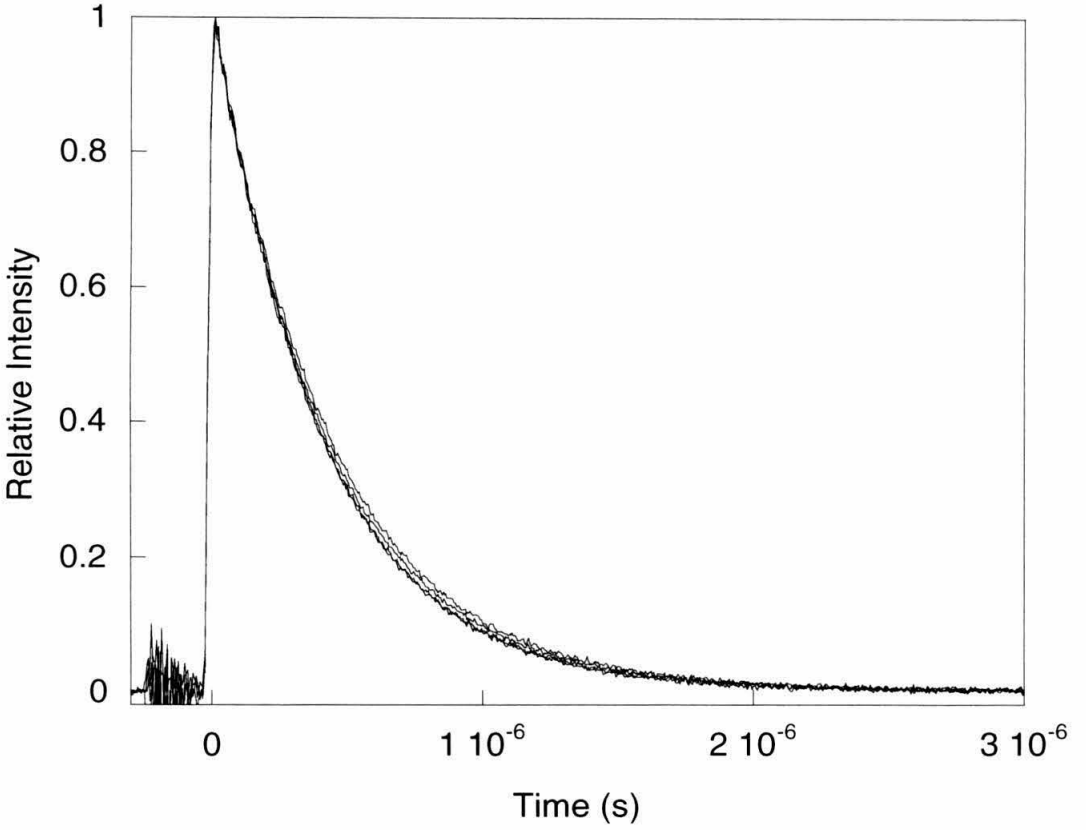
1
0.8
0.6
0.4
0.2
0
Relative Intensity
0
1 10-6
2 10-6
3 10-6
Time (s)

Figure 5.9 Luminescence decay kinetics of **1-4** at pH 4.8.

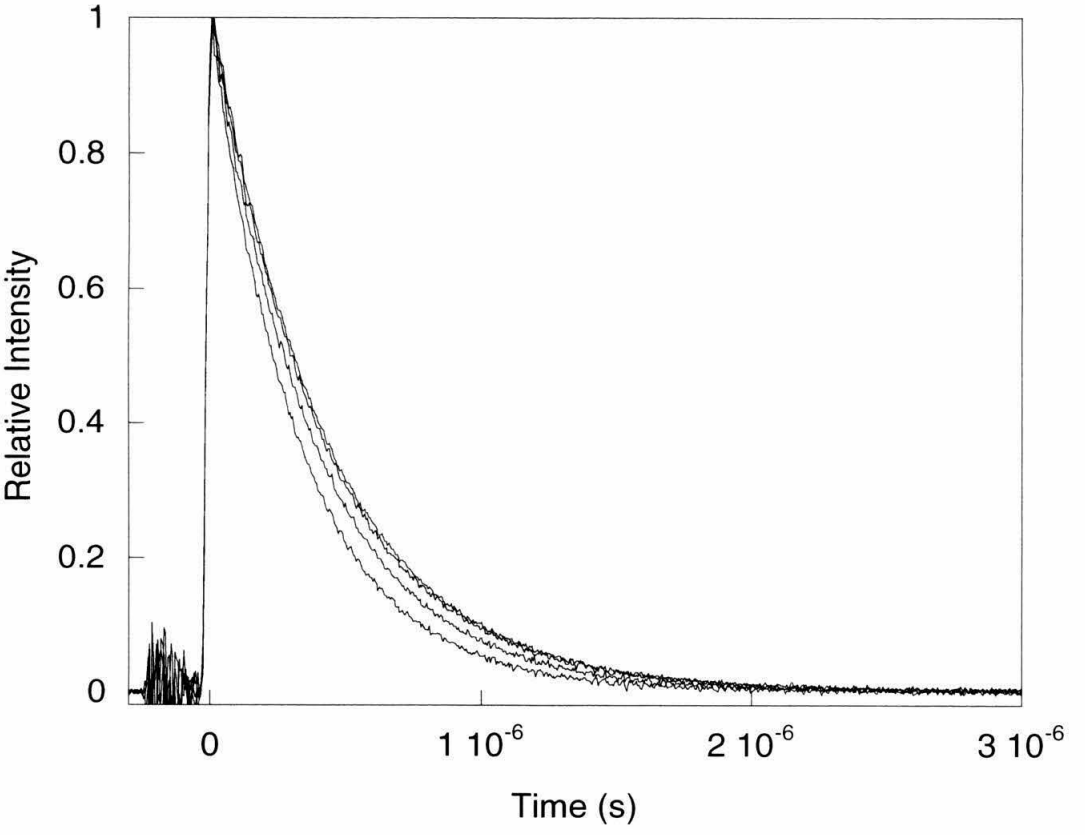
1
0.8
0.6
0.4
0.2
0
Relative Intensity
0
1 10-6
2 10-6
3 10-6
Time (s)

Figure 5.10 Luminescence decay kinetics of **1-4** at pH 2.0.

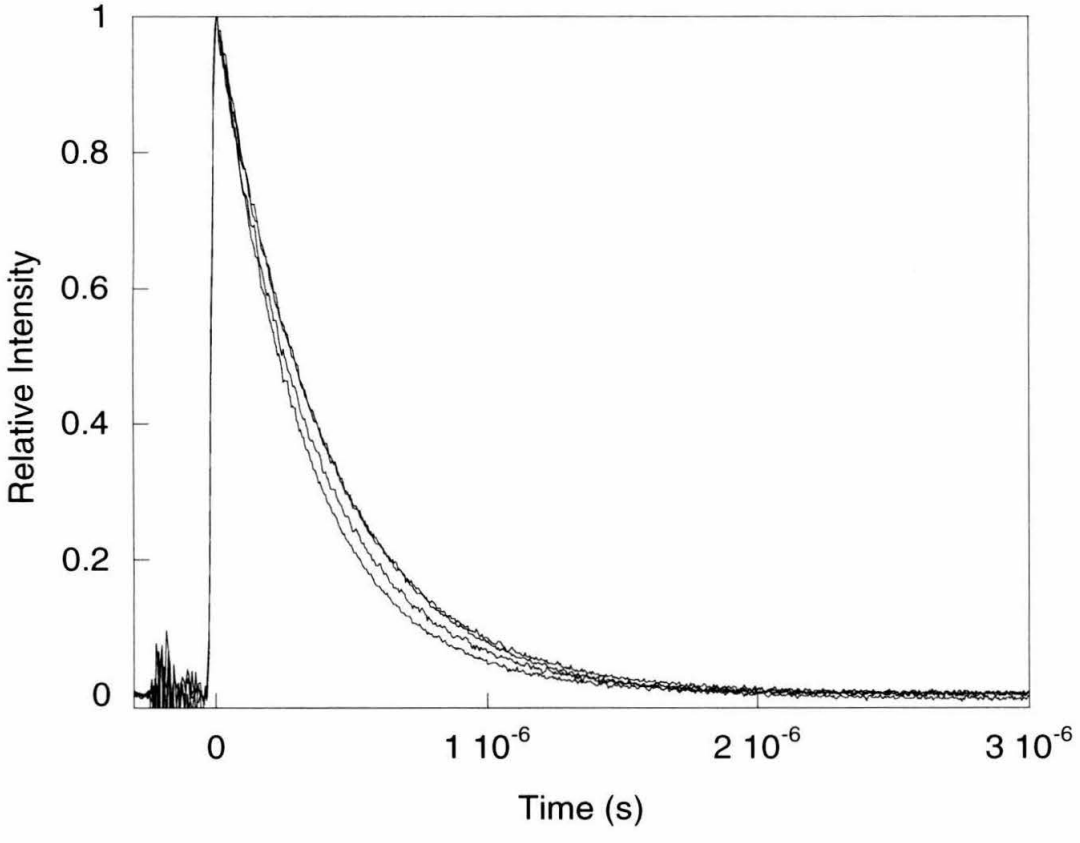
1
0.8
0.6
0.4
0.2
0
Relative Intensity
0
1 10-6
2 10-6
3 10-6
Time (s)

Figure 5.11 Luminescence decay kinetics of **1-4** at pH 0.55.

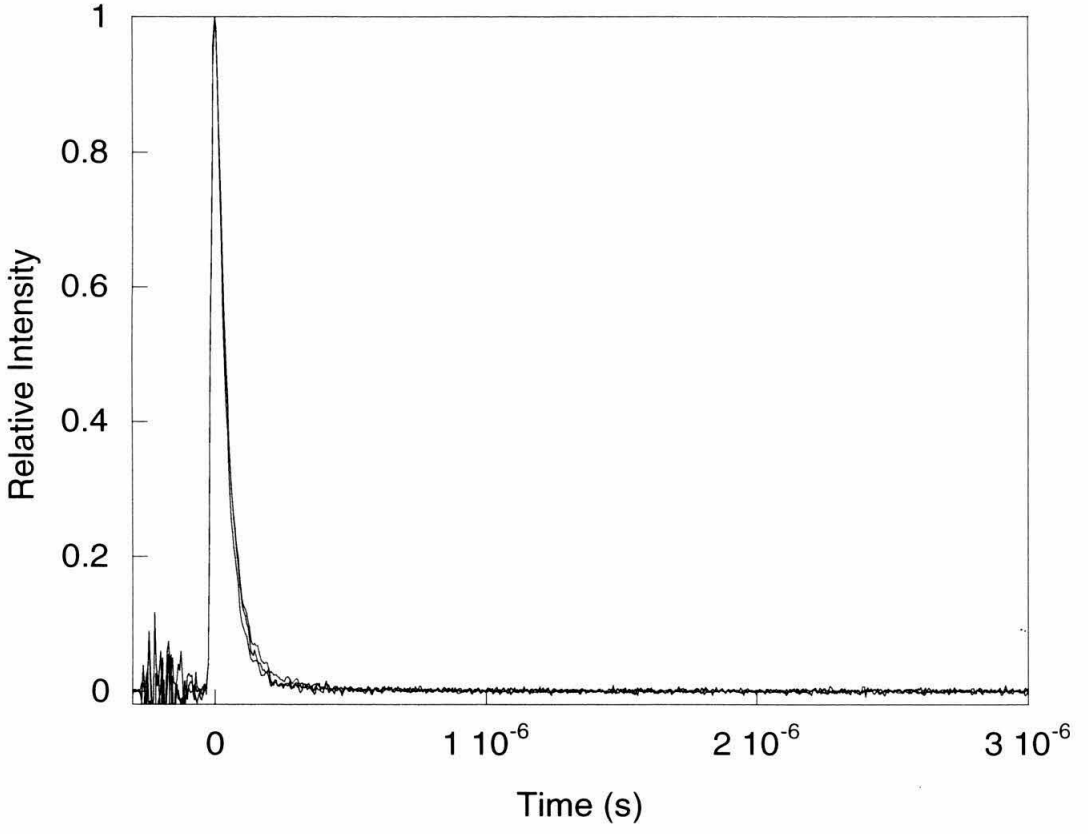
1
0.8
0.6
0.4
0.2
0
Relative Intensity
0
1 10-6
2 10-6
3 10-6
Time (s)

Figure 5.12 Luminescence decay kinetics of **1-4** at pH 12 in H_2O and D_2O.

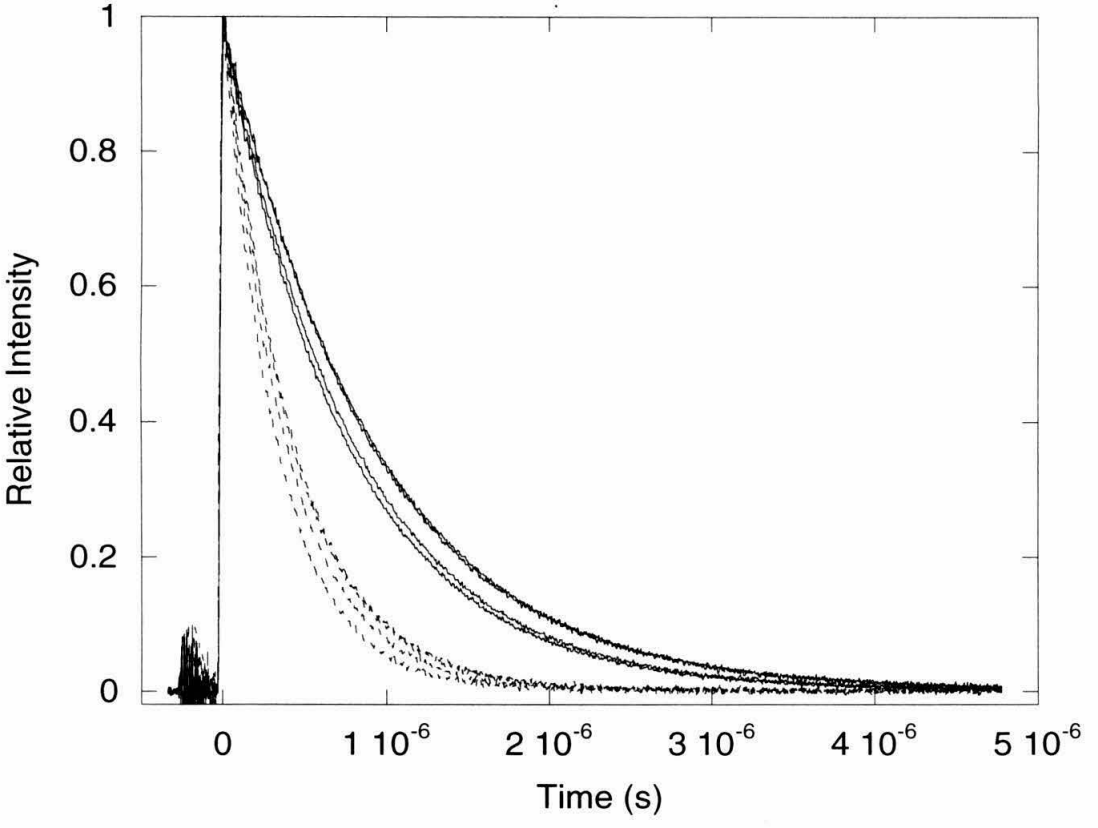
1
0.8
0.6
0.4
0.2
0
Relative Intensity
0
1 10-6
2 10-6
3 10-6
4 10-6
5 10-6
Time (s)

Table 5.2 Excited state lifetimes and emission energies of **1-4** at different pH values.

	pH 0.55		pH 4.77		pH 12	
cmpd	τ, ns	E_{em}, cm^{-1}	τ, ns	E_{em}, cm^{-1}	τ, ns	E_{em}, cm^{-1}
1	64	14880	337	14970	429	15174
2	77	14880	386	15060	412	15174
3	61	14880	420	15128	444	15174
4	59	14880	427	15151	412	15174

pK_{NH_3}* and pK_{COOH}*, respectively. These pK* (Table 5.1) values are typical for α-amino acids functions [31] and are close to ground state pK values obtained by NMR spectroscopy. The apparent excited state pK_A* values (Table 5.1) were determined by fitting the data to a three state acid base equilibrium for **3** and **4**, and to a four state equilibrium for **1** and **2** [29]. Also shown in Figure 5.6 is the luminescence titration curve of **5** and the corresponding fit to a two state equilibrium. **5** contains only the amide functional group and consequently exhibits only a single inflection at low pH.

At very high and very low pH values the emission intensities of **1-4** do not vary with amino-acid side chain length and are similar to those of **5**. In the intermediate pH 2-8 range, however, an interesting dependence on amino-acid side chain length is found. The emission intensities increase significantly with the number (n) of methylene groups (Figure 5.1). These findings are confirmed by lifetime measurements at pH 0.5, 2, 4, and 12 (Table 5.2).

Discussion

The pH dependent emission properties of **5** resemble those of $[Ru(bpy)_3]^{2+}$ derivatives bearing carboxylate groups directly attached to one or more of the bipyridine ligands [37]. The ground-state pK_A's of the carboxylate groups on $[Ru(bpy)_2(4,4'\text{-dcbpy})]^{2+}$ are 2.15 and 1.75, respectively, resulting in pH-dependent UV-vis spectra [38-43]. The emission spectra are also pH-dependent, with an apparent excited-state pK_A* of 4.25. The difference between ground and excited state pK_A's indicates increased basicity of the excited state with respect to the ground state. In general, protonation of a

functional group in conjugation with the bipyridine ligand leads to luminescence quenching (Figure 5.13).

The pH dependent emission behavior of **5** is interpreted as the result of an amide oxygen protonation in the excited state. Emission quenching in **5** *via* amide protonation is considerably more efficient than in corresponding carboxylate species. This quenching occurs at lower pH and is consistent with lower pK_A and pK_A^* values of the amide function ($pK_1^* \sim 0.5$, Table 5.2).

The UV-vis spectrum of the complex is pH independent in the pH 0-14 range. A shift of the MLCT bands to lower energies is observed in strongly acidic solutions (pH < –1, Figure 5.3) indicating that the ground state $pK_A < 0$ for the amide oxygen. Although the difference between ground- and excited-state pK_A is not quantified, the excited state is expected to be more basic than the ground state since three mesomeric structures exist in the excited state in which the amide oxygen carries a partial negative charge [44].

The amino acid complexes **1-4** also show efficient luminescence quenching below pH 1, which is mainly due to protonation of the amide links. A small superimposed effect of the carboxylate functions of **1** and **2** is evident from the titration curves shown in Figure 5.4. The absorption spectra of **1-4** do not change with either pH or side-chain length indicating the absence of direct electronic interactions between the amino acid functions and the ruthenium chromophore. This behavior is expected since the methylene spacers prevent efficient electronic coupling between the two functional groups.

Similarly, small shifts of the emission bands to lower energies is observed as the pH is lowered to 0. However, the nonradiative decay rates increase significantly. This observation is consistent with the presence of an excited-state protonation quenching

mechanism (Figure 5.13) [16].

The luminescence of $^{*}M$ is quenched by protons according to the Stern-Volmer relationship given in Equations 5.1 and 5.2.

Equation 5.1.
$$\frac{I_0}{I} = \frac{\tau_0}{\tau} = 1 + \frac{k_H \tau_0}{1 + k_{-H}\tau_0'}\left[H^+\right] = 1 + k_q \tau_0 \left[H^+\right]$$

Equation 5.2.
$$k_q = \frac{k_H}{1 + k_{-H}\tau_0'}$$

If the protonated complex $*MH^+$ in Figure 5.13 is very short lived ($\tau_0 >> \tau'_0$), then observed emission is predominantly from *M. In such a case, one would not expect the emission band to shift significantly upon lowering the pH. It is evident from Figure 5.6 that the titration curve has not reached its minimum at pH 0. Thus, *M (unprotonated amide link) will contribute significantly to the observed luminescence, which explains the negligible red shift of the emission curve maxima. Below pH 0, the emission of **1-4** is undetectable. For complex **5** a residual emission is observed even at pH –1.7 (Figure 5.5) and the band appears significantly shifted to lower energies. A plot of the emission lifetimes of **5** *vs.* $[H^+]$ show the expected linear Stern-Volmer behavior in a pH –0.5-3 range (Figure 5.14). In this range no significant band shift is observed. In 12 M HCl solution, however, the steady-state approximation in Equation 5.3 does not remain valid because the red-shifted emission from the protonated complex significantly contributes to the total intensity.

It is evident from our data that the remote amino acid moiety has a small, yet distinct, effect on the excited-state properties of the ruthenium chromophore in the pH 2-

Figure 5.13 Ground- and excited-state acid-base equilibrium.

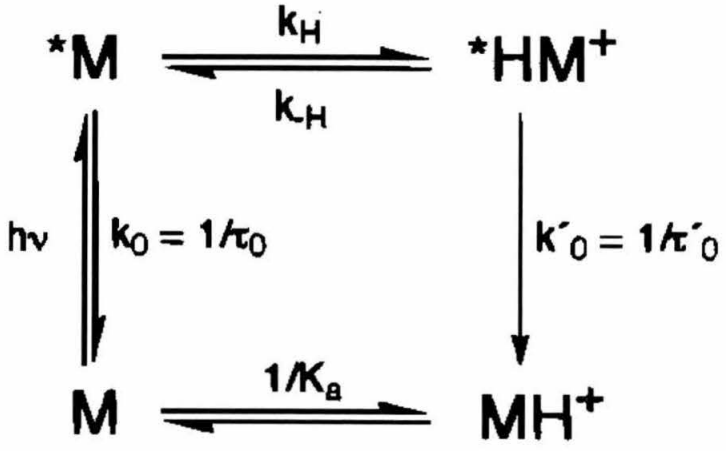
*M
k_H
k_{-H}
*HM+
hν
$k_0 = 1/\tau_0$
$k'_0 = 1/\tau'_0$
M
$1/K_a$
MH+

Figure 5.14 Stern-Volmer plot of $1/\tau$ *vs.* $[H^+]$.

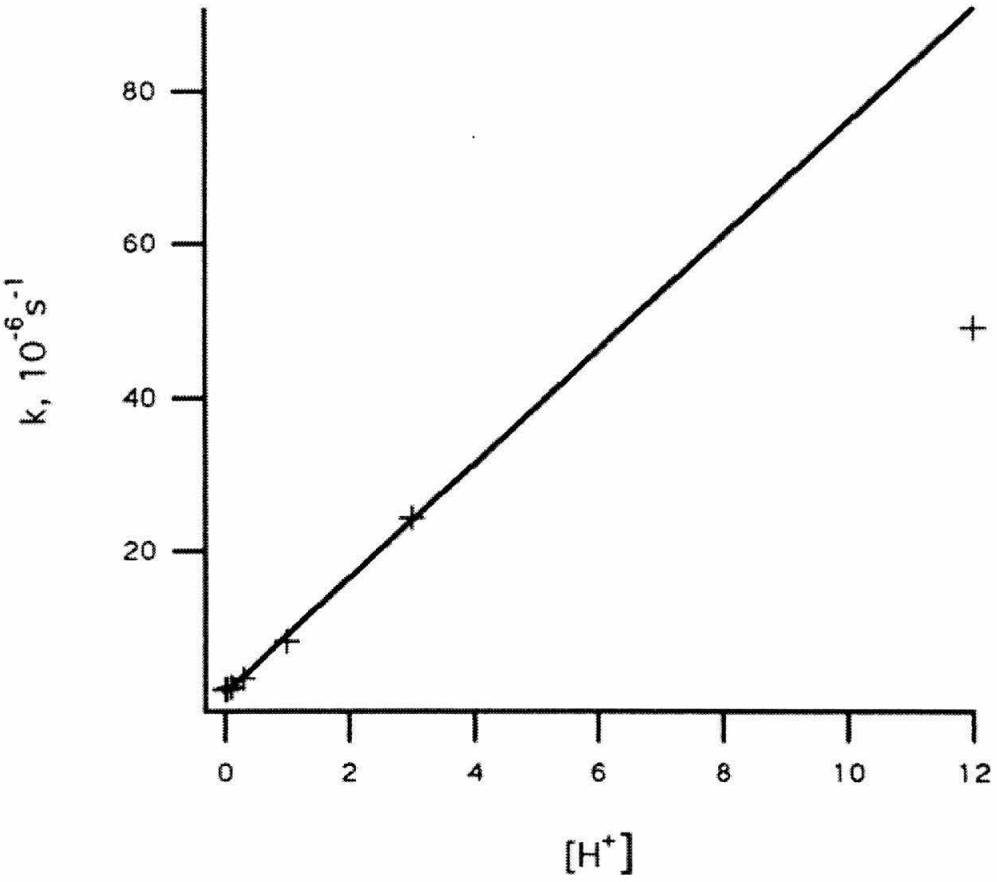
80
60
40
20
k, 10^{-6} s^{-1}
0
2
4
6
8
10
12
[H^+]

10 range. The intensity of the luminescence depends exponentially on the amino-acid to chromophore separation (Figure 5.6). This is mirrored by an exponential dependence of the pKa's reported for the amino-acid functional group of **1-4**. The observed distance dependence of pKa's is most likely due to an inductive effect of the amide linkage since the amide substituded amino acids, Asn and Gln, exhibit comparable pKa's to the corresponding Dapa (n=1) and Daba (n=2) Ru-modified amino acids. The electronic interaction that perturb the pKa's of the amine also makes the electron density around the amide bond sensitive to the protonation state of the amine. This is evidenced by similar distance decay constants (~0.9 $Å^{-1}$) for the pKa and luminescence intensity distance dependence (amide-amine distance). The change of the electron density of the amide oxygen leads to larger Franck-Condon factors that lead to increased nonradiative decay and subsequent luminescence quenching. This behavior is similar to the quenching behavior at low pH where the amide becomes protonated.

Conclusions

The results presented in this report show that large perturbations of excited state dynamics of $[Ru(bpy)_3]^{2+}$ result when subtle changes of remote functional groups are effected. The systems we studied are particularly relevant for sensing applications in biological systems using luminescent metal complexes, since the amide link used for the synthesis of **1-4** provides a convenient route to metallated peptides and proteins. Our data suggest that the photophysical properties of the ruthenium chromophore are very sensitive to the protonation state of the amide linkage. Moreover, the modulation of excited state properties by weak electronic interactions between the chromophore and remote

functional groups provides interesting means of controlling the properties of supramolecular photochemical molecular devices (PMDs) [53]. It supplements the tuning of photoredox properties by ligand modification [54-56].

References

[1] HB Gray, JR Winkler, *Annu. Rev. Biochem.*, **65**, 537-561 (1996).

[2] JK Barton, In *Bioinorganic Chemistry*; I Bertini, HB Gray, SJ Lippard, JS Valentine, Eds., University Science Books: Mill Valley, 455-503 (1994).

[3] TJ Meade, In *Interactions of Metal Ions with Nucleotides, Nucleic Acids, and their Constituents*; A Sigel, H Sigel, Eds., Marcel Dekker: New York, **32**, 453-478 (1996).

[4] K Shreder, A Harriman, BL Iverson, *J. Am. Chem. Soc.*, **118**, 3192-3201 (1996).

[5] H Szmacinski, E Terpetschnig, JR Lakowicz, *Biophys. Chem.*, **62**, 109-120 (1996).

[6] DG McCafferty, BM Bishop, CG Wall, SG Hughes, SL Mecklenburg, TJ Meyer, BW Erickson, *Tetrahedron*, **51**, 1093-1106 (1995).

[7] B Durham, LP Pan, JE Long, F Millett, *Biochemistry*, **28**, 8659-8665 (1989).

[8] R-Q Liu, MA Miller, GW Han, S Hahm, L Geren, S Hibdon, J Kraut, B Durham, F Millett, *Biochemistry*, **33**, 8678-8685 (1994).

[9] DS Wuttke, HB Gray, SL Fisher, B Imperiali, *J. Am. Chem. Soc.*, **115**, 8455-8456 (1993).

[10] S Jurisson, D Berning, W Jia, D Ma, *Chem. Rev.*, **93**, 1137-1156 (1993).

[11] D Parker, *Chem. Soc. Rev.*, **19**, 271-291 (1990).

[12] X Cha, K Ariga, T Kunitake, *J. Am. Chem. Soc.*, **118**, 9545-9551 (1996).

[13] JV Caspar, TJ Meyer, *J. Am. Chem. Soc.*, **105**, 5583-5590 (1983).

[14] H Sun, MZ Hoffman, *J. Phys. Chem.*, **97**, 11956-11959 (1993).

[15] RB Nair, BM Cullum, CJ Murphy, *Inorg. Chem*, **36**, 962-965 (1997).

[16] H Sun, MZ Hoffman, *J. Phys. Chem.*, **97**, 5014-5018 (1993).

[17] AMW Cargill Thompson, MCC Smailes, JC Jeffery, MD Ward, *J. Chem. Soc., Dalton Trans.*, 737-743 (1997).

[18] R Alsfasser, R van Eldik, *Inorg. Chem.*, **35**, 628-636 (1996).

[19] FW Küster, A Thiel, A Ruland, *Rechentafeln für die chemische Analytik;* 103 ed.; W. de Gruyter: Berlin, New York, pp 161 (1985).

[20] BP Sullivan, DJ Salmon, TJ Meyer, *Inorg. Chem.*, **17**, 3334-3341 (1978).

[21] BM Peek, GT Ross, SW Edwards, GJ Meyer, TJ Meyer, BW Erickson, *Int. J. Pept. Protein Res.*, **38**, 114-123 (1991).

[22] SL Mecklenburg, DG McCafferty, JR Schoonover, BM Peek, BW Erickson, TJ Meyer, *Inorg. Chem.*, **33**, 2974-2983 (1994).

[23] SL Mecklenburg, BM Peek, JR Schoonover, DG McCafferty, CG Wall, BW Erickson, TJ Meyer, *J. Am. Chem. Soc.*, **115**, 5479-5495 (1993).

[24] SL Mecklenburg, BM Peek, BW Erickson, TJ Meyer*J. Am. Chem. Soc.*, **113**, 8540-8542 (1991).

[25] LP Pan, B Durham, J Wolinska, F Millett, *Biochemistry*, **27**, 7180-7184 (1988).

[26] CA Evans, DL Rabenstein, *J. Am. Chem. Soc.*, **96**, 7312-7317 (1974).

[27] TL Sayer, DL Rabenstein, *Can. J. Chem.*, **54**, 3392-3400 (1976).

[28] B Geiser, A Ponce, R Alsfasser, *Inorg. Chem.*, **38**, 2030-2037 (1999).

[29] $$I_{obs} = \frac{I_M + I_{MH} \cdot 10^{(pK_2 - pH)} + I_{MH_2} \cdot 10^{(pK_1 + pK_2 - 2pH)}}{1 + 10^{(pK_2 - pH)} + 10^{(pK_1 + pK_2 - 2pH)}}$$

For a complete treatment refer to: AM Josceanu, P Moore, SC Rawle, P Sheldon, SM Smith, *Inorg. Chim. Acta*, **240**, 159-168 (1995).

[30] KH Scheller, V Scheller-Krattiger, RB Martin, *J. Am. Chem. Soc.*, **103**, 6833-6839 (1981).

[31] T Kiss, In *Biocoordination Chemistry*; K Burger, Ed., Ellis Horwood: New York, pp 56-134 (1990).

[32] J Desilvestro, M Grätzel, L Kavan, J Moser, *J. Am. Chem. Soc.*, **107**, 2988-2990 (1985).

[33] DN Furlong, D Wells, WHF Sasse, *J. Phys. Chem.*, **90**, 1107-1115 (1986).

[34] R Dabestani, AJ Bard, A Campion, MA Fox, TE Mallouk, SE Webber, JM White, *J. Phys. Chem.*, **92**, 1872-1878 (1988).

[35] N Vlachopoulos, P Liska, J Augustynski, M Grätzel, *J. Am. Chem. Soc.*, **110**, 1216-1220 (1988).

[36] TK Foreman, WM Sobol, DG Whitten, *J. Am. Chem. Soc.*, **103**, 5333-5336 (1981).

[37] JG Vos, *Polyhedron*, **11**, 2285-2299 (1992).

[38] PJ Giordano, CR Bock, MS Wrighton, LV Interrante, RFX Williams, *J. Am. Chem. Soc.*, **99**, 3187-3195 (1977).

[39] PA Lay, WHF Sasse,*Inorg. Chem.*, **23**, 4123-4125 (1984).

[40] MK Nazeeruddin, K Kalyanasundaram, *Inorg. Chem.*, **28**, 4251-4259 (1989).

[41] T Shimidzu, T Iyoda, K Izaki, *J. Phys. Chem.*, **89**, 642-645 (1985).

[42] K Kalyanasundaram, MK Nazeeruddin, M Grätzel, *Inorg. Chim. Acta*, **199**, 831-839 (1992).

[43] JW Park, J Ahn, C Lee, *J. Photochem. Photobiol. A*, **86**, 89-95 (1995).

[44] WE Ford, M Calvin, *Chem. Phys. Lett.*, **76**, 105-108 (1980).

[48] PD Beer, SW Dent, TJ Wear,*J. Chem. Soc., Dalton Trans.*, 2341-2346 (1996).

[49] PD Beer, SW Dent, NC Fletcher, TJ Wear,*Polyhedron*, **15**, 2983-2996 (1996).

[50] PD Beer, *Chem. Commun.*, 689-696 (1996).

[53] V Balzani, F Scandola, In *Supramolecular Technology*; DN Reinhoudt, Ed.; Elsevier: Oxford, Vol. 10; pp 687-746 (1996).

[54] M Furue, K Maruyama, T Oguni, M Naiki, M Kamachi, *Inorg. Chem*, **31**, 3792-3795 (1992).

[55] M Maestri, N Armaroli, V Balzani, EC Constable, AMW Cargill Thompson, *Inorg. Chem*, **34**, 2759-2767 (1995).

[56] PA Anderson, GB Deacon, KH Haarmann, FR Keene, TJ Meyer, D Reitsma, BW Skelton, GF Strouse, NC Thomas, JA Treadway, AH White, *Inorg. Chem.*, **34**, 6145-6157 (1995).